UNIVERSITY OF LJUBLJANA
FACULTY OF MATHEMATICS AND PHYSICS
DEPARTMENT OF PHYSICS

Klemen Kunstelj

STRUCTURAL ANALYSIS OF SURFACE LAYERS WITH NON-LINEAR OPTICAL TECHNIQUES

Doctoral thesis

ADVISER: Prof. dr. Irena Drevenšek-Olenik

Ljubljana, 2009

UNIVERZA V LJUBLJANI
FAKULTETA ZA MATEMATIKO IN FIZIKO
ODDELEK ZA FIZIKO

Klemen Kunstelj

STRUKTURNA ANALIZA POVRŠINSKIH PLASTI Z METODAMI NELINEARNE OPTIKE

Doktorska disertacija

MENTOR: Prof. dr. Irena Drevenšek-Olenik

Ljubljana, 2009

Abstract

In this thesis we present the assembly and testing of two non-linear optical techniques, i.e. second-harmonic generation (SHG) and sum-frequency generation (SFG). The main characteristic of all nonlinear optical effects of second order is their nature of being allowed only and specifically at the surface or interface between two centrosymmetric media. Therefore both SFG and SHG can be used to study thin alignment layers in liquid crystal displays (LCD) and for investigating thin layers of specific biomolecular architectures.

The SHG experimental technique was assembled as part of the ultrafast Ti:sapphire laser system. We studied the dynamics and phase characteristics of thin alignment layer for liquid crystals by studying the dependence of the SHG response on an applied external electric field. In spite of the fact that the FLCP alignment layers are relatively thin (200 nm), the SHG results indicate a pinned domain-like structure. Understanding of the switching process as a whole is crucial for further applications of these alignment layers in the LCD industry.

In the second part of the thesis we present the development of the SFG technique and continue with a short description of Atomic Force Microscopy (AFM). By using combined AFM and SFG methods we study thin layers of Guanosine 5´-monophosphate (GMP) and heptadecanoic acid (HDA) in various environments. The GMP molecule is the RNA nucleotide which due to its specific nature organizes into highly ordered supramolecular structures, i.e. quartets and wires. The results of both AFM and SFG show that GMP molecules on the surface of mica substrate can organize into ordered wire- or layer-like surface structures at lower concentrations and they form different bulk conformations at higher concentrations. Heptadecanoic acid belongs to a larger group known as fatty acids which possess an amphiphilic behavior, i.e. they are capable of forming monolayers on the water surface. The results of AFM and SFG analysis show that the transfer of HDA molecules from the water surface to solid substrate leads to formation of inhomogeneities in the Langmuir-Blodgett film. Despite this inconvenience we are able to determine the orientation of HDA molecules and within the model predict the formation of different phases of HDA monolayers.

PACS: 42.65.Ky, 61.30.Vx, 61.30.Hn, 64.70.M, 68.18.-g, 68.37.Ps, 68.47.Pe, 81.16.Dn

Keywords: Alignment layers for liquid crystals, Second-harmonic generation (SHG), Sum-frequency generation (SFG), Atomic Force Microscopy (AFM), Guanosine, Langmuir-Blodgett films.

Povzetek

V disertaciji bomo predstavili nelinearni optični metodi podvajanja frekvenc (SHG) in generacije vsote frekvenc (SFG). Obe spadata v večjo skupino nelinearnih optičnih pojavov drugega reda, katerih glavna značilnost je občutljivost na površine oz. mejne plasti med dvema centrosimetričnima materialoma. Zaradi te specifične lastnosti ju lahko uporabimo pri proučevanju tankih urejevalnih slojev za tekoče kristale, kot tudi tankih slojev različnih organskih molekul.

Eksperimentalno metodo SHG smo postavili kot del večjega ultrahitrega titan-safirnega laserskega sistema. S SHG meritvami smo proučevali dinamične in fazne lastnosti novih urejevalnih slojev tekočih kristalov, t.i sloje iz feroelektričnega tekočekristalnega polimera. Rezultati so pokazali, da je kljub relativno tankemu urejevalnemu sloju, to je okoli 200 nm, njegova struktura še vedno precej kompleksna in kaže tipično domensko strukturo. Natančno poznavanje strukture tega sloja je namreč ključno pri nadaljnjem uvajanju le-teh v industriji tekočekristalnih zaslonov.

V drugem delu disertacije je podrobno opisana eksperimentalna postavitev SFG in na kratko predstavljena metoda mikroskopa na atomsko silo (AFM). S pomočjo obeh smo namreč proučevali tanke površinske strukture molekul gvanozin 5´-monofosfata (GMP) in heptadekanojske kisline (HDA). GMP molekula je RNK nukleotid, ki ima zaradi svojih specifičnih lastnosti zmožnost samourejanja v večje molekulske skupke (kvartete, žičke). Z uporabo kombinacije obeh eksperimentalnih metod smo namreč lahko spremljali različne konformacijske spremembe v nastali površinski strukturi molekul GMP, ki nastanejo zaradi spremembe v koncentraciji med nanosom na površino. HDA molekula spada med maščobne kisline, ki imajo podobno kot lipidi amfifilne lastnosti oz. so površinsko aktivne. Rezultati AFM in SFG analize vzorcev monoslojev HDA molekul so pokazali, da je v grobem možno določiti ureditev in orientacijo molekul v monosloju, in to kljub številnim nehomogenostim, ki nastanejo med izdelavo takih tankih filmov.

PACS: 42.65.Ky, 61.30.Vx, 61.30.Hn, 64.70.M, 68.18.-g, 68.37.Ps, 68.47.Pe, 81.16.Dn

Ključne besede: Urejevalni sloji tekočih kristalov, podvajanje frekvenc (SHG), generacija vsote frekvenc (SFG), mikroskop na atomsko silo (AFM), gvanozin, Langmuir-Blodgett filmi.

Acknowledgments

First of all I am sincerely grateful to my adviser prof. dr. Irena Drevenšek-Olenik for her guidance and support. My special gratitude goes to prof. dr. Mischa Bonn from AMOLF Institute in Amsterdam, Netherlands, for offering me the opportunity to spend a fruitful time experimenting in his laboratory. I would also like to thank dr. Primož Kušar for his help at programming and for practical instructions during experimental work in the lab. I also thank to all my colleagues at the F7 department for all discussions and fun during my PhD at Jožef Stefan Institute. I would also like to express my gratitude to my family for continuous encouragement and understanding.
Last but not least, my heartfelt gratitude goes to my wife Menči and daughter Naja for their love and support during research work and patience during writing of the thesis.

Contents

Chapter 1

Introduction

Many phenomena in nature as well as in technological devices strongly depend on the properties and behavior of molecules near surfaces and interfaces. Optical techniques can serve as a convenient tool for surface and interface analysis, since they are nondestructive, noninvasive and allow the investigation of any surface or interface accessible to light. One group of surface sensitive optical techniques is based on nonlinear optical effects of second order, such as second-harmonic generation (SHG) and sum-frequency generation (SFG). Their important advantage with respect to conventional linear optical techniques like for instance IR spectroscopy, Raman spectroscopy and ellipsometry, is improved surface sensitivity. This is expressed particularly when probing materials with bulk centrosymmetric structure.

From the experimental point of view a number of optical techniques have been introduced for studying surfaces and interfaces. Nowadays most famous are certainly spectroscopic ellipsometry (SE), spectroscopic reflectometry (SR), and reflectance difference/anisotropy spectroscopy (RDS/RAS). The later operates on the principle that the bulk contribution to the near-normal-incidence reflectance of cubic materials is isotropic, thus the observed anisotropies can be attributed to the lower symmetry surface or interface. The information about surface or interface can also be obtained from the SE and SR data, but generally only after extensive modeling. This is a consequence of a relatively weak interaction of photons with the matter, since only a small fraction of reflected beam is influenced by the surface or interface. As rule of thumb the penetration depth usually ranges around 10 nm which is very large compared to 0.1 nm thickness of the surface region. The information is thus allocated roughly as 99% from the bulk and 1% from the surface.

Completely different story arises with nonlinear optical techniques of second order. This is because 2^{nd} order nonlinear optical effects are forbidden in the centrosymmetric bulk materials and allowed only at the surface/interface between two centrosymmetric materials, where the inversion symmetry is broken. As mentioned before, there are two very popular nonlinear optical techniques of second order i.e. SHG and SFG. The first can in general provide spectroscopic information on the electronic resonances of adsorbed molecules. However, for molecules adsorbed on the surface/interface, the detailed information on their surface arrangement is hidden in the vibrational rather than in the electronic modes. These vibrational modes have their resonance frequencies in the near- and mid-infrared spectral range. The availability of detectors in this spectral range is rather limited, but the so called IR-VIS SFG can be used to overcome this deficiency. In surface SFG experiments a fixed frequency high power visible laser beam is mixed

with a tunable high power IR beam. When using picosecond lasers, surface SFG spectra are collected by scanning the frequency of the IR beam. This need is overcome by the so-called broad bandwidth or multiplex SFG, in which the broad bandwidth femtosecond IR beams are used to cover a wide window of the vibrational spectrum, since all data points in the SFG spectra are collected under the same conditions. In the picosecond setup this is not true, because the IR beam is scanned over the spectrum region collecting each data point at different conditions. This is particularly important in the case of surface changing in time or monitoring some specific reactions that takes place on the surface.

In the thesis I present the development and assembling of second-harmonic generation and IR-VIS sum-frequency generation experimental techniques at the Jožef Stefan Institute in Ljubljana, Slovenia. The large part of my work was related to building up, adjusting, and calibrating of both setups, which are based on the ultrafast Ti:Sapphire laser system (Coherent) available at Complex Matter department. The calibrated setups were then used to perform the SHG investigation of surface layers for LC alignment and SFG studies of thin layers of biomolecules on different surfaces. In order to determine the surface topography of studied layers we used the Atomic Force Microscopy (AFM), which enables to distinguish between different types of surface structures developed during deposition. Part of the SFG results presented in the thesis was obtained during the visits to the AMOLF Institute in Amsterdam (The Netherlands).

The dissertation is divided into several chapters. In Chapter 2 a short theoretical introduction into non-linear optical techniques as surface specific tools is given. In chapter 3 a detailed description of SHG setup at the Jožef Stefan Institute with all experimental procedure, optical elements and detection system is given. Chapter 4 summarizes the results of investigation of electrically commanded surfaces for LC alignment. In chapter 5 a short description of Atomic Force Microscopy is given. Chapter 6 describes AFM investigation of surface structures of Guanosine 5′-monophosphate (GMP) on various substrates. The main focus is on GMP structures deposited on the mica substrate. In Chapter 7 the SFG setup at AMOLF institute with description of laser, optical, and detection systems is given. Chapter 8 is dedicated to SFG and AFM results obtained in comparative study of two different salts of GMP molecules on the mica and Au (111) substrates. Chapter 9 is continuation of chapter 7 by providing a description of the FID-SFG and frequency domain SFG setups assembled at the Jožef Stefan Institute. In chapter 10 the results of combined SFG and AFM investigation of monolayers of heptadecanoic acid in different environments, for instance in contact with water or various solid substrates, are presented. Chapter 11 summarizes the main findings and gives the conclusions of the dissertation.

Chapter 2

Theoretical background of optical nonlinearity

Nonlinear optical effects were known long before the invention of the laser, even though the observation of most of the nonlinear optical phenomena requires laser radiation. The Pockels and Kerr electro-optical effects [1] are examples of such phenomena. The invention of the laser in 1960 by Maiman contributed to the increase of research on nonlinear optical effects, such as second-harmonic generation, sum-frequency generation, stimulated Raman scattering, four-wave mixing, etc. The first nonlinear effect with laser radiation was observed by Franken in 1961 on a quartz crystal. They used a ruby-laser with a wavelength of 694.2 nm to generate second harmonic radiation at 347.1 nm. From the pioneering work of Franken in 1961 the field of non-linear optics has developed and became one of the most interesting areas in applied and also in basic science [2].
To describe nonlinear optical phenomena it is natural to start from Maxwell equations, which serve as general laws of electric and magnetic effects in matter

$$\nabla \times \mathbf{E} = -\frac{\partial \mathbf{B}}{\partial t}, \tag{1}$$

$$\nabla \times \mathbf{B} = \mu_0 \varepsilon_0 \frac{\partial \mathbf{E}}{\partial t} + \mu_0 \mathbf{j}, \tag{2}$$

$$\nabla \cdot \mathbf{E} = \frac{\rho}{\varepsilon_0}, \tag{3}$$

$$\nabla \cdot \mathbf{B} = 0, \tag{4}$$

where **E** and **B** are the electric and the magnetic fields and j and ρ are the current and charge densities in matter, respectively. The last two equations are linked by the so called law of charge conservation. In general one can expand j and ρ in terms of electric multipole moments, while the magnetic multipole moments can be neglected since optical media are generally nonmagnetic. Taking into account only the electric dipole moment approximation it follows

$$\rho = \rho_0 - \nabla \cdot \mathbf{P}, \tag{5}$$

$$\mathbf{j} = \mathbf{j}_0 + \frac{\partial \mathbf{P}}{\partial t}, \tag{6}$$

where ρ_0 is the free electric charge, j_0 is the free current density and **P** is the electric dipole moment per unit volume (also known as polartization). The assumption that there is no free electric charge and free electric current gives $\rho_0 = 0$ and $j_0 = 0$. Considering all these assumptions eq. (3) can be rewritten into

$$\nabla \cdot \mathbf{E} + \frac{1}{\varepsilon_0} \nabla \cdot \mathbf{P} = 0. \tag{7}$$

Combining eq. (1) and (2) one gets the wave equation

$$\nabla^2 \mathbf{E} - \nabla(\nabla \cdot \mathbf{E}) - \mu_0 \varepsilon_0 \frac{\partial^2 \mathbf{E}}{\partial t^2} - \mu_0 \frac{\partial^2 \mathbf{P}}{\partial t^2} = 0. \tag{8}$$

The polarization **P** can now be written in terms of linear and nonlinear part of polarization

$$\mathbf{P} = \mathbf{P}_l + \mathbf{P}_{nl}. \tag{9}$$

The linear part is basicly linked to the linear-optical phenomena (scattering, reflection, refraction, etc), which means that the optical properties of the medium are independent of the field intensity. The relation can be written in frequency domain as

$$\mathbf{P}_l(\omega) = \mathbf{P}^{(0)} + (\varepsilon - 1)\mathbf{E}(\omega) = \mathbf{P}^{(0)} + \chi^{(1)}\mathbf{E}(\omega), \tag{10}$$

where $\mathbf{P}^{(0)}$ is the permanent polarization, ε is the dielectric constant of the medium, and $\chi^{(1)}$ is the linear susceptibility (polarizability). ω is the frequency of the electomagnetic radiation that interacts with the medium.
The nonlinear part of polarization can be expanded into power series of electric field

$$\mathbf{P}_{nl} = \mathbf{P}^{(2)} + \mathbf{P}^{(3)} + \mathbf{P}^{(4)} + \ldots, \tag{11}$$

$$\mathbf{P}^{(2)}(\omega) = \chi^{(2)}(\omega = \omega_1 \pm \omega_2) : \mathbf{E}(\omega_1)\mathbf{E}(\omega_2), \tag{12}$$

$$\mathbf{P}^{(3)}(\omega) = \chi^{(3)}(\omega = \omega_1 \pm \omega_2 \pm \omega_3) \vdots \mathbf{E}(\omega_1)\mathbf{E}(\omega_2)\mathbf{E}(\omega_3). \tag{13}$$

The first term in the nonlinear polarization represents nonlinear optical processes of second order. If we put $\omega_1 = \omega_2 = \omega_0$ in (12) we get $\omega = 2\omega_0$ which is the process of second-harmonic generation (SHG). In the more general case of three-wave-mixing configuration, where $\omega = \omega_1 + \omega_2$ or $\omega = \omega_1 - \omega_2$, the second order polarization produces the processes of sum-frequency generation (SFG) and difference-frequency generation (DFG), respectively.

Equation (13) represents nonlinear optical processes of third order, such as self-focusing, self-phase modulation, four wave mixing, stimulated Raman scattering, optical Kerr effect and related phenomena. It describes also the process of third-harmonic generation (THG) in which the 3rd order susceptibility corresponds to $\chi^{(3)} = \chi^{(3)}(\omega\,;\,\omega_0 = \omega_1 = \omega_2 = \omega_3)$ and the energy conservation meets with $\omega = 3\omega_0$ [3].

2.1 The second order nonlinear optical susceptibility

In the following section we will mainly focus on the nonlinear processes of second order. First, it is worth mentioning that in general all even-order nonlinear sceptibilities exist only in non-centrosymmetric media or in the media where the inversion symmetry is broken (this includes also surfaces and interfaces). This can be proven by a simple consideration. If we take eq. (12) and make the spatial inversion by introducing operator $\hat{\mathrm{I}}$ we get the following relation

$$\begin{aligned}\hat{\mathrm{I}}P_i^{(2)}(\omega) &= \hat{\mathrm{I}}\chi_{ijk}^{(2)}(\omega\,;\omega_1,\omega_2,\mathrm{r})\hat{\mathrm{I}}\left(E_j(\omega_1,\mathrm{r})\right)\hat{\mathrm{I}}\left(E_k(\omega_2,\mathrm{r})\right)\\ &= \chi_{ijk}^{(2)}(\omega\,;\omega_1,\omega_2,\mathrm{r})\left(-E_j(\omega_1,\mathrm{r})\right)\left(-E_k(\omega_2,\mathrm{r})\right)\\ &= P_i^{(2)}(\omega)\end{aligned} \tag{14}$$

Relation (14) indicates that in centrosymmetric media the even orders of polarization must be identically zero.
In general the nonlinear susceptibility of second order $\chi^{(2)}$ is a tensor with 27 independent components. Introducing several symmetry rules the number of independent components can be reduced. The product of electric fields in the eq. (14) is identical to exchanging E_jE_k with E_kE_j. This gives

$$\chi_{ijk}^{(2)}(\omega\,;\omega_1,\omega_2) = \chi_{ikj}^{(2)}(\omega\,;\omega_2,\omega_1), \tag{15}$$

which can be extended in non-absorbing media to the so-called full permutation symmetry. This means that all the frequency arguments in a nonlinear susceptibility tensor are interchangeable as long as the corresponding coordinate indices are interchanged accordingly. This is also known as Kleinman symmetry rule [4]. According to this symmetry the relations for the components of the second-order nonlinear susceptibility are as follows

$$\begin{aligned}\chi_{ijk}^{(2)}(\omega\,;\omega_1,\omega_2) &= \chi_{jik}^{(2)}(\omega_1\,;\omega\,,\omega_2) = \chi_{jki}^{(2)}(\omega_1\,;\omega_2,\omega)\\ &= \chi_{kij}^{(2)}(\omega_2;\omega\,,\omega_1) = \chi_{kji}^{(2)}(\omega_2;\,\omega_1,\omega).\end{aligned} \tag{16}$$

Further, the total number of independent components of second-order nonlinear susceptibility is reduced by taking into account the symmetry properties of the probed surface. For instance for an isotropic surface the susceptibility tensor $\chi^{(2)}$ is necessarily independent of the azimuthal orientation of the frame of reference in which it is

evaluated. From a total of 27 components only seven are nonzero in any Cartesian basis (x, y, z) [5] in which z axis represents the symmetry axis for $C_{\infty v}$ symmetry group:

$$\chi^{(2)}_{zzz}, \chi^{(2)}_{xxz} = \chi^{(2)}_{yyz}, \chi^{(2)}_{xzx} = \chi^{(2)}_{yzy}, \chi^{(2)}_{zxx} = \chi^{(2)}_{zyy}. \tag{17}$$

We can now discuss also the surface with C_{1v} symmetry. Such a symmetry corresponds to the rubbed polymer surface. Therefore the nonlinear susceptibility has 10 non-vanishing independent elements

$$\chi^{(2)}_{xxz}, \chi^{(2)}_{yyz}, \chi^{(2)}_{zzz}, \chi^{(2)}_{xzx} = \chi^{(2)}_{zxx}, \chi^{(2)}_{yzy} = \chi^{(2)}_{zyy}, \chi^{(2)}_{xxx}, \chi^{(2)}_{yyx}, \chi^{(2)}_{zzx}, \chi^{(2)}_{xyy} = \chi^{(2)}_{yxy}, \chi^{(2)}_{xzz} = \chi^{(2)}_{zxz}. \tag{18}$$

2.1.1 Microscopic theory

Inorganic materials such as conductors or semiconductors have a crystalline structure in which the atoms strongly interact with each other to form a macroscopic network. In such complex system the nonlinear optical response may be calculated by various simplified models based on a structural symmetry of the system. On the contrary, organic materials are usually composed of molecules, which weakly interact with each other to form molecular crystals. The intermolecular interactions are of Van der Waals type and hence weak compared to the intramolecular interactions. Thus molecular crystals can be considered as systems of weakly interacting entities that independently respond to the influence of an external electromagnetic field. The macroscopic susceptibility $\chi^{(2)}$ introduced in the previous section can be related to the microscopic molecular susceptibility $\beta^{(2)}$

$$\chi^{(2)}_{ijk} = N\langle\beta\rangle_{ijk} = N\int f(\Omega)\; a_{iI}a_{jJ}a_{kK}\tilde{\beta}_{IJK}d\Omega, \tag{19}$$

where N is the number of molecules per unit volume, a is the transformation matrix from the molecular to the laboratory system and $f(\mathbf{\Omega})$ is angular distribution functions. The curved brackets represent the average over all possible orientations of the molecules within macroscopic phase. The molecules can be preferentially oriented or fixed in space for instance as in the case of Langmuir Blodgett films or rubbed polymer surfaces. Therefore the understanding of microscopic molecular susceptibilities and the orientational distribution of the molecules can be used to predict the macroscopic susceptibilities [3].

2.1.2 Second-harmonic generation (SHG) and sum-frequency generation (SFG) at surfaces and interfaces

In this thesis the emphasis is on the SHG and SFG as the tools for investigating the surfaces and interfaces between two centrosymmetric media. The second harmonic

generation at surfaces and interfaces was discovered by R. W. Terhune, P. D. Maker, and C. M. Savage working for the Ford Motor Company in 1962, which is one year after Franken made the first Second-harmonic generation experiment in bulk material. Terhune et al. observed that calcite, although it was a centrosymmetric material, produced SHG signal when exposed to an external electric field. In 1968 Bloembergen et.al. showed that the SHG signal from calcite and many other centrosymmetric materials actually originates from the surface [6].

The advantages of SHG and SFG techniques and all the optical techniques in general are their nondestructive nature and the ability to investigate any surface or interface accessible to light. With SHG and SFG the information about the surface structure, molecular orientation, and chemical composition can be deduced. Until now the surface investigations based on SHG and SFG have expanded on several fields such as investigations of semiconductors [7], isolators [8], magnetic materials [9], polymers [10,11], bio-surfaces and bio-interfaces [12], biological membranes [13,14] and liquid surfaces [15].

In the previous sections we derived the wave equation for the electromagnetic waves propagating through the bulk medium. Taking into account the relation (9) and combining it with the equation (8) leads to the wave equation for nonlinear medium in the electric dipole approximation

$$\nabla^2\mathbf{E} - \nabla(\nabla\cdot\mathbf{E}) - \mu_0\varepsilon_0\varepsilon\frac{\partial^2\mathbf{E}}{\partial t^2} = \mu_0\frac{\partial^2\mathbf{P}_{nl}}{\partial t^2}. \tag{20}$$

where the assumption of an isotropic medium with dielectric constant ε has been taken into account ($\mathbf{P}_l = 0$) The right hand side of the equation (20) plays the role of a driving source to induce an electromagnetic wave with the same frequency ω as $\mathbf{P}_{nl}$. Equation (20) can be simplified if the net free charge is 0 ($\rho_0 = 0$), which gives according to (3) the following wave equation in non-linear media

$$\nabla^2\mathbf{E} - \mu_0\varepsilon_0\varepsilon\frac{\partial^2\mathbf{E}}{\partial t^2} = \mu_0\frac{\partial^2\mathbf{P}_{nl}}{\partial t^2}. \tag{21}$$

We assume that the incident electric field and the nonlinear polarization have the form of monochromatic plane waves propagating only in the z direction:

$$\begin{aligned} E_i(z,t) &= E_{i0}e^{i(k_i z-\omega_i t)}, \\ P_{nl}(z,t) &= P_{nl0}(z)e^{-i\omega_3 t}, \\ P_{nl0} &= 4d_{eff}E_{01}E_{02}e^{i(k_1+k_2)z}, \end{aligned} \tag{22}$$

where k_i and ω_i represents the wave vector of the i-th electromagnetic wave (indices 1, 2 and 3 signify both fundamental EM waves and the SFG wave respectively in the case of sum-frequency generation). E_{01} and E_{02} are amplitudes of both fundamental EM waves. The constant d_{eff} is related to nonlinear susceptibility and is obtained by summation over

all components of nonlinear susceptibility that contributes to the nonlinear response (see eq. (12)). We are interested in the wave equation for the $\omega_3 = \omega_1 + \omega_2$ (or $\omega_3 = 2\omega_1$) component which signifies the SFG (or SHG), respectively. Expanding the equation (21) by considering equation (22) gives

$$\left(\frac{d^2E_{30}}{dz^2} + 2ik_3\frac{dE_{30}}{dz} - k_3^2E_{30} + \frac{\omega_3^2E_{30}}{c^2}\right)e^{i(k_3z-\omega_3t)} = -\mu_0 d_{eff}\omega_3^2E_{10}E_{20}e^{i((k_1+k_2)z-\omega_3t)} \tag{23}$$

Supposing that the amplitude E_{30} is the slowly varying amplitude which in other words means that the fractional change of the amplitude does not change significantly in a distance of an optical wavelength

$$\left|\frac{d^2E_{30}}{dz^2}\right| \ll \left|k_3\frac{dE_{30}}{dz}\right|, \tag{24}$$

the eq. (23) can be simplified

$$\frac{dE_{30}}{dz} = \frac{i\mu_0 d_{eff}\omega_3^2}{2k_3}E_{10}E_{20}e^{i\Delta kz}, \tag{25}$$

where $\Delta k = k_1+k_2-k_3$ is the wave vector mismatch. Equation similar to (25) can be derived also for the amplitudes E_{10} and E_{20}. In order to solve the eq. (25) we will consider E_{10} and E_{20} as constant amplitudes. For easier calculation we will hide all constants under A. The integration over whole nonlinear medium gives

$$E_{30} = A\int_0^l e^{i\Delta kz}dz = A\left(\frac{e^{i\Delta kl}-1}{i\Delta k}\right). \tag{26}$$

The SFG intensity can be obtained by the magnitude of the time-averaged Poynting vector

$$I_{30} = \frac{\varepsilon_0 c}{2}\left|E_{30}^2\right| = \frac{\varepsilon_0 cA^2}{2}\left|\frac{e^{i\Delta kl}-1}{\Delta k}\right|^2 = \frac{\varepsilon_0 cA^2l^2}{2}\frac{\sin^2(\Delta kl/2)}{(\Delta kl/2)^2}. \tag{27}$$

The expression (27) has its maximum value when the $\Delta kl/2 = 0$ which is the so-called phase matching condition:

$$\mathbf{k}_3 = \mathbf{k}_1 + \mathbf{k}_2. \tag{28}$$

The major difference between the SFG and SHG with respect to other optical techniques is their property of being surface or interface sensitive. The thickness of the interface

(surface) is usually much smaller than the wavelength of the probing electromagnetic wave ($d<<\lambda$), so the model of taking interfacial region as infinitely thin layer is reasonable [16,17]. The nonlinear response is represented as a sheet of nonlinear polarization $\mathbf{P}^{\mathbf{NLS}}$, placed in between the centrosymmetric medium 1 and medium 2, which are isotropic in terms of linear optical properties. They are described by the following dielectric constants: ε', ε_1, and ε_2 (see Figure 2-1).

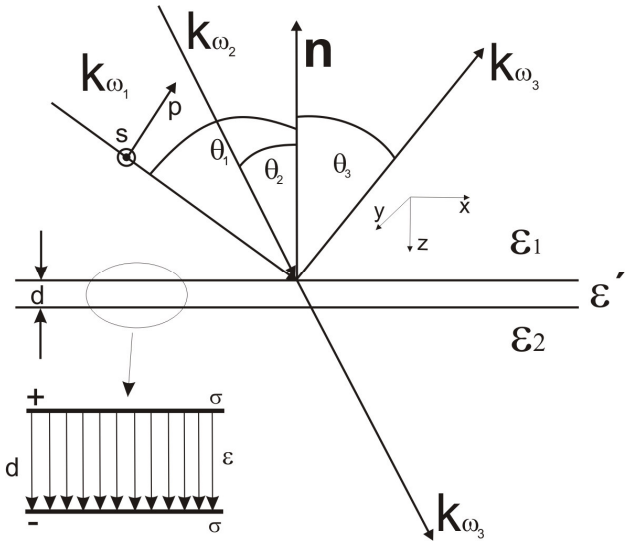

Figure 2-1: The scheme of the nonlinear optical effects at the surface (interface) between two isotropic media where the boundary is treated as a surface (interface) capacitor.

We will try to determine the radiation field emanating from the interface between two isotropic media. If we consider a 2D sheet of polarization located at the interface, the surface charge density σ can be associated as: $\sigma = -\nabla_{||} \cdot \mathbf{P}^{\mathbf{NLS}}$, where $\nabla_{||}$ denotes the component of the divergence operator parallel with the interface. Similarly can be defined also the surface current density $\mathbf{J}_s = \partial \mathbf{P}_{||}^{\mathbf{NLS}} / \partial t$. Surface charge density can be rewritten in terms of electrical field density as $\sigma = \varepsilon_0(\mathbf{E}(z=0^+)-\mathbf{E}(z=0^-))\cdot\mathbf{n}$, where $\mathbf{n}$ is the surface normal along the z axis (the origin is at the interface). Integration of Maxwell equation (3) over a very small pillbox (Figure 2-1) gives the matching condition:

$$\varepsilon_0 \left(\mathbf{E}\left(z=0^+\right) - \mathbf{E}\left(z=0^-\right) \right) \cdot \mathbf{n} = \sigma = -\nabla_{||} \mathbf{P}^{\mathbf{NLS}} \tag{29}$$

The second matching condition for the tangential component of magnetic field $\mathbf{B}$ can be derived from the Maxwell equation (2) and surface current density $\mathbf{J}_s$ at the interface or surface:

$$\mathbf{n} \times \left(\mathbf{B}\left(z=0^+\right) - \mathbf{B}\left(z=0^-\right) \right) = \mu_0 \mathbf{J}_s = \mu_0 \frac{\partial \mathbf{P}_{||}^{\mathbf{NLS}}}{\partial t} \tag{30}$$

The perpendicular part of nonlinear polarization $\mathbf{P}^{\mathbf{NLS}}$ can be treated as a surface capacitor with a surface charge density σ separated over distance d (Figure 2-1). Thus the z component of the nonlinear polarization can be written as $P_z^{NLS} = \sigma d$. The potential difference in this case would be $\Delta U = \sigma d/(\varepsilon' \varepsilon_0) = P_z^{NLS}/(\varepsilon' \varepsilon_0)$. The parallel components of the electric field experience a jump across the boundary in a way $\Delta \boldsymbol{E} = -\nabla_{||} \Delta U$, which yields the last matching condition for the tangential components of the electric field (E_x and E_y).

According to the relations in (29) and (30) and the relations obtained in the last paragraph we can derive the matching conditions of the electric and magnetic fields at the boundary between two isotropic media

$$\begin{aligned}
&\Delta D_z\big|_{z=0} = -\nabla_{\parallel} \cdot \mathbf{P}^{NLS}, \\
&\Delta B_z\big|_{z=0} = 0, \\
&\Delta H_x\big|_{z=0} = \frac{\partial P_y^{NLS}}{\partial t};\ \Delta H_y\big|_{z=0} = -\frac{\partial P_x^{NLS}}{\partial t}, \\
&\Delta E_x\big|_{z=0} = -\frac{1}{\varepsilon' \varepsilon_0}\frac{\partial P_z^{NLS}}{\partial x};\ \Delta E_y\big|_{z=0} = -\frac{1}{\varepsilon' \varepsilon_0}\frac{\partial P_z^{NLS}}{\partial y}.
\end{aligned} \tag{31}$$

First we have to derive the fields radiated from a polarized sheet at the interface between medium 1 and medium 2. We consider the thin layer between both media as $\mathbf{P}^{\mathbf{NL}}(x,y,z,t) = \mathbf{P}^{\mathbf{NLS}}(x,y,t)\delta(z)$ where $\mathbf{P}^{\mathbf{NLS}}(x,y,t) = \mathbf{P_s} e^{ik_x x - i\omega_3 t} + c.c.$ is a polarized sheet and *c.c.* represents complex conjugate term. We take the xz plane as plane of incidence. The wave vector of reflected beam in medium 1 and transmitted beam in medium 2 can be according to the dispersion relation written as

$$\begin{aligned}
&\mathbf{k}_1 = k_x \mathbf{e_x} - \sqrt{\varepsilon_1 k_{0_1}^2 - k_x^2}\,\mathbf{e_z}, \\
&\mathbf{k}_2 = k_x \mathbf{e_x} + \sqrt{\varepsilon_2 k_{0_2}^2 - k_x^2}\,\mathbf{e_z},
\end{aligned} \tag{32}$$

where $k_{0i} = \omega_i/c$ is the wave vector at the appropriate frequency ω_i calculated in the free space. From the boundary conditions (31) we can derive the expressions for the radiated fields from the interface. The electric fields with plane wave characterization close to the polarized sheet on either side are as follows

$$\begin{aligned}
&\mathbf{E}_i(x,y,z,t) = \mathbf{E}_i(\omega_3) e^{i\mathbf{k}_i \cdot \mathbf{x} - i\omega_3 t} + c.c. \\
&\mathbf{E}_i(\omega_3) = \frac{ik_0^2}{\sqrt{\varepsilon_i k_0^2 - k_x^2}}\left[\mathbf{P_s} - \mathbf{k}_i(\mathbf{k}_i \cdot \mathbf{P_s})\right].
\end{aligned} \tag{33}$$

where $\mathbf{k}_{1,2}$ is the unit wave vector along the direction of propagation . The expression (33) can be written in terms of a unit polarization vector $\hat{\boldsymbol{e}}_i$ ($\mathbf{k}_i \cdot \hat{\boldsymbol{e}}_i = \mathbf{0}$) which gives the following expression:

$$\hat{\boldsymbol{e}}_i \cdot \mathbf{E}_i = \frac{ik_0^2}{\sqrt{\varepsilon_i k_0^2 - k_x^2}} \left(\left(\mathbf{F} \hat{\boldsymbol{e}}_i \right) \cdot \mathbf{P}_\mathbf{s} \right) \tag{34}$$

The polarization vectors from medium 1 to medium 2 are transformed correspondingly $\boldsymbol{e}_i = \mathbf{F} \cdot \hat{\boldsymbol{e}}_i$, where $\mathbf{F}$ is the Fresnel transformation matrix for polarization vectors $\hat{\boldsymbol{e}}_i$ that relates the fields in medium 2 to the ones in medium 1. For s- (polarization perpendicular to the plane of incidence) and p- (polarization in the plane of incidence) polarized light we obtain the following relations for the radiated fields in medium 1:

$$\begin{aligned} E_{s1} &= \frac{ik_0^2}{\sqrt{\varepsilon_1 k_0^2 - k_x^2}} F_{1\to 2}^{yy} P_y^{NLS}, \\ E_{p1} &= \frac{ik_0^2}{\sqrt{\varepsilon_1 k_0^2 - k_x^2}} \left(F_{1\to 2}^{xx} P_x^{NLS} + F_{1\to 2}^{zz} P_z^{NLS} \right). \end{aligned} \tag{35}$$

The non-zero *F*-factor for s- and p- polarized light from medium 1 to medium 2 are expressed as

$$\begin{aligned} F_{1\to 2}^{xx} &= \frac{2\varepsilon_1 \sqrt{\varepsilon_2 k_{0_2}^2 - k_x^2}}{\left(\varepsilon_2 \sqrt{\varepsilon_1 k_{0_1}^2 - k_x^2} + \varepsilon_1 \sqrt{\varepsilon_2 k_{0_2}^2 - k_x^2} \right)} \\ F_{1\to 2}^{yy} &= \frac{2\sqrt{\varepsilon_1 k_{0_1}^2 - k_x^2}}{\left(\sqrt{\varepsilon_1 k_{0_1}^2 - k_x^2} + \sqrt{\varepsilon_2 k_{0_2}^2 - k_x^2} \right)} \\ F_{1\to 2}^{zz} &= \frac{2\left(\frac{\varepsilon_1 \varepsilon_2}{\varepsilon'} \right) \sqrt{\varepsilon_1 k_{0_1}^2 - k_x^2}}{\left(\varepsilon_2 \sqrt{\varepsilon_1 k_{0_1}^2 - k_x^2} + \varepsilon_1 \sqrt{\varepsilon_2 k_{0_2}^2 - k_x^2} \right)} \end{aligned} \tag{36}$$

In order to formulate the nonlinear optical effects within this phenomenological model the nonlinear polarized sheet will be treated in terms of surface susceptibility $\chi^{(2)}$, $\mathbf{P}_\mathbf{s}(\omega_3) = \chi^{(2)}(\omega_3 = \omega_1 \pm \omega_2) : \mathbf{E}(\omega_1)\mathbf{E}(\omega_2)$. The $\mathbf{E}$ fields are evaluated in the boundary with dielectric constant ε' thus it is necessary to relate those fields to the applied fields. We will consider our waves as plane waves

$$\begin{aligned} \mathbf{E}_i(x, y, z, t) &= \mathbf{E}_i(\omega) e^{i\mathbf{k}_i \cdot \mathbf{x} - i\omega_i t} + c.c. \\ &= E_i(\omega) \hat{\boldsymbol{e}}_i \; e^{i\mathbf{k}_i \cdot \mathbf{x} - i\omega_i t} + c.c., \end{aligned} \tag{37}$$

where ω_i and $\hat{\boldsymbol{e}}_i$ are a frequency and a polarization vector of the pumping fields, respectively. The wave vectors can be written in similar relations to (32)

$$\begin{aligned}\mathbf{k}_1 &= k_x\mathbf{e_x} + \sqrt{\varepsilon_1\left(\omega_1/c\right)^2 - k_x^2}\,\mathbf{e_z},\\ \mathbf{k}_2 &= k_x\mathbf{e_x} - \sqrt{\varepsilon_2\left(\omega_2/c\right)^2 - k_x^2}\,\mathbf{e_z},\end{aligned} \tag{38}$$

where we again assumed the incident beams propagation in the xz plane. The surface polarization $\mathbf{P_s}$ can than be written in terms of incident pump beams as

$$\mathbf{P_s}(\omega_3) = \chi^{(2)}(\omega_3 = \omega_1 \pm \omega_2) : \boldsymbol{e}_i\left(\omega_1\right)\boldsymbol{e}_j\left(\omega_2\right)\mathbf{E}_i(\omega_1)\mathbf{E}_j(\omega_2), \tag{39}$$

where $\boldsymbol{e}_i$ vectors represent polarization vectors of the pump fields corrected for Fresnel factor describing propagation into the interfacial region. By considering the relations (34) and (39)

$$\hat{\boldsymbol{e}}_i\left(\omega_3\right)\cdot\mathbf{E}_i\left(\omega_3\right) = \frac{i\omega_3^2}{c^2\sqrt{\varepsilon_i k_0^2 - k_x^2}}\left[\boldsymbol{e}\left(\omega_3\right)\cdot\chi^{(2)} : \mathbf{e}_i\left(\omega_1\right)\mathbf{e}_j\left(\omega_2\right)\right]E_i(\omega_1)E_j(\omega_2). \tag{40}$$

This relation describes the radiated field $\mathbf{E}_i$ with polarization vector $\hat{\boldsymbol{e}}_i\left(\omega_3\right)$ in either medium 1 or 2 produced by excitation from fields $\hat{\boldsymbol{e}}_i\left(\omega_1\right)E_i(\omega_1)$ and $\hat{\boldsymbol{e}}_j\left(\omega_2\right)E_j(\omega_2)$ propagating towards the interface in media *i* and *j*. By considering the nonzero elements of $\chi^{(2)}$ for isotropic surface or interface (subsection 2.1.1) one obtains four nonzero electric fields for all polarization combinations, i.e. ppp, ssp, pss, and sps. The other four, namely spp, psp, sss, and pps, are zero and thus forbidden for isotropic surfaces (interfaces) [5].
We can now write the phase matching condition (28) for the surface or interface

$$k_{x_3} = k_{x_1} + k_{x_2}, \tag{41}$$

where k_{x_i} are in-plane wave vector components of the pumping and radiated fields. The phase matching can be also written in terms of angles of incidence

$$k_3\sin(\theta_3) = k_1\sin(\theta_1) + k_2\sin(\theta_2). \tag{42}$$

We will now proceed to the next chapter in which the short description of the SHG experimental setup at the Jožef Stefan Institute in Ljubljana will be given.

Chapter 3

Experiment of second harmonic generation

Figure 3-1 schematically shows the SHG experimental setup. The sample is irradiated with an optical pulse generated in the Mira-RegA laser system (Coherent, St. Clara, CA, USA). A laser beam was directed through a half wave-plate, polarizer and lens (f = 1 m) to the sample mounted in transmission geometry. SHG signal was collected with the lens (f = 15 cm), refocused with an additional lens (f = 20 cm), and then sent to the photomultiplier tube (PMT) operating in the photon counting regime.

3.1 Mira-RegA laser system

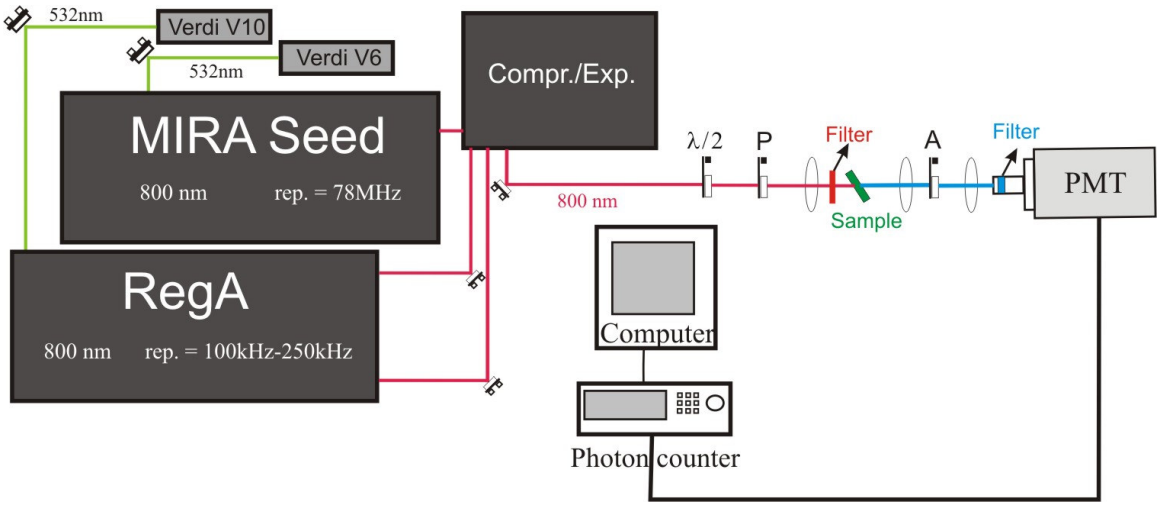

Figure 3-1: Experimental setup for Second harmonic generation.

The Mira laser is a commercially available mode-locked titanium sapphire oscillator operating at the fundamental wavelength of 804 nm. Mira is pumped by a diode pumped Nd:YAG (Coherent Verdi 6) continuous wave (CW) laser operating at wavelength of 532 nm with an average power of 5 W. In the Mira-RegA laser system Mira serves as a seed for laser pulses with a repetition rate of 78 MHz and 10 nJ of average energy per pulse. The time duration of a single laser pulse is about 80 fs. Laser pulse from Mira is then directed into the RegA titanium sapphire amplifier. RegA is pumped by a Nd:YAG (Coherent Verdi 10) CW laser operating at 532 nm with an average power of 10 W.

Pulses obtained from the RegA have a tunable repetition rate in the range 100 – 250 kHz with 3.6 μJ – 6 μJ of energy per pulse. RegA pulses have a spectral bandwidth of approximately 26 nm with a central wavelength at 804 nm. SHG measurements were performed with typically 0.6 – 0.8 μJ of energy per pulse.

After a proper spectral filtering (to remove the SHG signal generated in optical elements prior to the sample and to filter out the fundamental beam after the sample) the SHG signal emanating from the sample was detected by photomultiplier tube (PMT) operating in the gated photon counting regime. Gated photon counting regime operates in such a way that the detection is synchronized with the laser amplifier system.

3.2 Photomultiplier tube

As a detector in SHG setup we used a commercially available PMT purchased from Electron Tubes, UK. We used the model 9893/350B with blue-green sensitive photocathode and 14 BeCu dynodes of linear focused design for fast timing and extended linearity. The active diameter of this PMT was 9 mm and the quantum efficiency at 400 nm was 25%. PMT was cooled down to -20ºC in order to reduce dark current down to a couple of counts per second. Typical spectral response and voltage gain characteristics are shown on Figure 3-2.

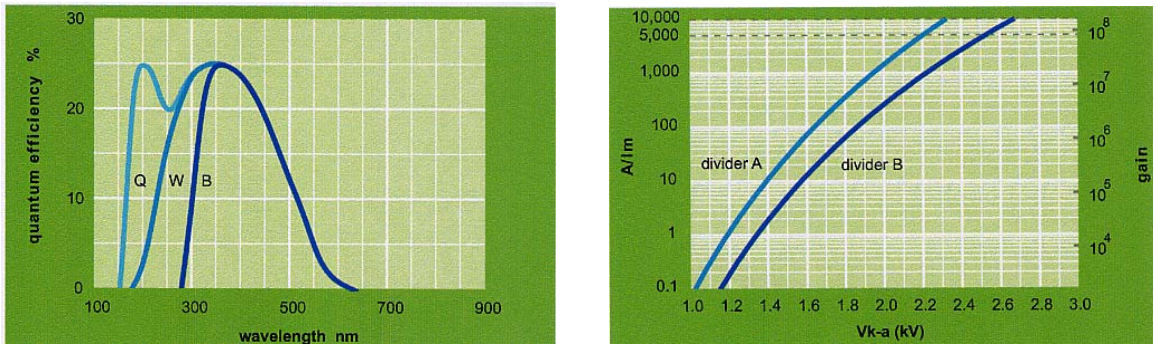

Figure 3-2: The spectral response (left) and voltage gain (right) characteristics for PMT 9893/350B [Electron tubes].

3.3 Photon counting

The signal detected by PMT was amplified by Stanford Research SR 440 voltage amplifier and collected with the Stanford Research SR 400 Photon Counter operating in the gated regime. The gating regime was synchronized with the RegA repetition rate in order to detect only the events related to the second-harmonic generation. Time delay between the SHG signal and the trigger pulse from the laser was 1.423 μs. The width of the detection gate was fixed to 5 ns to filter out long-lived multi-photonic events such as two-photon fluorescence. To increase the signal/noise ratio and to filter out afterpulsing signal, the level of the discriminator was adjusted to 0.026 V. An additional improvement

in order to filter out two photonic fluorescence is the insertion of a monochromator or a band pass filter into the detection part of the SHG experiment [17].

Chapter 4

Electrically commanded surfaces

In the following chapter the results of the SHG investigation used to probe the dynamic response of siloxane-based side chain ferroelectric liquid crystal polymer (FLCP) utilized as an alignment layer for liquid crystal displays (LCDs) are presented. The emphasis of our study was on the field-induced modification of the nonlinear optical susceptibility and on the switching dynamics of the SHG response. We investigated also the temperature dependence of the SHG signal through-out the LC phase transition from the SmC* to the SmA* phase.

4.1 Liquid crystals

In general there are three phases of matter, i.e. gas, liquid and solid [16]. All these states are generally distinguished by the degree of translational and orientational order of the constituent parts (molecules, atoms). On the basis of orientational order some phases can be further subdivided, for instance a solid can be crystalline or amorphous. An example for the later is glass, in which the molecules are fixed in place without a pattern in their arrangement. On the other hand the crystalline solid state possesses long-range translational and long-range orientational order of the constituent atoms (molecules). This means that constituent atoms (molecules) occupy specific positions in space and orient themselves with respect to each other. However, there exist a group of materials with mesomorphism which means that they are in the state with positional and orientational order somewhere between liquid and solid crystalline phase. Such phases are commonly known as liquid crystals (LCs). These materials most commonly consist of elongated (rod-like) molecules with highly anisotropic physical properties. Liquid crystals can be subdivided on the basis of their degree of order into two major subphases. The first one is *nematic* (Figure 4-1 (a)) and the other is *smectic* (Figure 4-1 (b)) phase.

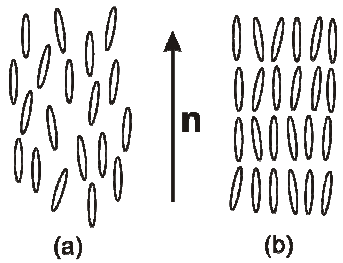

Figure 4-1: Schematic drawing of (a) nematic and (b) smectic LC phases. Vector **n** represents the preferred orientation direction of the LC molecules.

In order to represent the direction of preferred orientation of molecules in the neighborhood of any point a unit vector **n**, called the *director*, is commonly used in the LC community. The director is presented in Figure 4-1 showing the preferred molecular orientation.
Nematic phase is close to the isotropic (liquid) phase, because the molecules possess only orientational order, whereas the position of their centers of gravity is random. In the smectic phase the LC molecules possess positional order in one or two dimensions, rather than three as in the crystalline phase and they are also preferentially aligned along one direction. The smectic phase can be further divided into SmA* and SmC* phase.
In the SmA* phase the director is parallel with the smectic layer normal. On the contrary in the SmC* phase the director is tilted away from the smectic layer normal. Molecules consistuing SmC* phase are chiral which gives the SmC* phase ferroelectric properties with nonzero spontaneous polarization (see Figure 4-4). The local point symmetry of SmC* phase is C_2 with two fold axis of rotation being perpendicular to the director. This direction also corresponds to the direction of the net spontaneous polarization. All these properties make SmC* phase SHG active in the dipole aproximation. Since the SmC* phase possesses C_2 symmetry the corresponding nonlinear susceptibility tensor has four nonzero components (two fold axis concide with y axis - Figure 4-3 (b)):

$$\chi^{(2)}_{xxy} = \chi^{(2)}_{xyx} = \chi^{(2)}_{yxx},\ \chi^{(2)}_{xyz} = \chi^{(2)}_{xzy} = \chi^{(2)}_{yxz} = \chi^{(2)}_{yzx} = \chi^{(2)}_{zxy} = \chi^{(2)}_{zyx},\ \chi^{(2)}_{yzz} = \chi^{(2)}_{zyz} = \chi^{(2)}_{yzz},\ \text{and}\ \chi^{(2)}_{yyy}.$$

4.2 Alignment layers

Electrically Commanded Surfaces (ECS) are a novel type of alignment layers for LCDs, which are based on the concept that the electric field induced molecular reorientation in the surface layer is transferred to the bulk nematic LC via elastic forces [19]. In the conventional LCDs the electro-optic effect is based upon the coupling between LC physical properties (dielectric anisotropy) and the external electric field (see Figure 4-2).

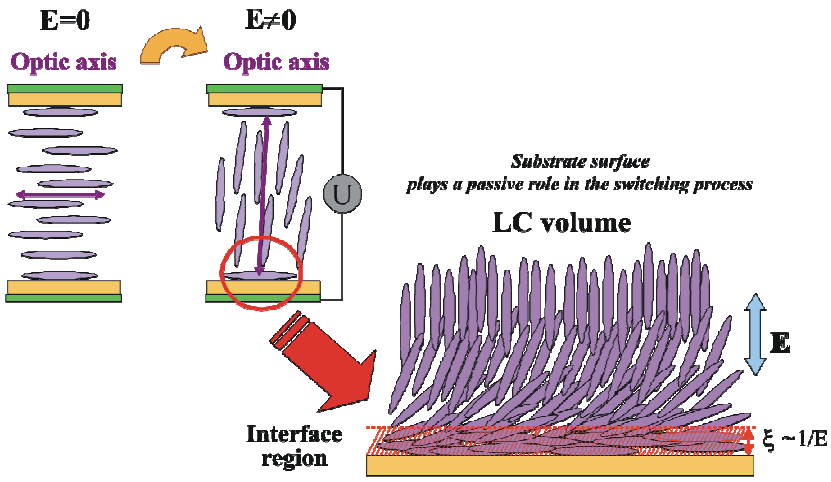

Figure 4-2: The switching process in the conventional LCD.

Basically the reorientation of LC molecules only takes place in the bulk whereas the LC/solid surface regions stay unaffected due to strong anchoring. If the LC molecular anisotropy defined as $\Delta\varepsilon = \varepsilon_{||} - \varepsilon_{\perp}$ (where $\varepsilon_{||}$ and $\varepsilon_{\perp}$ are dielectric constant along and perpendicular to the direction, respectively) is more than 0, the LC molecules in the bulk tend to orient along the direction of the electric field. The alignment of the LC molecules in the area of contact between the LC molecules and the alignment layer is not affected by the applied electric field. So the alignment layer in conventional LCDs acts as a passive layer in the switching process. The interaction and thus the reorientation of the LC bulk molecules play an active role in the whole switching process.

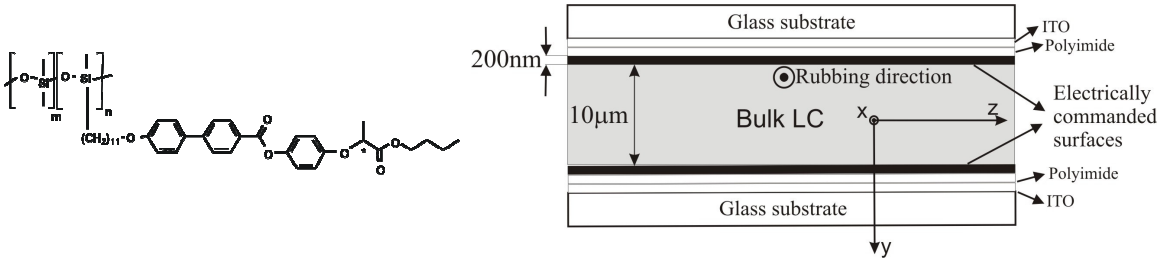

Figure 4-3: (a) Chemical formula of the siloxane-based side-chain LC polymer. (b) The geometry of the cell with electrically commanded surfaces.

The ECS alignment layers are made of a thin film of siloxane-based side-chain ferroelectric liquid crystal polymer (FLCP) deposited onto the inner surfaces of the LC cell (see Figure 4-3). The FLCP film is oriented in a bookshelf geometry with SmC* layers being perpendicular to the confining glass substrates. The electric field applied across the cell does not directly switch the LC bulk molecules, but it reorients the molecules of the FLCP film and subsequently the LC bulk molecules follow them due to elastic forces. In the typical liquid crystal cell configuration this coupling provides an in-plane switching of the optical axis of the planar aligned liquid crystal bulk (Figure 4-4) [19,20].

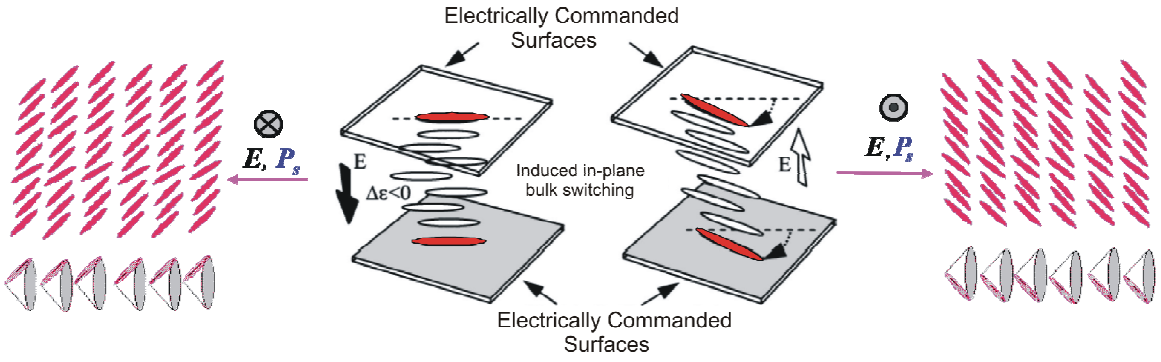

Figure 4-4: Schematic representation of an in-plane switching of FLCP molecules in the ECS layer.

In some previous investigations by means of time-resolved high resolution birefringence measurements it was shown that application of an external voltage to a cell containing

isotropic liquid (hexadecane) and FLCP alignment layers, representing ECS, induces in-plane deviation of the sample optical axis, with its sign depending on the field polarity [20,21]. The angle of the field-induced deviation was observed to be proportional to the applied electric field, which signifies the "V-shaped" switching of the FLCP film [22, 23]. However, the associated apparent switching angle of the mesogenic side chains was found to be much smaller than the tilt angle of the same FLCP material in its bulk SmC* phase and also much lower than the reorientation angle of the optical axis observed in the LCD cell controlled by these layers [21]. There might be several reasons for the observed discrepancy. One of them could be the presence of domain structure in the FLCP layer, which reduces the effective tilt angle of the molecules over the probed sample area. Another reason might be modification of the FLCP structure in contact with hexadecane.
To shed more light on the mechanisms that might be involved in the static as well as in the dynamic behavior of FLCP alignment layers, playing the role of ECS, we performed optical SHG of the same FLCP alignment layers studied previously by high resolution birefringence measurements. In contrast to optical birefringence measurements, which probe quadrupolar ordering of the structure associated with the alignment of the smectic planes, SHG probes polar moments of the molecular angular distribution and hence gives information on the polarization properties of the films [24]. The emphasis of our study was on field-induced modification of the nonlinear optical susceptibility and on switching dynamics of the SHG response. A comparative analysis was made between cells filled with hexadecane and empty cells in transmission geometry. We investigated also the temperature dependence of the SHG signal throughout the phase transition from the SmC* to the SmA* phase.

4.3 Samples

Cells used in our measurements were composed of two equal plates made of a glass substrate on which three different layers were deposited subsequently: a conductive ITO film, serving as an electrode, an unidirectionally rubbed polyimide film, and a 200 nm thick layer of a siloxane FLCP material (see Figure 4-3 (b)). The details of the synthetic route and ferroelectric properties of this FLCP material are reported elsewhere [25]. The value of its bulk spontaneous polarization at room temperature is 160 nC/cm^2. It exhibits the SmC*-SmA* phase transition at 105^{o}C. A cell, with a 10 μm gap, was filled with an isotropic liquid (hexadecane), which is SHG *inactive*. The role of the isotropic liquid was to increase the local field within the FLCP film and to reduce optical reflection at the interfaces, while at the same time assuring that it will not affect the electro-optic response of the FLCP film.

4.4 Results of SHG measurements on ECS samples as alignment layers in LCDs

The SHG investigation on ECS samples was performed in transmission geometry (Figure 4-5). First we performed the SHG measurements on an empty cell and afterwards we filled the cell with hexadecane in order to increase the effect of electric field (see

Figure 4-6). The ITO and FLCP layers are relatively thin thus we expected that the SHG signal would mainly originate from that part of the ECS cell. At normal incidence of the fundamental optical beam the observed SH intensities for all polarization combinations (sp, pp, ps and ss of the fundamental and the SH beam) were very low. The signal significantly increased when the sample was rotated around the x axis (Figure 4-5). The SH response of an empty cell to the triangular external electric field with an amplitude of 100 V and a frequency of 5 mHz for sp and pp polarization combination at an angle of incidence of 45° is shown in Figure 4-6 (a). The average value of the SH intensity in the pp polarization combination is approximately 10 times larger than for the sp combination. For pp polarization combination the response is bipolar with nearly linear dependence on the voltage U, while for sp polarization combination a significant deviation from linear dependence can be observed (see Figure 4-7 (a)). Contrary to pp and sp polarization combinations, the SH responses in the ps and ss polarization combinations were practically zero and did not exhibit any variations related to the external voltage.

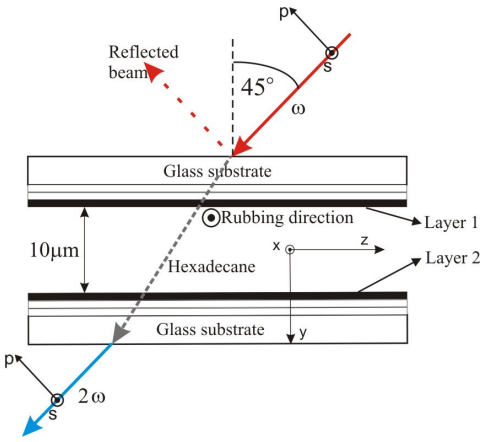

Figure 4-5: The experimental setup of the transmission geometry.

The SH response from the cell filled with hexadecane is shown in Figure 4-6 (b) for sp and pp polarization combinations.

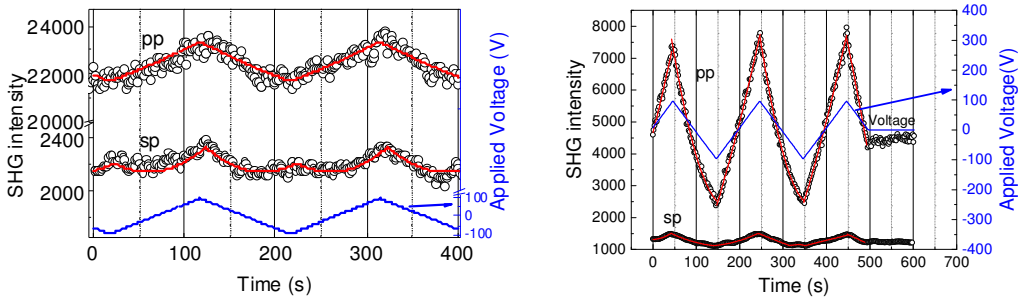

Figure 4-6: The SHG response to the external electric field for the (a) empty ECS cell and (b) the ECS cell filled with hexadecane.

The presence of hexadecane resulted in a decrease of the average SH intensities. For pp polarization combination the SH signal is approximately five times lower compared to an empty cell, but the modulation contrast is significantly increased. On the contrary for sp polarization the modulation contrast is not that significant, but is similar to the one observed in the empty cell.
Similar to the empty cell the relative modification of the SH intensity as a function of applied voltage for the pp polarization is nearly linear, while the sp signal still exhibit almost quadratic coupling (see Figure 4-7 (b)).

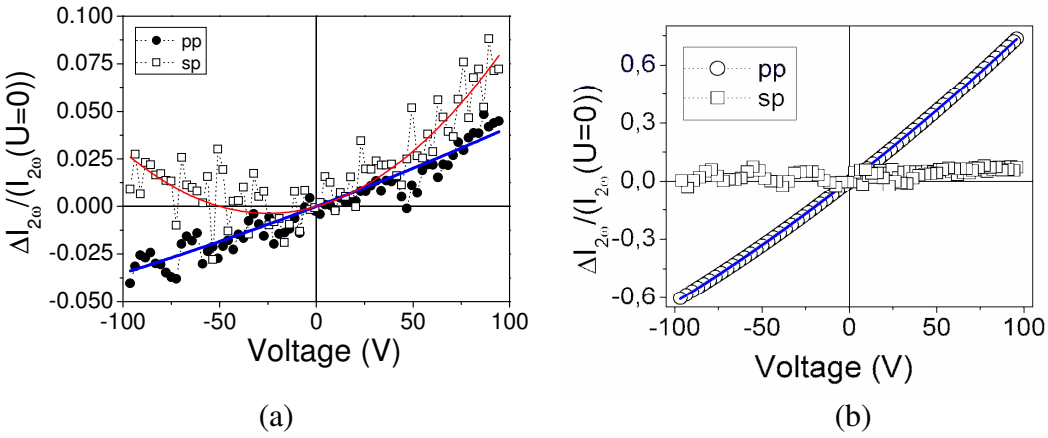

Figure 4-7: Relative SHG intensity as a function of applied electric field of the ECS cell for (a) an empty ECS cell and (b) a cell filled with hexadecane.

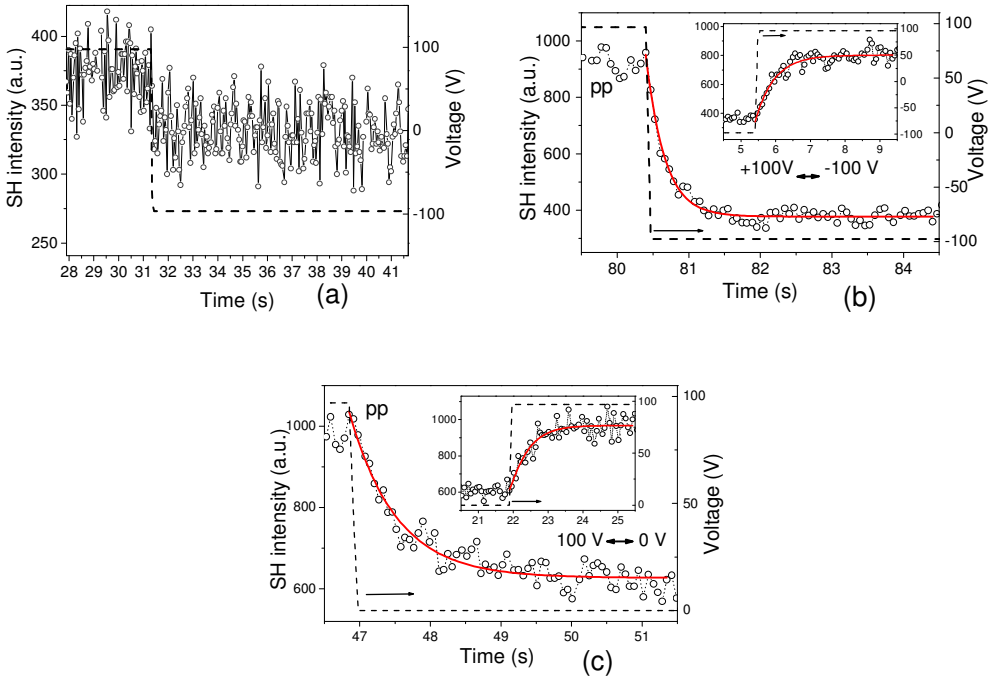

Figure 4-8: Temporal response of the SHG signal to the square waveform voltage from +100 V to -100 V for (a) the empty cell and (b) the cell filled with isotropic liquid hexadecane (the inset shows the switching from -100 V to +100 V). (c) Temporal response of the cell filled with hexadecane to voltage varying between 0 and 100 V. The dashed line refers to the voltage shown in the right vertical axis.

In the next series of measurements we probed the dynamic response of the SHG signal to the voltage alternation from U = +100 V to U = -100 V and vice versa.The best temporal resolution, at which we could still resolve the signal from the noise, was 50 ms. The response obtained for pp polarization combination for an empty cell is shown in Figure 4-8 (a). A steplike modification of $I_{2\omega}$ can be observed, therefore a corresponding switching time τ cannot be determined.

From these measurements we can only conclude that in the empty cell the value of τ is below 50 ms. The dynamic response of the cell filled with hexadecane measured for pp polarization combination is shown in Figure 4-8 (b). Closer inspection of the switching time give considerably longer switching times than in the empty cell, so that the value of the switching time can easily be resolved at temporal resolution of 50 ms. The temporal response was fitted by exponential function for both switching characteristics in Figure 4-8 (b). For the falling voltage step the SH response was fitted by $(1+A\exp(-t/\tau))^2$ and by $(1+A[1-\exp(-t/\tau)])^2$ for the rising voltage step. The obtained response time has a value of $\tau = 0.50 \pm 0.12$ s.

To resolve a free structural relaxation of the field-induced changes, we measured also the dynamic response after switching-on and switching-off of the external voltage 100 V (see Figure 4-8 (c)). In this case the switching-off process is slower compared to switching-on process. The corresponding values of both switching times are $\tau_{off} = 1.31 \pm 0.11$ s and $\tau_{on} = 0.46 \pm 0.15$ s.

At room temperature the FLCP layer is in the SmC* liquid crystal phase. By increasing the temperature of the sample the FLCP layers experience a phase transition from the SmC* to the SmA* liquid crystal phase at 105°C. In order to probe this phase transition we heated the ECS cell to approximately 120°C. First we measured the temperature dependence of the SHG signal in the absence of an external electric field. The results obtained for the pp polarization combination are shown in Figure 4-9. For temperatures below 100°C the SHG signal weakly decreases with the increasing temperature. At around 105°C the SHG intensity suddenly drops down indicating the SmC*-SmA* liquid crystal phase transition of the FLCP layer. The phase transition occurs almost at the same temperature as in the bulk FLCP even though the probing FLCP layer is only 200 nm thick.

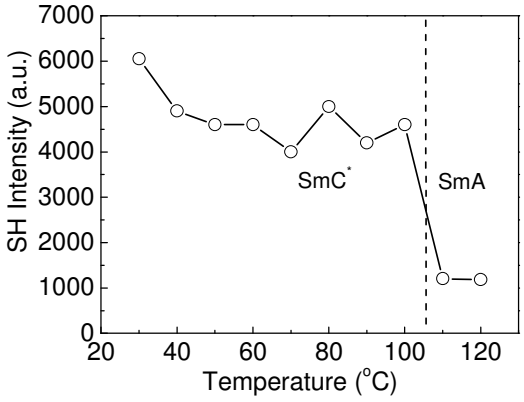

Figure 4-9: The SHG intensity for pp polarization combination measured in the absence of an external electric field as a function of temperature. The phase transition from SmC*-SmA is clearly observed between 100°C and 110°C.

The next step of investigation of the ECS cells was to probe their field-induced response at different temperatures. We have measured the electric field-induced SHG signal in steps of 10°C and observed that the response of the FLCP layers dramatically changes.

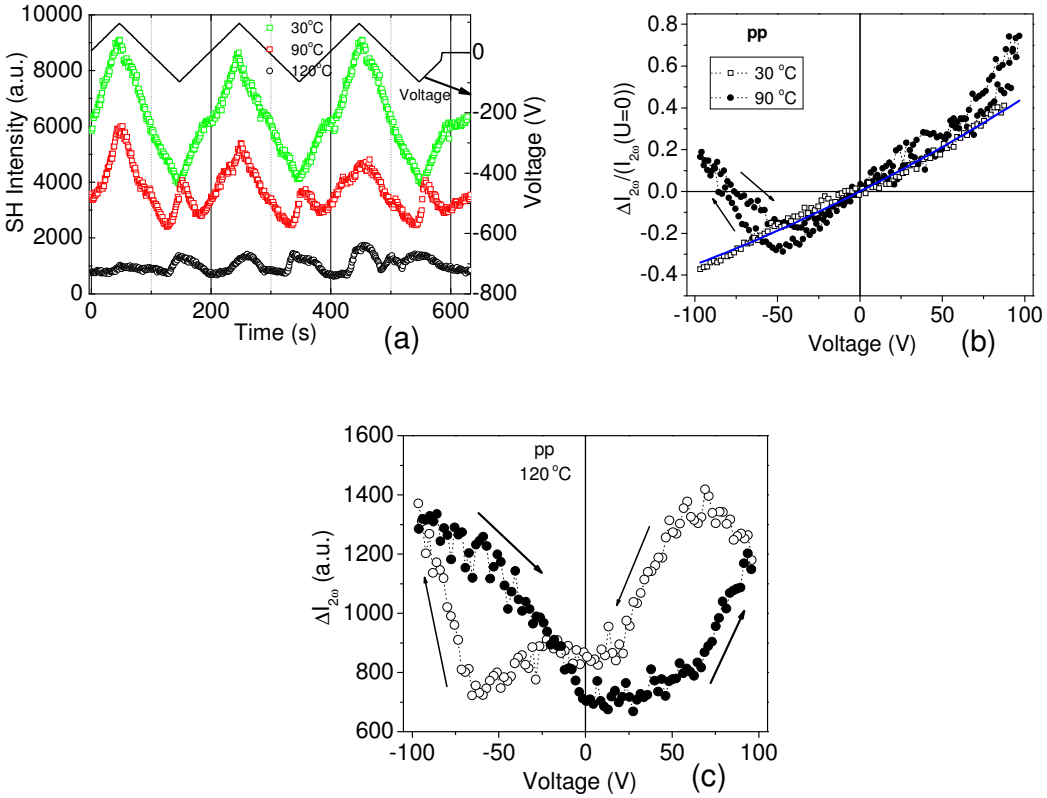

Figure 4-10: (a) SHG response to V-shaped electric field at different temperatures. (b) Relative SHG response as a function of applied voltage at 30 ºC and 90 ºC for the cell filled with hexadecane. (c) Variation of the SH intensity for pp polarization combination as a function of applied voltage in the SmA* phase at 120 ºC. Filled and empty symbols represent data obtained during increasing and decreasing voltage, respectively.

The SHG modulations show strong temperature dependence of the field-induced SHG of the FLCP layers. The nearly linear bipolar response observed at room temperature changes to the quadratic unipolar response (Figure 4-10 (a)). In the SmA phase only the quadratic modulation of the SHG response is retained. We also observed some hysteresis effects at higher temperatures, i.e. the response during the increase of the voltage was considerably different compared to the one during the decrease of the voltage (Figure 4-10 (b) and Figure 4-10 (c)).

4.5 Discussion

First we consider the origin of the SHG signal from ECS cells. By neglecting the SH contribution from the polyimide layer, there are at least three different terms of the second order nonlinear susceptibility

$$\chi^{(2)} = \chi_{ITO} + \chi_{FLCP} + \chi_{\text{int}}, \tag{43}$$

where χ_{ITO} represents the second order nonlinear susceptibility of the ITO film, χ_{FLCP} the second order nonlinear susceptibility of the FLCP layer, and χ_{int} stands for the interaction between the FLCP and the ITO, which takes place via polarization induced surface charging of the ITO layer [26]. In general the ITO electrodes are a considerably strong source of SHG and thus their contribution cannot be neglected in the thin film geometry. The magnitudes of the first two SHG contributions are of the same order, which was verified by SHG measurements performed in a similar cell, but without the FLCP layer. When a voltage was applied across the ITO cell only quadratic unipolar response was observed. Such behavior can be attributed to the change of the refractive index (Kerr effect) of hexadecane, which results in a phase shift between the SHG fields generated by the two layers. In the empty cell without hexadecane such effect was not observed (green curve in Figure 4-11).

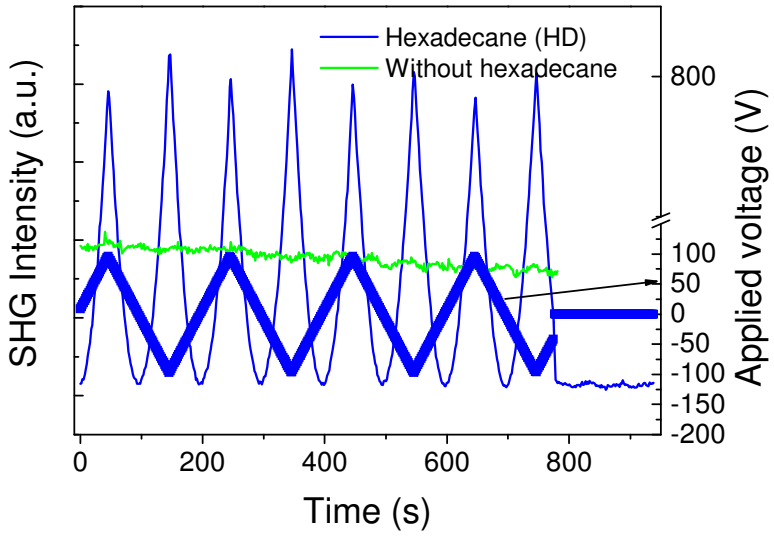

Figure 4-11: The SHG response to the external electric field of an empty ITO cell and when filled with hexadecane (HD).

Now we will explain the signal reduction of the net SHG radiation when filling the cell with hexadecane and from where the quadratic response for the cell filled with hexadecane and without FLCP is coming from. Since we are dealing with the ECS cell which has two identical surfaces with ITO electrodes and FLCP layer (Figure 4-5), both of them contribute to the SHG signal. But due to the surface reflections the fundamental optical fields in those two layers are different. Besides the last statement only the field-sensitive parts of the nonlinear susceptibility have, due to the same direction of the electric field, the same orientation in both layers. On the contrary, the field independent contributions are expected to be of the opposite sign because of their complementary orientation. Expression of the SHG intensity can be formed as follows:

$$I_{2\omega}(1+2) \propto \left(I_{2\omega,0} + \left(\chi^{(2)}_{FLCP+ITO}(1) I_{\omega}(1) + \chi^{(2)}_{FLCP+ITO}(2) I_{\omega}(2) \cdot \exp\left[i\Delta kL / \cos\gamma \right] \right)^2 \right). \quad (44)$$

Here $I_{2\omega,0}$ is the background contribution to the SHG intensity, $I_\omega(1)$ and $I_\omega(2)$ represent the intensities of the fundamental beam in both layers, $\Delta k = k_{2\omega} - 2k_\omega$ is the wave vector mismatch between the SHG and the fundamental beams respectively, and γ is the propagation angle of the beams in hexadecane [27]. The wave vector mismatch is nonzero in a cell with hexadecane and zero in air (empty cell). The term $I_{2\omega,0}$ was added to expression (44) because SHG measurements in thin ferroelectric LC cell imply that such a term appears as a consequence of the frozen SmC* structure in contact with the substrates [28,29]. From expression (44) it follows that in the cell filled with hexadecane the interference of SH contributions originating from the front (layer 1) and back (layer 2) walls of the cell is very important and for $\Delta kL \sim [(2N+1)\pi]$ results in strong reduction of the net SHG signal.

A quantitative determination of a χ_{FLCP} from our experimental results would be very speculative, but we can determine its field-induced changes, which was the main goal of our investigation. The net spontaneous polarization should be zero at U = 0 V but as it can be seen from Figure 4-6 this is not the case. The SHG contribution from the FLCP film is nonzero even in the absence of the field. Such a property can be attributed to the intrinsic static nonlinear susceptibility related to the structural defects, i.e. the domain-like structures of the sample [30]. The additional contribution to the SHG response is the field induced part which is proportional to the structural polarity and therefore in the first approximation increases linearly with the applied electric field. According to the above statements the nonlinear susceptibility of the FLCP layer follows as

$$\chi_{FLCP} = \chi_0 + a \cdot E, \tag{45}$$

where χ_0 represents the static and $a \cdot E$ the field-induced SHG terms. The coefficient a is the coupling constant of the FLCP layer and an electric field which can be either positive or negative.

The SHG intensity of the interfacial region in equation (44) can be written in first approximation as

$$I_{2\omega}(E) \propto I_{2\omega,0} + b\left(\chi_0 + a \cdot E\right)^2, \tag{46}$$

where the coefficient b represents the ratio between the coherent and incoherent parts. If the field-dependent term is small compared to the static one the variation of the SHG intensity with the applied field is linear. For large fields a deviation from the linear dependence becomes evident and a relative modification of the SHG intensity shown in Figure 4-7 can be given as

$$\frac{\Delta I_{2\omega}}{I_{2\omega}(E=0)} = \frac{I_{2\omega}(E) - I_{2\omega}(E=0)}{I_{2\omega}(E=0)} \propto \frac{2ab\chi_0 E + ba^2E^2}{I_{2\omega,0} + b\chi_0^2}, \tag{47}$$

which is in good agreement with the observed behavior in Figure 4-6. The ITO layers and the defects in the FLCP film hence act as a reference SHG signal that coherently adds to the field-induced signal. They play a role analogous to the reference SHG plates in a conventional phase sensitive SHG setup [31].

The so-called electrically induced SHG (EFISH) is nowadays used for characterization of electrical properties of thin films and interfaces. This effect is very well characterized by the equation (45) and is analogous to the interface field approximation which assumes linear dependence of the DC-field induced nonlinear polarization on the interface field strength [32]. In [33] Aktsipetrov et.al. demonstrated for Si (001) – SiO_2 interfaces, that nonlinear interference of the field dependent and field independent contributions can provide internal homodyne amplification of the EFISH contribution of the SHG response. In the temperature region of the SmC* phase a similar effects takes place also in our samples. The magnitude of the SHG from the unswitchable domains can be estimated from the temperature dependence of $I_{2\omega}$(U = 0V) shown in Figure 4-9, in which it is evident that the spontaneous polarization of the domains slowly decreases with increasing temperature and more or less vanishes at 105°C (SmC*-SmA* transition). The small SHG signal still present in the SmA* phase can be attributed to $I_{2\omega,0}$ and ITO electrodes. On the other hand, the unipolar response of the SHG signal above the phase transition indicates that the $I_{2\omega,0}$ is dominant. The variable SHG signal in the SmA* phase can be explained by the electroclinic effect [28,34]. The electroclinic effect is a response of chiral molecules in the SmA* phase on external electric field resulting in an average molecular tilt.

Now we can make some comments on the observed differences between the SHG signal from the empty cell and the cell filled with hexadecane. The main benefit from hexadecane is an increased magnitude of electric field inside the FLCP film at selected applied voltage. The static dielectric constant ε of the hexadecane is 2, which is approximatelly three times smaller with respect to FLCP dielectric constant i.e. 7 [35]. For applied voltages up to 100 V the corresponding electric field ranges from 0 to 1.4 V/μm and from 0 to 2.8 V/μm for a 10 μm thick cell filled with hexadecane. The threshold fields in the few micrometer thick ECS cell typically ranges from 1 to 10 V/μm [36] so in our 200 nm thick FLCP layers we are still below the threshold. The presence of the hexadecane in the ECS cell affects the optical properties of the cell. It reduces surface reflections at the boundaries, but at the same time it causes undesired destructive interference between the SH contributions from layer 1 and 2. The latter also explains why an average SHG intensity is smaller compared to an empty cell (Figure 4-6). Closer look at the field-induced variations of the SHG signal for both types of cells (empty one and the one filled with hexadecane) reveals that the four times larger relative variations cannot be explained by a factor 2 increase in the applied electric field. This suggests that hexadecane also modifies the SmC* structure of the FLCP layer. It is probable that it reduces the pinning of the domains and makes them more switchable. It is also very likely that the domains which were completely immobilized during the preparation procedure of the FLCP layer become active. The coefficient a in equation (45) is increased, which means that the ratio between χ_0 and the field induced part of susceptibility in equation (45) increases.

The Figure 4-8 shows the relaxation processes of the empty cell and the cell filled with hexadecane. All dependences were fitted with an exponential function. In the empty cell the field-induced variation of the SHG signal represents only 2.5 % of the average value. This suggests that only a relatively minor part of the FLCP film, very probably the topmost surface layer in contact with air, responds to the electric field. The field-induced reorientation is small and hence the switching time is short. When adding hexadecane, the domain structure of the material is relaxed and also regions below the surface start to

respond. The reorientation of the side chains is larger, and consequently, it takes more time to accomplish the complete switching process. The exact temporal dependence of the response is expected to be quite complex, however the quality of our experimental data does not allow us to resolve the details. The empirically assumed exponential dependence of the χ_{FLCP} is in very good agreement with the exponentially observed dependence. The measurements of switching-off the external electric field showed that the response times are only three times longer compared to response times when turning the same electric field back on. This observation shows that the internal forces, which cause a decay of the spontaneous polarization after poling, are of the same order of magnitude as the field-induced ones.
One can notice the large discrepancy between the switching times measured with SHG and the ones measured with field-induced birefringence, with later τ being around 20 ms (switching from +70 V to -70 V) [21]. The SHG results give $\tau \sim 500$ ms for switching from 100 V to -100 V. This large difference can be explained by the fact that the birefringence method probes only in-plane alignment of the FLCP layer with the preferential orientation in the xz plane. We assume that this aligned layer was affected by the direct buffing process. It is known from near-edge X-ray absorption fine structure (NEXAFS) measurements that buffing induces molecular alignment only in a 10 nm thick topmost surface layer of the polymer [37]. The topmost layer of the FLCP hence responds to the field in the millisecond time scale, which was also concluded from our SHG measurements with an empty cell. If the results on the birefringence modulation are recalculated by taking into account only the thickness of the aligned topmost layer of the FLCP, then the corresponding molecular in-plane reorientation angle becomes 23°, which is similar to the reorientation angle observed in the LC cells made by the same ECS layers. The presence of the alignment only in the topmost surface layer also suggests that the indirect alignment of the FLCP due to the presence of the polyimide substrate is much less efficient. The SHG measurements are, on the contrary, sensitive to the polarity of the FLCP structure, i.e. to its macroscopic dipole moment along the *y*-axis. This dipole moment is also nonzero in the regions, which have no preferential orientation of the smectic layers in the *xz* plane. These unaligned domains seem to contribute the main part of the SHG signal in the case of the cells filled with hexadecane, but they do not contribute to the birefringence. The dynamic response of the domain regions of the sample is strongly affected by the structure of domain walls, which results in a much slower response to the external field than the response of the top-most layer. One should also not forget, that a large part of the FLCP structure, especially the regions anchored to the substrate, does not respond to the field at all, so in principle they have an infinitely long response time.

4.6 Conclusions

Our results demonstrate that the SHG technique is an efficient tool to study the structural and switching properties of thin films of the FLCP molecules in the SmC* phase. For applied electric fields up to 2.8 V/μm the SHG measurements reveal V-shaped switching of the FLCP molecules. In the unperturbed FLCP the field-induced modifications of the structural polarity are very low compared to the polarization of the unswitchable parts of the FLCP. The switchable SHG response originates mainly from the topmost surface

layer of the FLCP, while the main part of the film is in a strongly pinned domain configuration.
When the FLCP is in contact with hexadecane the domain-like structure seems to relax and thus the field-induced SHG modifications are intensified resulting in a slower relaxation process. The polar order responsible for the SHG seems to possess slower dynamics with respect to the in-plane quadrupolar order simply because a much larger part of the FLCP contributes to the SHG signal than to the birefringence method.
The SHG results indicate that the structure of FLCP interface is layered. These layers are as follows: (a) the topmost surface layer which is very well aligned due to buffing and responds to the applied voltage with a response time on the order of ten milliseconds; (b) the intermediate volume layer in the form of a domain-like structure that responds with a response time of 1 s; (c) a frozen layer anchored to the substrate that might be a major contributor to the SHG signal but does not respond to the electric field. The topmost layer is from the concept of proper operation of the ECS cell the most important, but at the same time it is coupled to the underneath domain-like structure, which influences its response. However the knowledge of the complete structure and its response to the external voltage is prerequisite in order to tailor the properties of the ECS alignment layer for applications in the LCD industry.

Chapter 5

Atomic Force Microscopy

In previous chapters we presented investigations of thin surface layers by using second harmonic generation technique. The emphasis was on LC materials. With the following chapter we start the discussion about the construction of thin film architectures of biomolecules, i.e. DNA oligonucleotides and fatty acids. To probe the topography, ordering and structure of these films we used a combination of two experimental techniques, namely atomic force microscopy (AFM) and sum-frequency generation (SFG). We start with a short description of the AFM technique.

The AFM technique belongs to the family of so-called scanning probe microscopy – SPM, where a sharp probe is scanned across a surface in order to probe the interaction with the investigated sample. The result of such investigation is the topography of the surface. There are several primary modes of AFM operation [38]:

(a) **Tapping mode AFM**: it operates by scanning a tip attached to the end of an oscillating cantilever across the sample surface. The oscillation frequency of the cantilever is adjusted slightly below its resonance frequency with amplitude ranging typically from 20 – 200 nm. The tip very lightly taps on the sample surface contacting the surface only at the bottom of the swing. The feedback loop maintains constant oscillation amplitude by maintaining a constant RMS of the oscillation signal acquired by the split photodiode detector. The topography of the investigated surface is acquired by the vertical position of the scanner at each data point in order to maintain constant »setpoint« amplitude.

(b) **Contact mode AFM**: it operates by scanning a tip attached to the end of a cantilever across the sample surface while monitoring the change in cantilever deflection with a split photodiode detector. The tip contacts the surface through an adsorbed fluid layer on the sample surface. A constant deflection between the cantilever and the sample is maintained by a feedback loop. The constant cantilever deflection enables the force between the tip and the sample to be constant. The force can be calculated from Hooke´s law $F = -kx$, where F is the force, k is the spring constant and x is the cantilever deflection. The distance the scanner moves vertically at each data point on the sample is stored by the computer to form the topographic image of the sample surface.

(c) **Non-contact mode AFM:** it operates with an oscillating cantilever at a frequency slightly above its resonance frequency and with an amplitude < 10 nm. The tip does not contact the sample surface, but oscillates above the adsorbed fluid layer

on the surface during scanning. The feedback loop maintains a constant oscillation amplitude or frequency by vertically moving the scanner at each data point until »setpoint« amplitude or frequency is reached. The topography of the surface is obtained by the distance the scanner moves vertically at each data point.

The typical AFM setup is shown on Figure 5-1. The mode of operation is basically determined by the type of detection electronics which are the following: for the Tapping mode AFM the RMS of the amplitude signal is measured, for the contact mode the A-B/A+B of the deflection signal is measured, and in non-contact mode AFM the oscillation amplitude or frequency is measured.

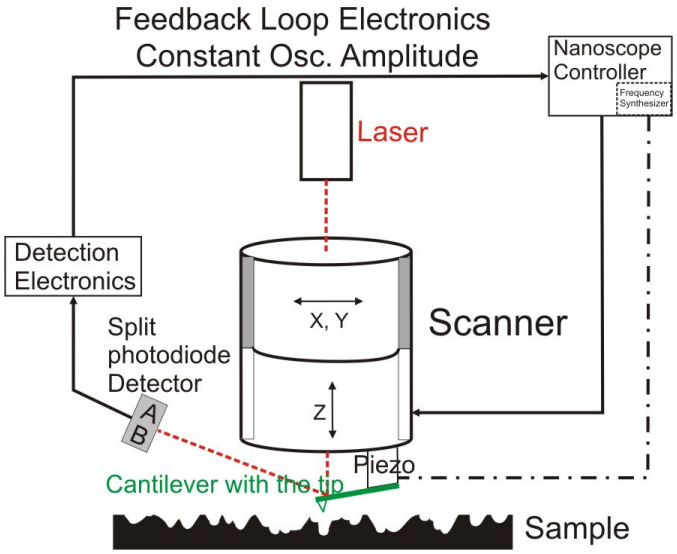

Figure 5-1: The schematic representation of typical AFM setup.

Main part of the AFM images of surface structures shown in the next chapter were taken by standard AFM in tapping mode using Nanoscope Dimension DI3100 with Nanoscope IV controller (Veeco Instruments). Beside this we also used Multimode AFM operating in contact mode in order to resolve the relative orientation of the aggregates with respect to the substrate.

Chapter 6

Surface structures of Guanosine 5´-monophosphate (Part 1)

6.1 Introduction

In the first part regarding surface structures of guanosine 5´-monophosphate (GMP) the main focus will be on preparation of samples and their topography observed under the AFM.
Construction of surface architectures via a controllable self-assembly process is a challenging goal, which can lead to a broad range of applications in nanoscale molecular electronic devices. Promising candidates for such exploration are guanosine molecules and its derivatives. Guanosine 5`- monophosphate is the RNA nucleotide composed of nucleic base guanine, sugar ribose, and the phosphate group (Figure 6-1).

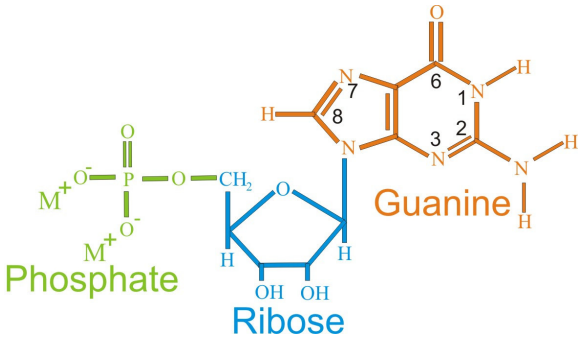

Figure 6-1: Structure of Guanosine 5´-monophosphate.

It is unique among all nucleotides because it self-assembles into highly ordered structures in aqueous environment. However, this self-assembly property is not unique only for the GMP but for all guanine analogs. This is due to the fact that the nucleic base guanine possesses the self-complementary hydrogen bonding edges and aromatic surfaces which tend to self-associate. Guanine has two hydrogen bond acceptors (N7 and O6) on its Hoogsteen face and two hydrogen bond donors (N1 amide and N2 amino) on its Watson-Crick face. Due to their polarized aromatic surfaces the guanosine derivatives can self-assemble in solutions into several highly ordered structures such as dimers, tetramers, ribbons, or macrocycles [39,40]. Guanine is also distinctive among all the DNA bases for its low ionization potential, due to which it plays a key role in electrical conductivity of DNA-based materials [41-45]. The self-organization of guanine rich systems can also be found in many settings in nature. Some spiders have cells known as guanocytes that are

filled with crystalline plates of guanine. When these spiders feel endangered, they change the color instantly by retracting the guanocytes from their surface [39,46]. Also some deep-sea fish contain layered guanine crystals that focus light to the photoreceptors [39,47].

We will basically focus here on the self-assembly process of GMP into tetramers. The starting GMP material is usually in the form of an alkali metal salt. When dissolved in water the formation of hydrogen-bonded tetramers occurs. Due to the hydrophobic interactions between two tetramers of GMPs in solution the vertical stacking of the quartets takes place. The quartets are rotated with respect to each other to form a four-stranded helix. The stacking between two adjacent tetramers is further stabilized by the counterions (K^+, NH_4^+, Na^+, Rb^+, Li^+, and Cs^+) binding to the carbonyl groups in the cavity. These rod-like cylinders are more commonly known as G-wires. The whole self-assembly process is schematically shown in Figure 6-2. The basis of Guanosine self-assembly was proposed by Gellert et al. in 1962 [45] when they reported on hydrogen-bonded tetramers formed of 3´-GMP and 5´-GMP. They proposed that the tetramers were formed of guanine molecules held together by 8 hydrogen bonds and that the stacking of two such tetramers resulted in a helix-like formation with a spacing of 3.25 Å which was later confirmed by diffraction data for guanosine analogues and polyguanylic acid.

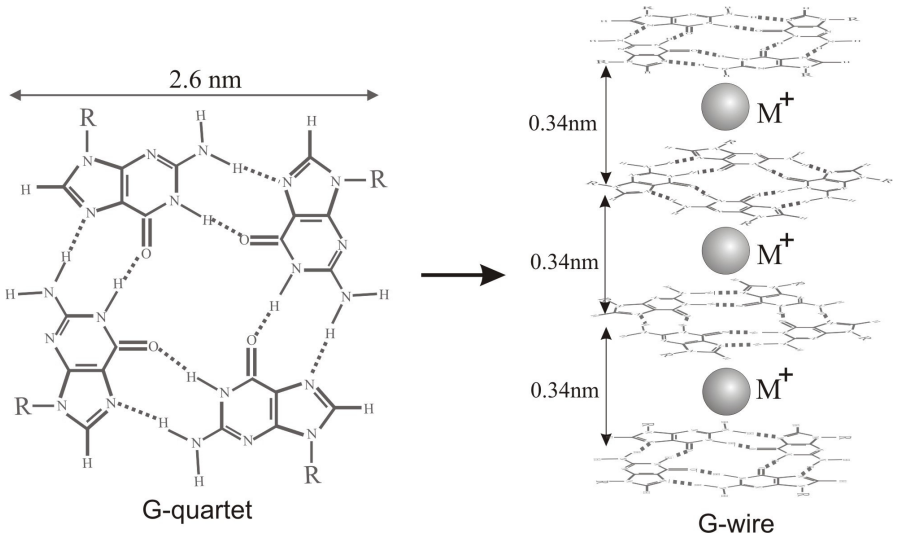

Figure 6-2: The self-assembly process of GMP molecules from G-quartet to G-wire (the grey spheres in the G-wire figure represent either potassium, ammonium or sodium counterions).

The length of G-wires depends on several external factors such as: type of the counter ions present in solution, pH, temperature, and concentration of the solution. The last two have also quite a large impact on the self-organization of GMP superstructures. With increasing concentration the GMPs start to develop liquid crystal phases [48,49]: from isotropic at 10 wt%, to cholesteric between 15-30 wt% and to hexagonal above 30 wt%.

The combined dynamic light scattering (DLS), ^{31}P NMR, and small angle X-ray scattering techniques were used to study Guanosine analogues and to determine the influence of added salt in solution [50], the influence of temperature [51], and the rate of concentration [52] on the formation of GMP aggregates. The presence of additional counterions in the solution increases the stacking process of GMP tetramers, when at

certain concentration of added salt the saturation is reached leading to almost 70% of all molecules aggregated. Strong dependence on molarity of added salt also indicates on a polyelectrolyte nature of the GMP stacks [50]. The comparative study of deoxy- and guanosine 5´-monophosphate (dGMP and GMP) in the pretransitional region of the Isotropic-Cholesteric phase transition [51] revealed that dGMP molecules start to assemble at lower concentrations and form considerably longer aggregates compared to GMP. On the other hand both molecules show similar melting curves with three characteristic regions: a low temperature interaction-controlled region, a narrow region of intense aggregate dissociation, and a high temperature region of dissociated species (GMP monomers). In 2005 Wong et al. [52] reported on detailed investigation of disodium GMP at pH 8. They studied the influence of concentration and temperature on the length and type of aggregates present in the solution. There are two types of aggregates present in the solution i.e. stacked 5´-GMP monomers and stacked G-quartets. Both types have the shape of rod-like cylinders.

In the following part of the introduction the focus will be on the behavior of Guanine analogs near the solid substrates. In aqueous environment the GMP self-organization occurs above a certain critical concentration which ranges from 5-30 wt% at room temperature. The length of the wires in solution can be up to some tens of nanometers and depends on the selected G-derivative, on solution parameters such as concentration, temperature, pH, and especially on the type and concentration of the cations [53-55].

The self-assembly of GMPs on solid substrates is, in contrast to the one in aqueous environment, not very well known. Recent investigations of surface structures of guanosine analogs and G-rich oligonucleotides have shown that these molecules also self-organize on solid substrates giving configurations with a high degree of order. Otero et al. [56] reported on self-assembly of guanine evaporated on Au (111) substrate under ultrahigh-vacuum condition. By using scanning tunneling microscope they observed a 2D lattice of G-quartets laying flat on the surface. A 2D array of flat-laying G-quartets was observed also at the interface of graphite and an 8-oxo G-derivative [57]. On the contrary, guanine derivatives attached to golden nanoparticles were not laying flat but were tilted with respect to the surface [58]. G-derivatives were placed on Si/SiO_2 substrates in order to probe the conductive properties of G-adsorbates. It was demonstrated that films of modified deoxyguanosines can be used as hybrid molecular electronic devices, such as transistors and photodetectors [59-61].

The self-assembly of G-rich oligonucleotides on mica was investigated by Marsh et al. They observed long G4-wires of $d(G_4T_2G_4)$ on freshly cleaved mica by AFM [62,63]. The height of these G4-wires very well corresponded to the diameter of the G-quartet measured in solution i.e. 2.4 nm [64]. Lipophilic deoxyguanosine derivatives on mica assembled either into layered thin films of G-quartets or nanoribbons, formed by hydrogen-bonded G-arrays. A surface-induced type of growth was proposed, in which the K^+ ions from the substrate served as aggregation centers for the guanines [65,66]. Vesenka et al. also revealed a strong correlation between the K^+ sites on mica and the G-4 wire growth. They also showed that at appropriate adsorption conditions the wires are auto-oriented in three preferential directions with respect to the underlying mica lattice. Using different experimental techniques, poly(G) strands were shown to form very long and stiff G-wires that exhibit also an extremely high stability and resistance to heat treatment [67]. These properties make G4-wires very attractive candidates for

applications in nanoelectronics, which are in many aspects superior to other DNA-based structures.
Our aim was to investigate if besides all these relatively large and complex guanine-based molecules also the simplest derivative, namely guanosine 5´-monphosphate, has the property to self-assemble on solid substrates. To elucidate this problem we used an AFM and SFG techniques to determine surface structures of GMP adsorbates deposited on freshly cleaved mica, Au (111), SiO_x, etc. by several types of depositions from aqueous solutions. A broad range of solution concentrations was probed and due to the fact that self-assembly in solutions strongly depends on type of cations, we also performed a comparative study between the surface structures formed from solutions of sodium, potassium and ammonium GMP salts.

6.2 Experimental

We started our investigation of GMP molecules at surfaces by using the so called drop-deposition and dip-coating deposition of GMPs on freshly cleaved mica substrate ($K_2O{\cdot}Al_2O_3{\cdot}SiO_2$; SPI Supplies, V-1 grade). The comparative study of di-sodium, di-ammonium and di-potassium salt GMP was made. The di-sodium GMP was purchased from Sigma-Aldrich Chemie (Steinheim, Germany; 100% purity, HPLC grade) and the other two were prepared by titration of the GMP free acid (98-100% purity; MP Biomedicals, USA) with NH_4OH and KOH, respectively, followed by subsequent lyophilisation. The selected material was dissolved in pure distilled water (Aqua ad iniectabilia) at several mass concentrations of the solution. The first depositions were made at high concentrations; the one that are reported in literature as critical concentrations for self-organization of the GMP molecules in aqueous environment i.e. c > 10 wt%. In the drop deposition procedure the same amount of the selected solution (V = 10 µl) was always deposited on the substrate and afterwards the sample was left in air at room temperature for 6-9 h. In the next series of measurements we diluted the initial solution at 20 wt% concentration to various concentration ranges between 0.004 - 0.5 wt%. At this point we used the so called dip-coating deposition in order to obtain more homogeneous and less densely packed surface structures.

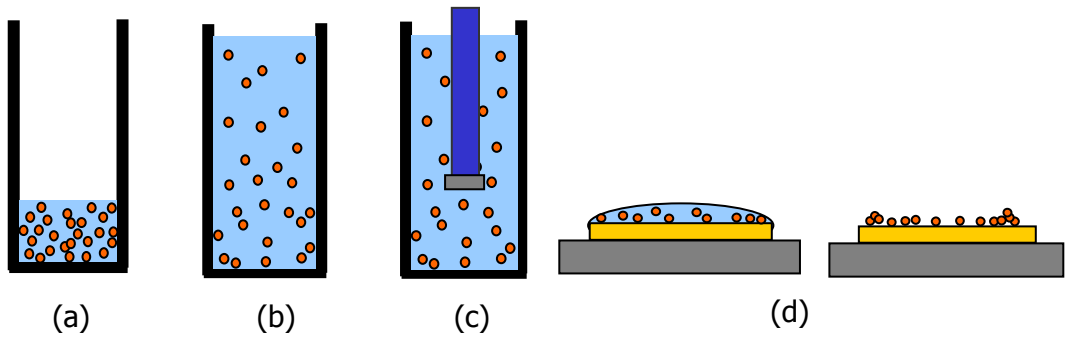

Figure 6-3: The dip-coating deposition: (a) preparation of 20 wt% solution, (b) dilution to required concentration, (c) dipping the sample for 3 minutes, (d) drying in air for 6 h.

The mica substrates used for the preparation of GMP surface structures were freshly cleaved and mounted onto a steel holder. The surface structures of GMP films obtained by dip-coating deposition (see Figure 6-3) were prepared by dipping the substrate into the required solution for three minutes. The volume of solution used for dipping was always the same; i.e. V=500 µl. After deposition the samples were dried in air at room temperature for 6-9 hours. After preparation procedure the developed surface topography was investigated by AFM technique. Most of the images were taken in the tapping and some of them in contact mode. The AFM images were always taken in the center of the substrate in order to avoid the material density gradient towards the edge, which is triggered by the drying process. The GMP surface structures nevertheless always showed some variation due to the concentration gradient effects, which could not be avoided.

6.3 Results

In the first series of experiments we prepared the GMP surface structures at concentrations in the range where the self-assembly of GMP in water solutions occurs. Initially we deposited the GMP on the surface by drop deposition. The AFM results for potassium and sodium GMP on mica substrate are shown in Figure 6-4 and Figure 6-5. It can be clearly seen that there is no direct correlation between the concentration and the developed surface structure. The roughness of all three concentrations spans in the range of 100 nm for both potassium and sodium GMP salts.

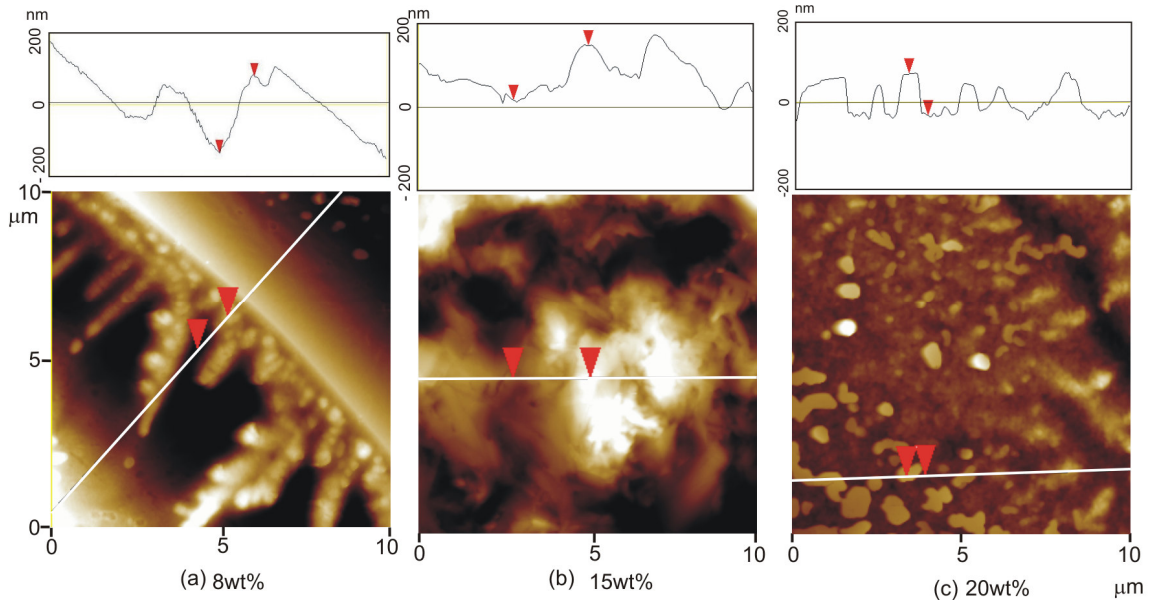

Figure 6-4: The AFM images of K_2 –GMP molecules deposited on mica substrate by drop deposition of solution with different concentrations.

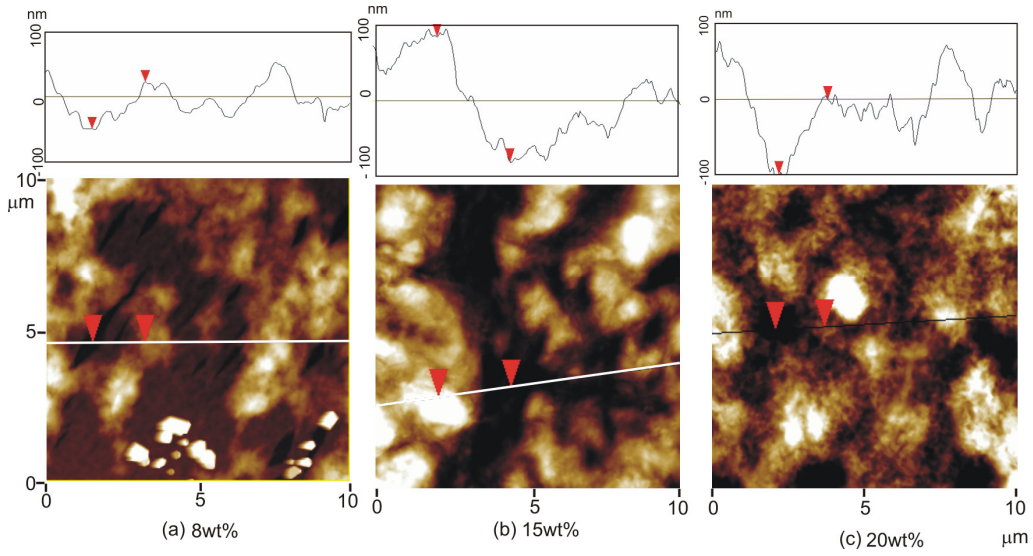

Figure 6-5: The AFM images of Na_2 –GMP molecules deposited on mica substrate by drop deposition.

Since we had no success in controlled preparation of surface structures of GMP by drop deposition technique we started to use the so called dip-coating deposition. We also introduced the dilution stage which means that the initially prepared GMP solution was first diluted to the required concentration and afterwards deposited on the substrate by dip coating. For GMP solution concentrations of $c \leq 0.01$ wt% only small isolated patches of deposited material with diameter of approximately 100 nm were observed on the substrate (Figure 6-7). The statistical analysis showed that the height of these islands was in the range of 2-5 nm. At the same time larger flat patches with a lateral dimension around 400 nm also appear at some places on the substrate (see Figure 6-7 (a)).

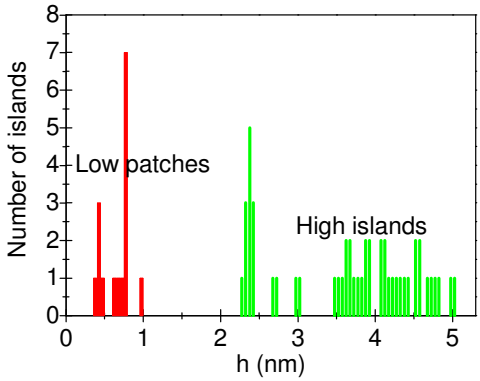

Figure 6-6: The statistical analysis of the islands and patches of GMP material on mica substrate deposited at $c \leq 0.01$ wt%.

Their height was around 1 nm. Both types of structures were observed in all low concentrated GMP solutions, but their internal structure is not yet resolved. The low flat patches might be monolayers of tilted GMP molecules [58] and the islands could be clusters of segregated salt [68].

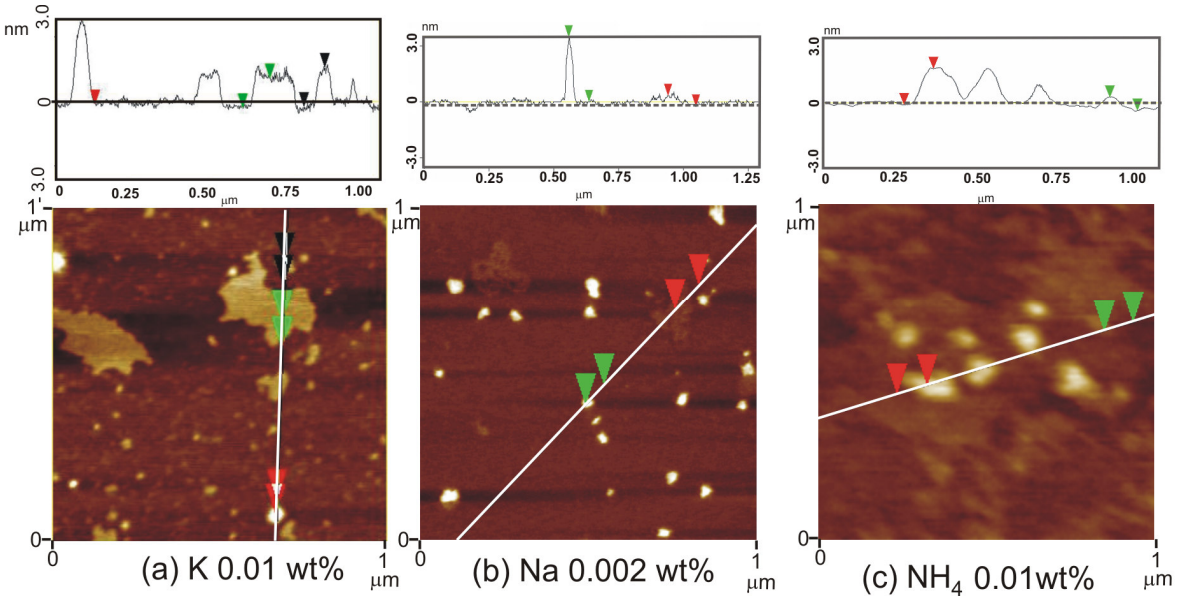

Figure 6-7: Tapping mode AFM images of different types of GMP salts on mica prepared from solution with the concentration c ≤ 0.01wt%.

When the deposition was made from solutions with 0.01 wt% ≤ c ≤ 0.02 wt% aggregates in the form of single wires and interconnected networks of wires appeared on the mica substrate. In Figure 6-8 to Figure 6-10 are shown the tapping mode AFM images for all three types of GMP salts.

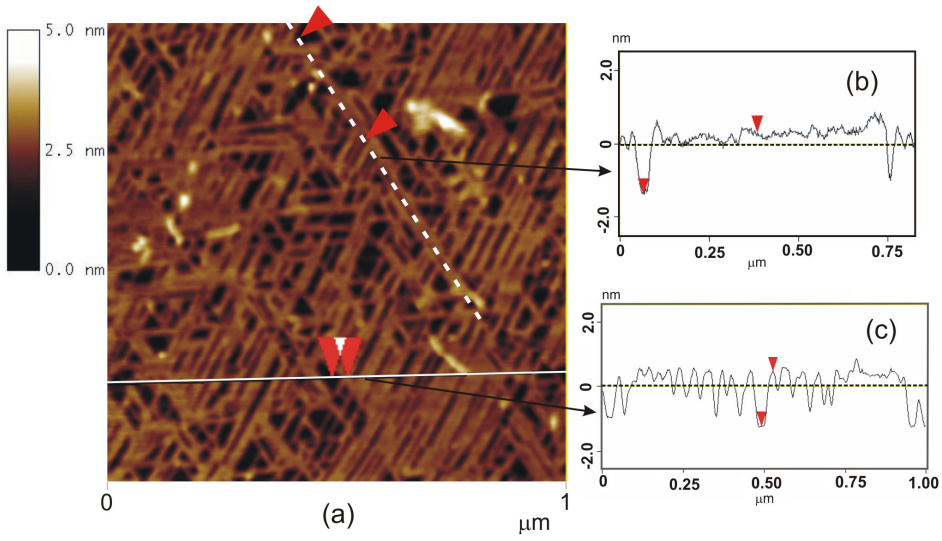

Figure 6-8: (a) Tapping mode AFM image of 1µm x 1µm large area of potassium GMP deposited on mica from solution of c = 0.02 wt%. (b) Cross section in direction along a single wire (dashed line in (a)) and (c) cross section in direction perpendicular to the G-wires.

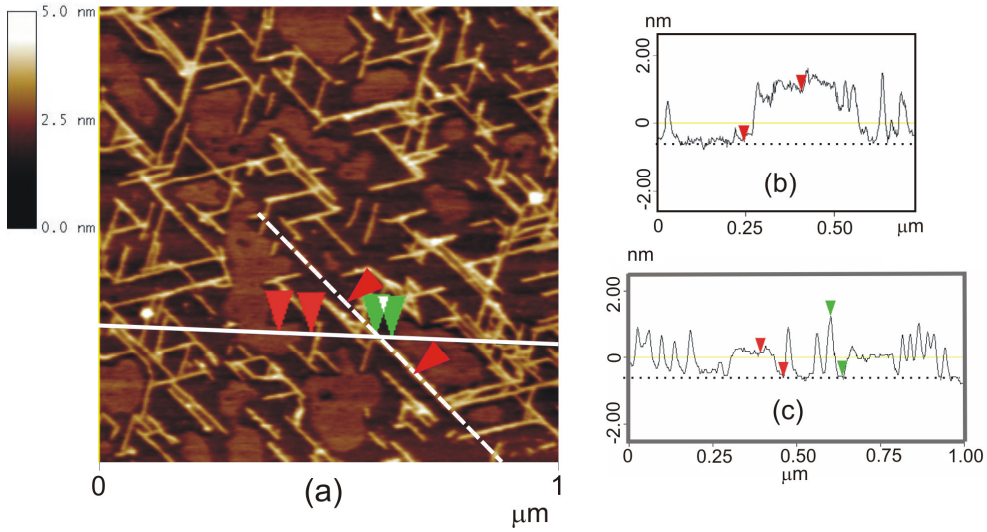

Figure 6-9: (a) Tapping mode AFM image 1µm x 1µm large area of ammonium GMP deposited on mica from solution of c = 0.01 wt%. (b) Cross section in direction along a single wire (dashed line in (a)) and (c) cross section in direction perpendicular to the G-wires.

Two cross-sections, one in direction perpendicular to the wire and the other along a single wire, are shown for each GMP salt. Several interesting features of the wires can be easily resolved. At first, they are even 1 micrometer long (observed in some cases) and very straight. They typically originate from small aggregated islands and grow out in six preferential directions with respect to the substrate. The preferential growth directions are separated for about 60°. The height of a single wire above the substrate surface ranges between 1.5 and 2.2 nm, which is evident from cross-sections, while the interconnection points extend slightly higher (above 5 nm).

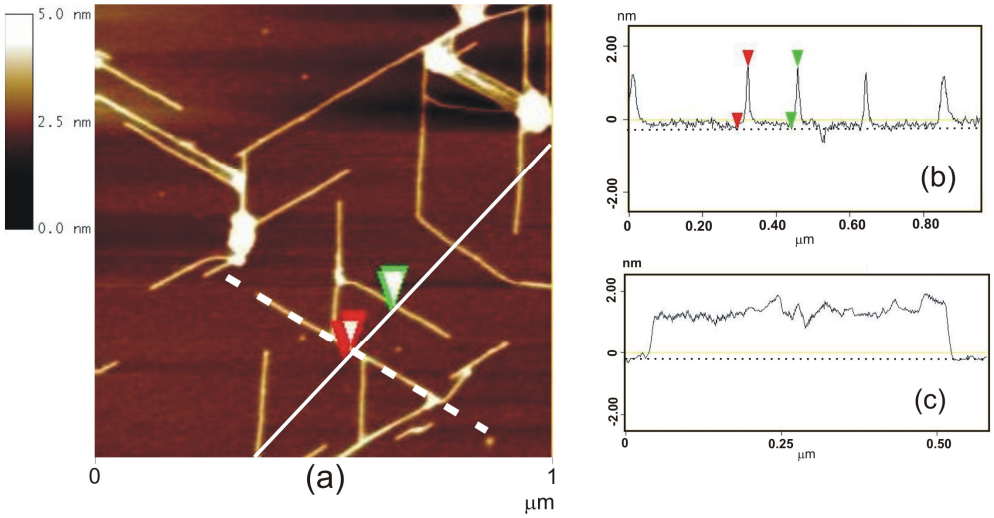

Figure 6-10: (a) Tapping mode AFM image of 1µm x 1µm large area of sodium GMP deposited on mica from solution of c = 0.01 wt%. (b) Cross section in direction along a single wire (dashed line in (a)) and (c) cross section in direction perpendicular to the G-wires.

In contrast to the sodium GMP structures shown in Figure 6-10 (a), the ammonium GMP surface structures (Figure 6-9 (a)) also show again low patches of the adsorbed material which were also observed in low-concentration samples. The differences in the density of the wires between all three types of GMPs are within the structural variations due to material density gradient effects shown in Figure 6-11. This gradient is a consequence of the drying process that governs the deposition of the material towards the edge of the drying drop.

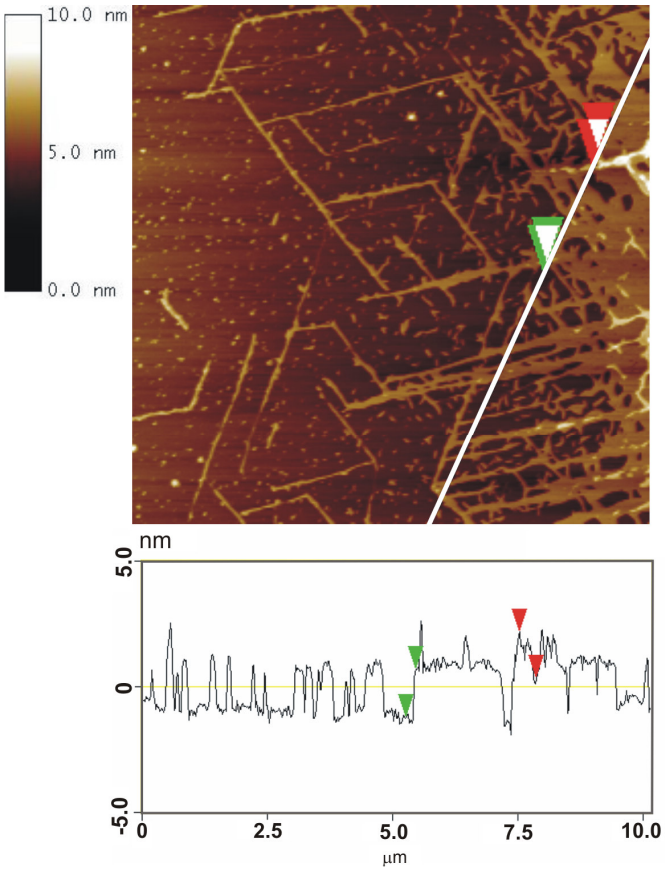

Figure 6-11: The tapping mode AFM image of 10 µm x 10 µm large area of sodium GMP deposited on mica substrate from aqueous solution at 0.02 wt% concentration.

In order to obtain some quantitative information about the aggregates, we made a statistical analysis of their height and orientation. The height of each selected object was determined on two to three different spots. The histogram with height distribution is shown in Figure 6-12. The histogram suggests the formation of surface structures that span across a large number of height values but at the same time indicate that majority of G-wires have h ~ 2 nm. The height of these wires is in good agreement with the diameter of G- wires formed on surfaces by other G-derivatives and G-rich oligonucleotides [63,67]. Why the height of these G-wires does not completely match with the diameter of G-quartet in aqueous environment (d ~ 2.4 nm) is not completely resolved yet. We have several possible explanations for such discrepancy: (a) the interaction with the substrate can lead to different conformation of the G-quartets on the surface; (b) it is not necessarily that the G-wires outside the solution are formed from G4 units but could be

also either stacked monomeric or dimeric units, especially the structures with height < 1.7 nm; (c) the pressure of the AFM tip can lead to lower apparent height of the G-wire [67].

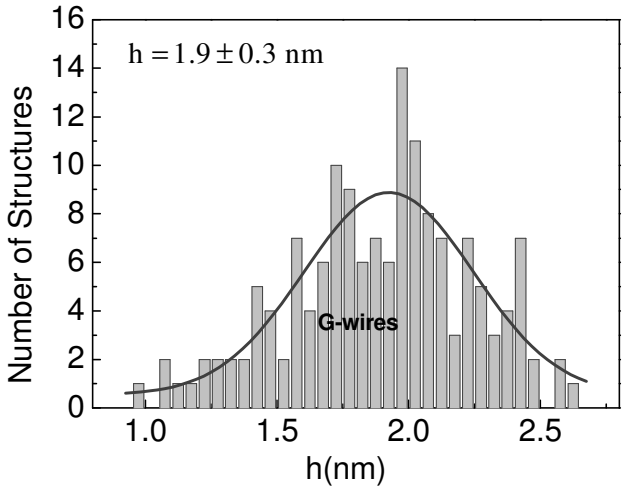

Figure 6-12: Height distribution of G-structures deposited from 0.01 wt% ammonium GMP solution. Solid line represents a fit to the Gaussian distribution taking into account data in the range of h > 1 nm.

As evident from Figure 6-8 and Figure 6-11 the G-wires on mica substrate posses certain orientational order to develop surface structures with six-fold rotational symmetry. To deduce this orientational ordering of the G-wires orientation, several objects were analyzed. The distribution of orientations is shown in Figure 6-13.
The reference point from which the G-wire orientation was determined was selected by the direction of the slow scan AFM axis, which means that the 0° corresponds to the horizontal direction. One can be clearly see three pronounced peaks separated by 60°, which indicate on six-fold rotational symmetry of developed surface structures.

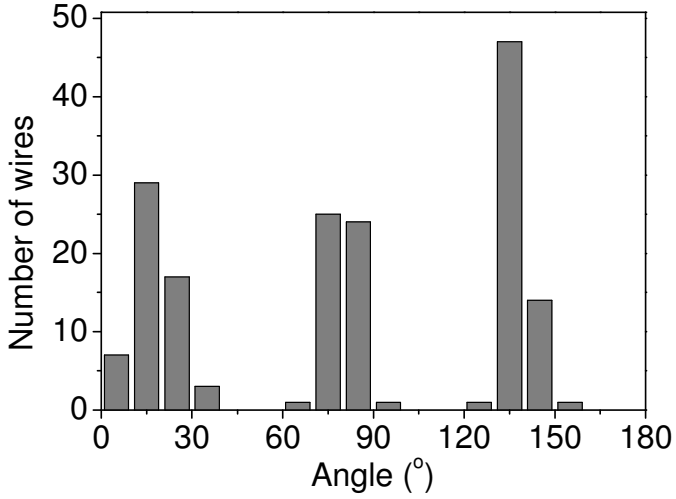

Figure 6-13: The orientational distribution of the G-wires reveals three preferential directions for G-wire orientations separated by 60°.

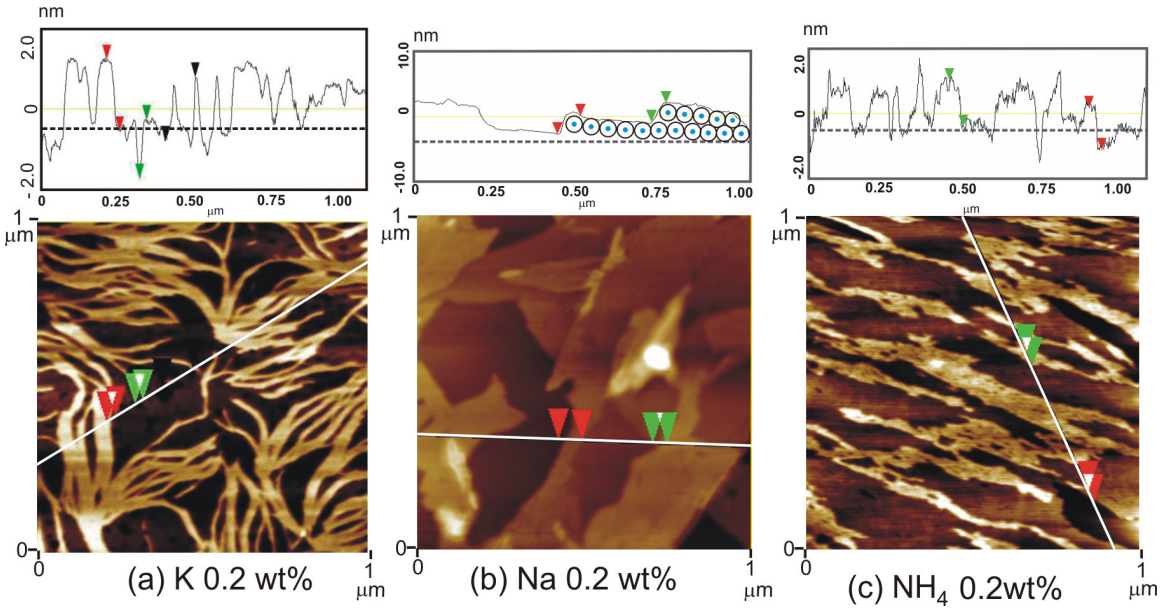

Figure 6-14: Tapping mode AFM images of different types of GMP salts on mica prepared from solution with the concentration of c = 0.2wt%. The possible conformation of G-wires in a single layer is shown in the cross section of (b). The blue circles represent cations between two adjacent G-quartets.

We also made the deposition at 10-times higher concentrations i.e. 0.2 wt%. It can be clearly seen from Figure 6-14 for all three types of GMPs, that the G-wires start to develop multi-layered structures. The height of these layers ranges from 2.2 – 2.8 nm, which is in very good agreement with the diameter of G-quartet measured in water solutions. We also proposed one of the possible models for development of such layers. It is shown in the cross-section of Figure 6-14 (b). The layers are attributed to crystal planes of a hexagonal lattice of the G-wires, which lie with their long axes parallel to the surface of the substrate. It is often that within such layered structures the holes, which extend down to the substrate, are developed. In general such layers show no preferential orientation similar to the one observed for intermediate concentrations. For solution concentrations c > 0.2 wt% the surface structures of the adsorbates becomes more and more irregular and congested, similar to the one observed in Figure 6-4 and Figure 6-5.

6.4 Discussion

Among all structures developed on the mica substrate the most interesting ones are G-wires formed in the intermediate concentration range (0.01 wt% ≤ c ≤ 0.02 wt%). As already mentioned in the introduction of this chapter, the G-wires are supposed to be very promising candidates for conductive elements in molecular electronic systems. Compared to the wires formed from other G-derivatives and G-rich oligonucleotides, the ones made from simple molecules such as GMP have two distinctive advantages. At first, being the stacks of planar G-quartets they can be completely homogeneous from the structural point of view. The density of defects created along the wire depends solely on the growth process. This is contrary to the wires formed from short oligonuclotides e.g. d($G_4T_2G_4$)

[63], which are sequential chains of G-quadruplex units interrupted by thymine (T) molecules. These act as intrinsic defects for charge transfer mechanism. The other advantage of the GMP wires is that there seem to be no restrictions for their length. Sometimes we observed wires that were more than couple of μm long (see Figure 6-11). Therefore by controlling the adsorption procedure, especially certain external factors such as humidity, temperature and substrate features, we expect that the length of G-wires could be tailored to the desired requirements. This would be in contrast to the self-folded poly(G) wires, which length is determined by the size of poly(G) chain and hence can be manipulated only via chemical synthesis procedure [67].
Control over orientational alignment of the wires is very important in characterization of their physical properties, such as electrical conductivity, rigidity, etc. There are several papers [65,69] that reported on auto-orientation of the guanosine structures on mica and suggested that this orientation is related to a specific coordination of intrinsic potassium cations in the top mica layer, which act as binding centers for the guanosine molecules. The muscovite mica is composed of sheets of phyllosilicates, in which octahedrally coordinated aluminium atoms are sandwiched between two identical layers of linked (Si, Al)O_4 tetrahedra [70]. Between two of these tetrahedrally coordinated sheets lies an interlayer of potassium cations. During the cleavage process single or multiple sheets are removed, so that the basal plane is composed of quasi-hexagonal array of oxygen ions. The cross-section through sheets of muscovite mica and the cross-section made in the plane with K atoms of muscovite mica are shown in Figure 6-15 (a). This quasi-hexagonal surface structure is schematically shown in Figure 6-15 (b) and has a lattice dimensions of a = 0.52 nm and b = 0.9 nm [70]. The K^+ ions, which are released within this array, can now serve as centers for adsorption of the G-quartets.

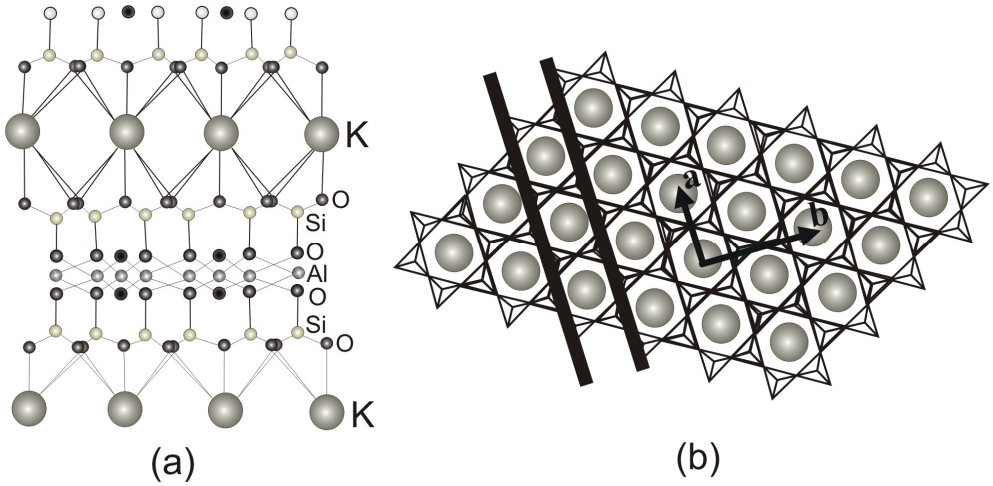

Figure 6-15: (a) Side view and (b) top view of the cross-section made in the plane with K atoms.

Although three preferential growth directions of G-wires were observed before, the wires formed from GMP show far more profound substrate-induced directional growth. The growth direction of the wires formed of GMP with respect to the underlying mica substrate was determined by AFM operating in contact mode with molecular resolution.

The AFM images, which clearly indicate the orientation of G-wires on mica substrate, are shown in Figure 6-16.

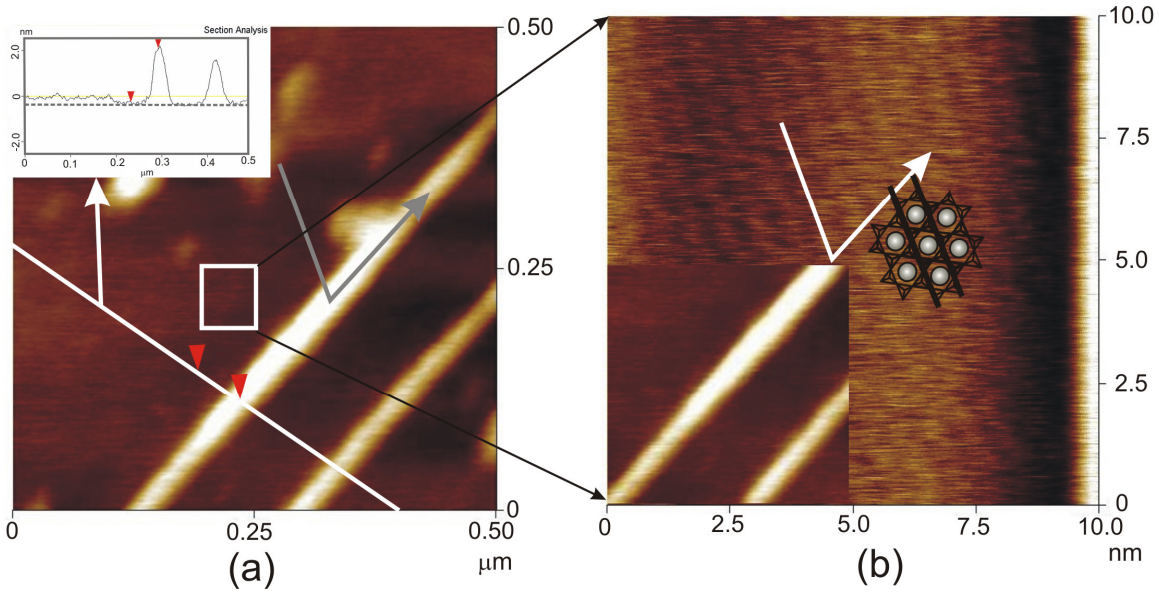

Figure 6-16: (a) Contact mode AFM image of G-wires on the mica substrate deposited from 0.01 wt% solution. The inset in (a) shows the cross-section over two wires as shown with white line. (b) Zoom-in of the nearby surface region of the mica substrate. The grey and white arrows in (a) and (b) respectively indicate the G-wire growth direction.

We initially took an AFM image of two wire-like aggregates found within the surface region of 0.5 µm x 0.5 µm (Figure 6-16 (a)). Then we zoomed-in with the AFM tip to the nearby region of the substrate (indicated by white square in Figure 6-16 (a)) and acquired its image on the scale of 10 nm x 10 nm (Figure 6-16 (b)). The dark parallel stripes in Figure 6-16 (b) correspond to the lattice planes of basal mica surface. These planes are separated by b/2 = 0.45 nm (Figure 6-15 (b)), which is in very good agreement with the separation obtained with contact mode AFM. The arrows (grey and white) in Figure 6-16 are pointing out the preferential direction of the G-wire growth. According to our images this direction is rotated for around 60° with respect to the stripes. This means that the wires are oriented in the direction of 60° with respect to the lattice vector a marked in Figure 6-15 (b). This is also the direction along the nearest neighbors in the quasi-hexagonal mica lattice.

The hexagonal arrangement of the aggregation stimulating K^+ sites causes that the wires grow out from the seed islands in correlation with the symmetry of the substrate. Therefore, a six-fold symmetry of the preferential growth directions is anticipated. Measurements in solution show that the inter-stacking distance of the G-quartets is 0.34 nm [45]. These G-quartets stack on top of each other forming a helical structure in a way that two adjacent G-quartets are rotated for approximately 30° with respect to each other. Since the period of such G-wire equals 3 x 0.34 nm = 1.02 nm the orientation along the nearest neighbor direction, i.e. along a direction, where twice the mica lattice distance 2a corresponds to 1.04 nm, is the most probable.

According to our observations, the formation of G-wires on mica is almost independent of the type of cations (potassium, sodium or ammonium) present in the solution used for

dip coating procedure. The only major distinction was that it was more likely that in the case of NH_4 – GMP the wires would be truly formed in the intermediate concentration i.e. 0.01 wt% ≤ c ≤ 0.02 wt%. On the other hand, nevertheless, the wires were formed from all three GMP salts and the developed G-wires possessed similar properties. The height distribution of the wires and their typical length did not depend on the type of the salt, which is contrary to the G-quartet stacking in solution that is strongly cation-dependent [53-55]. This finding suggests that self-assembly of the material in its solution phase does not play any important role for its surface aggregation. During slow drying of the droplet on the substrate, most of the GMP adsorption very probably takes place before the effective solution concentration reaches the critical value needed for formation of the aggregates in water solution. Therefore we believe that aggregates typical for the solution phase cannot even form. On the other hand, due to the dominant surface aggregation by potassium cations from the mica substrate, the formation of aggregates does not depend on the cations present in the initial material.

The layer-like structures observed for the concentrations around 0.2 wt% have the properties of crystal-like structures. X-ray scattering experiments on mica substrates revealed that GMP helices crystallize in a hexagonal arrangement with a_G = 2.86 nm being the separation between the helix long axes [71]. The crystal planes of parallel G-wires (growing in the crystallographic c_G direction) adsorbed to the substrate are consequently expected to have the height of $h_G = a_G \sin(60°)$, which gives the value of 2.48 nm. The model of G-wire crystal-like structure is schematically shown in Figure 6-17.

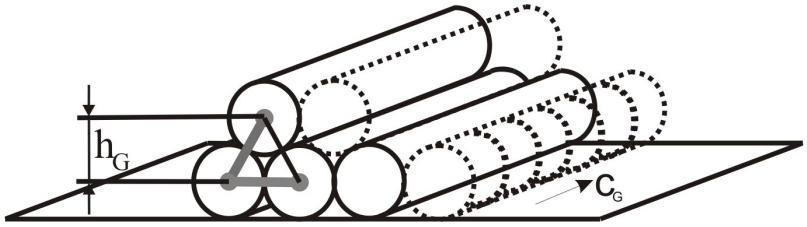

Figure 6-17: Terrace-like structure of G-wire with the height of approximately 2.5 nm. This value very well corresponds to the crystalline structure of G-quartets with wire axis lying parallel to the mica plane.

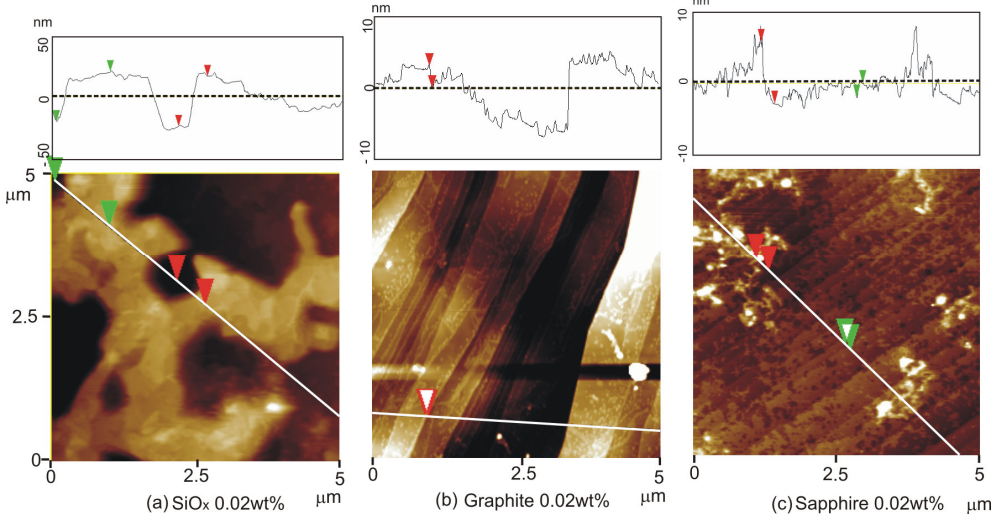

Figure 6-18: The AFM images of GMP material deposited on different substrates: (a) SiO_x; (b) Graphite and (c) Sapphire.

This is in very good agreement with the height of the single layer in our AFM images i.e. h ~ 2.5 nm (see Figure 6-14). Once the first crystal layer is developed at the substrate it serves as the template for the formation of subsequent layers.
As a test if the formation of G-wires also occurs on other substrates, we used the same preparation procedure and GMP concentrations also for SiO_x, graphite, and sapphire substrates. We observed only irregular patches of GMP molecules on the substrate. This indicates that the G-wire formation is substrate specific and is induced by the atomic arrangement of the mica basal plane.

6.5 Conclusions

Our results showed that GMP molecules can be promising candidates for future explorations of possible uses in nanoscale electronic devices, especially the formation of long G-wires with uniform height. We showed that Guanosine 5´-monophosphate exhibit an ability to grow in the form of very long, straight and well oriented nanowires on the mica substrate. These wires are on average 1.9 nm high and can be up to several micrometers long. They are aligned along the six directions of the nearest neighbours of the quasi-hexagonal basal mica plane.
The AFM results show that the formation of the G-wires depends on the concentration of the initial solution and is observed in the range from 0.005 wt% to 0.1 wt%. For smaller concentrations there is simply not enough material to initiate the wire growth, while at larger concentrations the layered structures appear on the mica substrate. The process of surface self-assembly is practically independent of the type of cations present in solution for intermediate concentrations, which is contrary to the self-assembly of GMP molecules for all three types of GMP derivatives in water solutions. We attribute this discrepancy to the specific surface structure of the mica substrate where the K^+ ions stimulate the aggregation of GMP molecules.

In the next chapter we will analyze the results of comparative study of different GMP films prepared on various solid substrates by using AFM and SFG spectroscopy. We have studied C-H molecular vibrations obtained from SFG spectra and analyzed the surface topography in order to obtain the information about the structure and ordering of thin films on the solid substrate.

Chapter 7

Experiment of Sum-frequency generation spectroscopy

The SFG spectroscopy (also known as frequency domain SFG) is an optical technique where the temporary long (spectrally narrow) VIS pulse overlap in space and time with the temporary short (spectrally broad ~200 cm^{-1}) IR pulse. With such SFG setup one can scan over certain spectral region of the sample and thus investigate the vibrations of certain molecules or molecular groups.

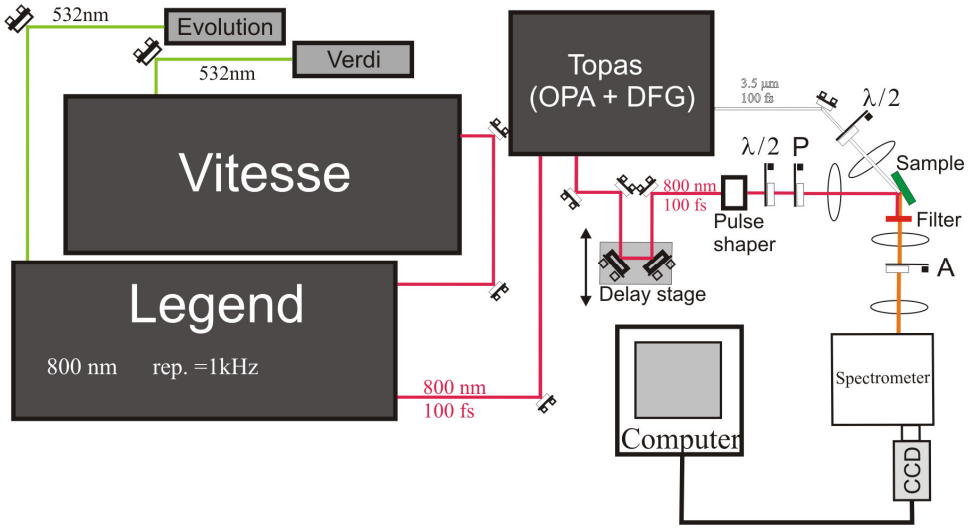

Figure 7-1: Experimental setup for Sum-frequency generation spectroscopy installed at the AMOLF Institute in Amsterdam. The symbols on the figure represent the following optical components **P**: Polarizer, **λ/2**: half-waveplate and **A**: Analyzer

Figure 7-1 schematically shows the experimental setup for frequency domain SFG. In order to perform such SFG spectroscopy we used the lasers pulses generated in the Vitesse-Legend (Coherent, St. Clara, CA, USA) and Topas (Light Conversion, Vilnius, Lithuania) 1 kHz laser system.

7.1 Vitesse-Legend-Topas laser system

Vitesse is a laser oscillator and plays the same role as Mira laser in the Mira-RegA 250 kHz laser system described in subsection 3.1. The pulses from Vitesse are directed into the Coherent Legend which is a titanium sapphire laser amplifier pumped by Nd:YLF (Coherent Evolution) 1 kHz Q-switched laser operating at fundamental wavelength of 532 nm with an average power of 25 W. The laser source from the Legend has a

wavelength of 800 nm and a repetition rate of 1 kHz, which gives energy per pulse and pulse duration of 2.5 mJ and 100 fs, respectively. Only part of the energy is used to pump the Topas (OPA + DFG) in order to generate the IR pulses with the wavelength tunable between 1.1-10 μm (9000 -1000 cm^{-1}). Approximately 0.5 mJ of the fundamental 800 nm laser source is sent through two commercially available etalons (pulse shaper) in order to obtain laser pulses of approximately 5 cm^{-1} spectral width (pulse duration a couple of ps) which is then used as a VIS part of the IR - VIS SFG experiment. The energy of such pulses was approximately 6 μJ. Both beams, IR and VIS, were focused on the sample at incident angles of 53° and 56°, respectively. The beam spot size for both ranged between 150 – 200 μm.

In the frequency domain SFG experiment an imaging monochromator (Acton SP-300i with motorized turret for a set of three gratings) with an intensified Charge Couple device (CCD) camera (Princeton Instruments) was used as a detector. The CCD camera was operating in gated regime with the 60 ns gate width. The CCD camera was also cooled down to -25 ºC to get rid of the thermal noise as much as possible.

Chapter 8

Surface structures of Guanosine 5´-monophosphate (Part2)

8.1 Introduction

As discussed in the Chapter 6, Guanosine 5'-monophosphate develops a wide range of surface structures on the muscovite mica substrate, from islands of aggregated material to wire- or even layered-like surfaces. The formation process very much depends on the mass concentration of the solution from which the GMP molecules are deposited on the surface of the substrate. In this chapter we will describe comparative analysis of surface and bulk morphologies of GMP molecules with different types of cations deposited on two types of substrates (mica and gold). For such analysis the AFM and SFG spectroscopy were used. We expected that by using the combination of AFM and SFG spectroscopy we would be able to obtain more information on surface and bulk morphology of developed GMP films.

8.1.1 Sample preparation

The thin films of guanosine molecules were prepared by using two different types of salts: a) disodium GMP purchased from Sigma-Aldrich Chemie (Steinheim, Germany; 100 % purity, HPLC grade) and b) diammonium GMP which was prepared by titration of the GMP free acid (98-100 % purity; MP Biomedicals USA) with NH_4OH followed by subsequent lyophilisation. The material was dissolved in pure distilled water (Aqua ad iniectabilia) at mass concentration of 20 wt%. This initial solution was then diluted to selected concentrations ranging from 0.02 wt% to 2 wt%. No buffers or other ionic agents were added in order to avoid the introduction of additional assembly-promoting cations to the solution.
The GMP molecules were deposited from solution on freshly cleaved mica substrate (K_2O Al_2O_3 SiO_2; SPI supplies V-1 grade) and a flame annealed Au(111) substrate. This flame annealing process is necessary in order to avoid contamination of Au substrates. The deposition on mica substrates was made by dip coating for 3 minutes [72] and subsequent drying in air for 6-9 h. For the GMP samples on gold surface the drop deposition technique in 15 µl of GMP solution was used. The samples prepared on gold substrates were then also kept drying at room temperature for 6-9 h. Afterwards the topography of developed surface structures was observed by AFM operating in tapping mode. Information about the AFM was given in chapter 5. We paid attention that the AFM images were always taken in the central part of the samples, in which also the SFG spectra were recorded. This is important because the adsorbed GMP structures always show some variations in topography due to the concentration gradient created during the

drying process. After the observations of topography under the AFM the SFG spectra were recorded by tuning the IR pulses to the resonance region of the C-H vibrational band, i.e. 2800 – 3100 cm^{-1}.

8.2 Results

8.2.1 SFG

The SFG spectra recorded on GMP structures on mica and gold substrates show two distinct peaks, one at around 2900 cm^{-1} and other at around 2950 cm^{-1}. According to the literature these two peaks can be attributed to the CH_2 symmetric and asymmetric stretch, respectively [73,74]. The CH_2 group is situated at the tail of the sugar ribose (see also Figure 6-1). Similar spectral peaks were also recorded for the GMP on the gold substrate. In the beginning the SFG response of the bare substrates (flame annealed gold and freshly cleaved mica) was recorded. These are dominated by the non-resonant background giving the power spectrum of the incident IR beam. Afterwards GMP molecules from solutions at different mass concentrations were deposited.

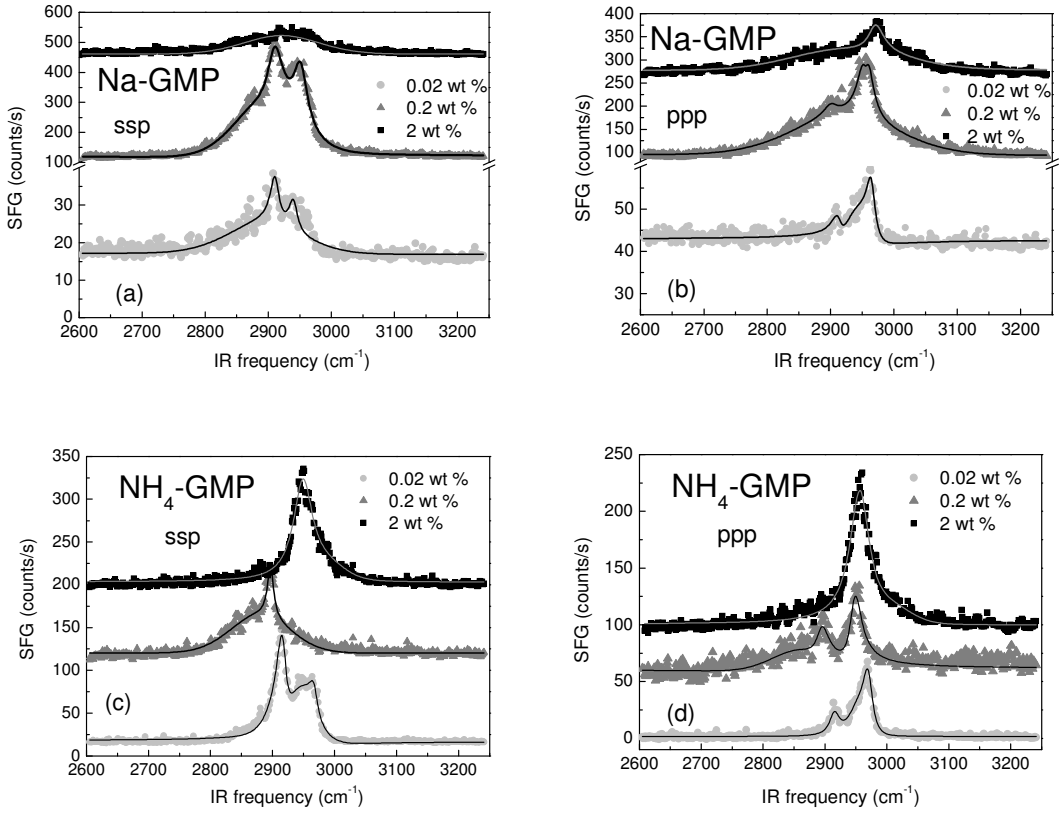

Figure 8-1: SFG spectra of sodium and ammonium GMP deposited on mica at three different concentrations for ssp (a and c) and for ppp (b and d) polarization combination. Solid lines are fits to eq. (48) and eq. (49). The spectra are offset for clarity.

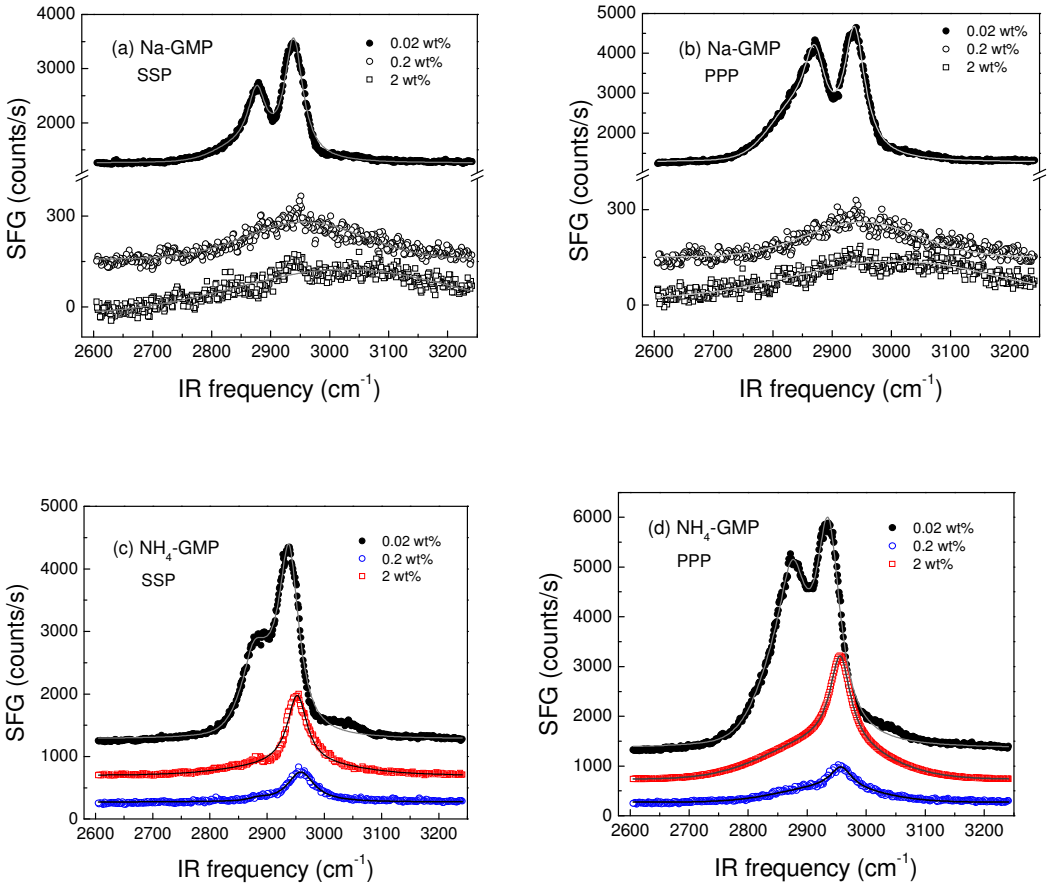

Figure 8-2: SFG spectra of sodium and ammonium GMP deposited on gold substrate at four different concentrations for ssp (a and c) and for ppp (b and d) polarization combination. Solid lines are fits to eq. (48) and eq. (49). The spectra are offset for clarity.

The SFG intensity can be roughly described by the following expression

$$I_{SFG} \propto \left|\chi^{(2)}\right|^2 \cdot I_{IR}(\nu_{IR}) I_{VIS}(\nu_{VIS}) \tag{48}$$

where $\chi^{(2)}$ is the nonlinear optical susceptibility of the second order, I_{IR} (υ_{IR}) and I_{VIS} (υ_{VIS}) are the intensities of the incident beams. For the SFG response in the frequency-domain, $\chi^{(2)}$ is generally described in terms of non-resonant and resonant contributions (coherently added Lorentzian functions); [75-77]

$$\chi^{(2)} = \chi_{NR} + \sum_n \frac{A_n}{\nu_{IR} - \nu_n + i\Gamma_n}, \text{ with } \chi_{NR} = A_{NR} \cdot e^{i\varphi}. \tag{49}$$

Here χ_{NR} is the non-resonant part of the SFG signal that originates from the substrate, A_n represents the resonant amplitude, υ_n the resonant frequency, Γ_n the damping constant of n-th vibrational mode, A_{NR} the amplitude of the non-resonant contribution and φ its relative phase with respect to the resonant contribution. All SFG data obtained at surface

structures of GMP molecules were fitted by expression (48) and taking into account relation (49).
The parameters obtained from fitting are collected in the Table 8-1 and Table 8-2. An interesting open question is why the central position of some peaks so drastically changes by changing the polarization combination and/or the concentration of the solution. In the case of SFG results on the mica substrate these modifications are especially profound for the Na-GMP.
Figure 8-1 and Figure 8-2 show the SFG results for the two GMP samples on the mica and gold substrates, respectively, deposited at three different mass concentrations. In the case of the mica substrate at very low concentrations both types of GMP show similar SFG spectra, which is consistent with the similar formation of surface structures as observed with the AFM (Figure 8-5 and Figure 8-6). Completely different behaviour for both GMP salts is observed at higher concentrations, which must be related to differences in macromolecular organization. A similar trend can be also noticed for concentration dependent SFG signal in the case of GMP structures on the gold substrate with one minor difference: the typical resonant SFG signal with two distinct vibrations is already smeared at 0.2 wt%. We can attribute such quick transition in SFG response to different properties of the gold substrate compared to mica.

	Na GMP - mica						**NH_4 GMP - mica**					
	0.02wt ssp	**0.02wt ppp**	**0.2wt ssp**	**0.2wt ppp**	**2wt ssp**	**2wt ppp**	**0.02wt ssp**	**0.02wt ppp**	**0.2wt ssp**	**0.2wt ppp**	**2wt ssp**	**2wt ppp**
φ	4.47	3.46	17.65	17.18	/	4.94	10.98	3.56	4.67	5.22	10.87	10.93
A_1	9.42	3.21	71. 24	11.03	/	/	31.87	43.19	13.41	9.36	/	/
υ_1	2911	2913	2909	2901	/	/	2914	2917	2896	2894	/	/
Γ_1	8.61	8.88	14.52	13.47	/	/	10.07	8.93	6.25	11.58	/	/
A_2	5.1	3.35	19.77	82.28	/	30.28	9.46	7.40	/	18.55	88.58	74.14
υ_2	2940	2965	2951	2955	/	2960	2969	2967	/	2947	2956	2949
Γ_2	11.6	16.3	16.3	8.6	/	15.03	38.12	50.65	/	14.2	19.16	18.61

Table 8-1: Parameters giving the best fit to the SFG data in Figure 8-1.

At this point we can make some qualitative analysis of the SFG results. At low concentrations only ppp, ssp, sps and pss signals were significant [75]. This confirms that the observed surfaces are close to isotropic, for which we know that only seven nonzero elements of nonlinear susceptibility exist and therefore the SFG signals for only four polarization combinations are nonzero (see chapter 2.1.1). This observation also indicates an average azimuthal symmetry and negligible bulk-like contributions from the adsorbates formed at low concentrations. The absence of signal for other polarization combinations is also in agreement with the AFM figures where the wire-like surface structures of the GMP developed at low concentrations exhibit the 6-fold azimuthal rotational symmetry.

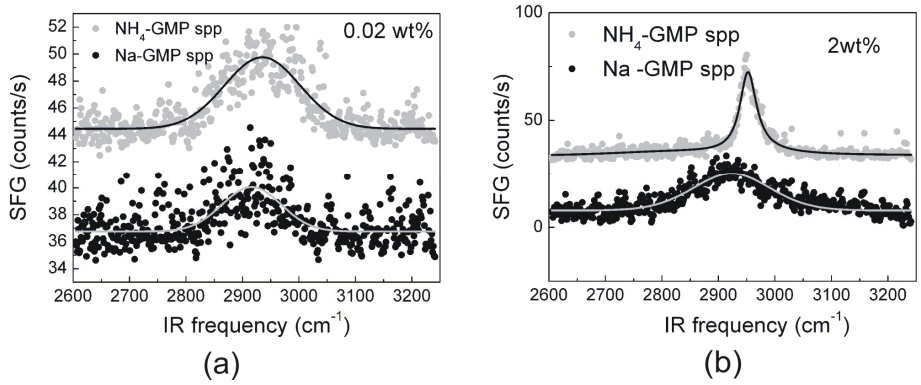

Figure 8-3: SFG spectra recorded in the spp polarization combination for film deposited at solution concentration of (a) 0.02 wt% and (b) 2 wt%. The peak in the SFG spectrum of NH4-GMP at 2 wt% is positioned at 2952 cm^{-1} with the FWHM of 18 cm^{-1}.

At higher concentrations the SFG signals of both GMP salts are profoundly different. As can be seen from Figure 8-1 (a) and (b) for c > 0.2 wt% (mica) for sodium GMP the signal saturates and its resonant part starts to decrease. The two peaks become more and more smeared. At higher concentrations (for mica above 0.2 wt% and for Au above 0.02 wt%) the ssp and ppp signals almost vanish (the spectral shape reflects the incident IR pulse spectrum), which indicates a strongly disordered adsorption layer. A completely different process takes place in the NH_4-GMP as seen from Figure 8-1 (c)(d) and Figure 8-2 (c)(d).

	Na GMP - Au(111)						**NH_4 GMP- Au(111)**					
	0.02wt ssp	**0.02wt ppp**	**0.2wt ssp**	**0.2wt ppp**	**2wt ssp**	**2wt ppp**	**0.02wt ssp**	**0.02wt ppp**	**0.2wt ssp**	**0.2wt ppp**	**2wt ssp**	**2wt ppp**
φ	5.7	4.5	/	/	/	/	3.7	9.2	8.6	5.1	2.4	6.3
A_1	51	89	/	/	/	/	28	137	/	/	/	/
υ_1	2876	2870	/	/	/	/	2875	2875	/	/	/	/
Γ_1	18	22	/	/	/	/	20.8	26.8	/	/	/	/
A_2	110	114	/	/	/	/	157	267	36	25	61	98
υ_2	2938	2937	/	/	/	/	2938	2935	2959	2957	2952	2955
Γ_2	19	21	/	/	/	/	21.4	25.0	28,6	22.8	21.0	21.1

Table 8-2: Parameters giving the best fit to the SFG data in Figure 8-2.

The signal here shows no saturation, but monotonously increases with increasing solution concentration, also for c > 0.2 wt%. Besides this we observed very interesting transition from two distinctive peaks observed at low solution concentrations to the one pronounced peak, which can be detected for almost all polarization combinations at high concentrations, even the "forbbiden" ones. The example for one such polarization combination (spp) is shown in Figure 8-3.

The appearance of a signal in the forbbiden polarization combination implies that either the azimuthal symmetry is lifted for those samples or that the bulk contributions of non-electric-dipole origin become significant. All these observations point to bulk

contribution. That the signal originates from the bulk and not from the surface was further corroborated by modifying the interfacial Fresnel factors by putting hexane solvent on top of the GMP layer prepared at high mass concentrations. As can be seen from the Figure 8-4 this almost did not affect the SFG signal.

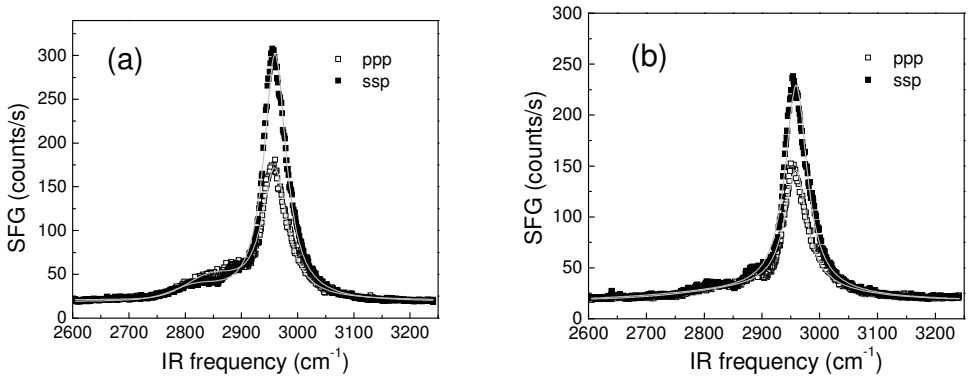

Figure 8-4: SFG spectra of NH_4-GMP deposited from solution at 2 wt% on the mica substrate recorded (a) with the sample placed in air and (b) sample treated by hexane.

In the case of GMPs on Au substrate the signal starts to decrease with increasing concentration (c > 0.02 wt%) for both types of GMPs indicating a more irregular surface structure which increases the scattering (Figure 8-2 (a) and (b)). Again we can notice different SFG resonant response for both GMPs where for Na-GMP we can not see any resonant SFG response at high concentrations, but for NH_4-GMP we find again an interesting transition from two distinctive peaks observed at low solution concentrations to the one pronounced peak at high concentrations.

8.2.2 AFM

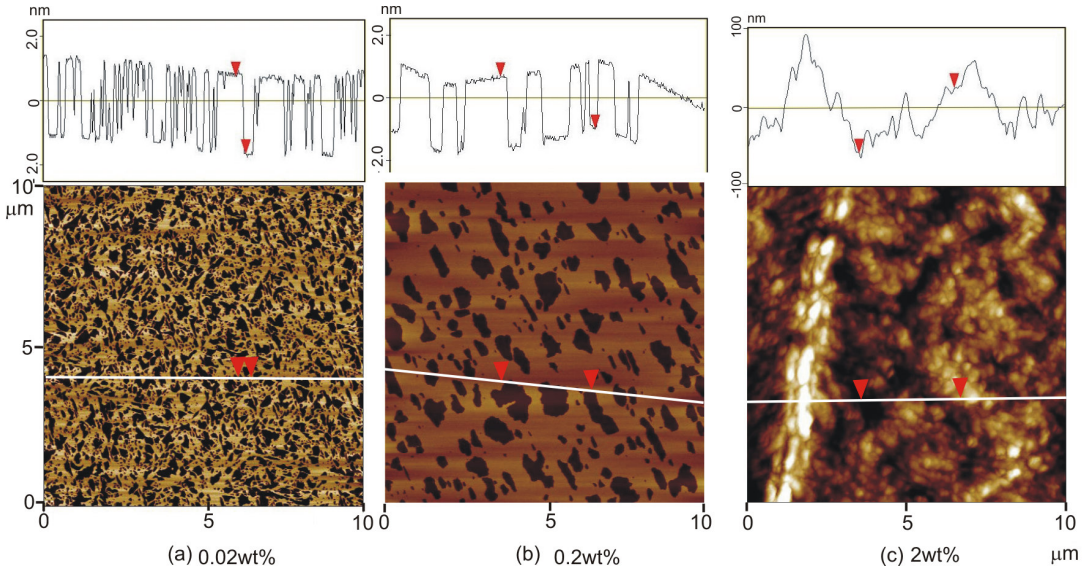

Figure 8-5: AFM images of sodium GMP deposited on mica substrate at different solution concentrations: (a) 0.02, (b) 0.2 and (c) 2.0 wt%. Note the different height scales in the different panels.

Figure 8-5 and Figure 8-6 show AFM images of surface morphology of the GMP samples on the mica substrate used for SFG measurements. For the lowest concentration (c ~ 0.02 wt%), close inspection of the AFM images reveals hexagonal assembly of wire-like aggregates for ammonium GMP (Figure 8-6 (a)). In the case of sodium GMP (Figure 8-5 (a)) a corrugation-like structure with some parts indicating wire-like aggregates can be observed.
For c ~ 0.2 wt% a terrace-like structure with the step height of approximately 2.5 nm is developed for both types of GMP salt (Figure 8-5 (b) and Figure 8-6 (b)), with significantly larger areas of homogeneous height for sodium GMP. For c ~ 2.0 wt% a rough and irregular arrangement of deposited material appears for both solutions (Figure 8-5 (c) and Figure 8-6 (c)). The average roughness of the films deposited from c ~ 2 wt% solutions, as determined by AFM, was approximately 200 nm for the Na-GMP and 50 nm for the NH_4-GMP. The roughness is more pronounced in the Na-GMP sample, which indicates more disordered bulk structures.

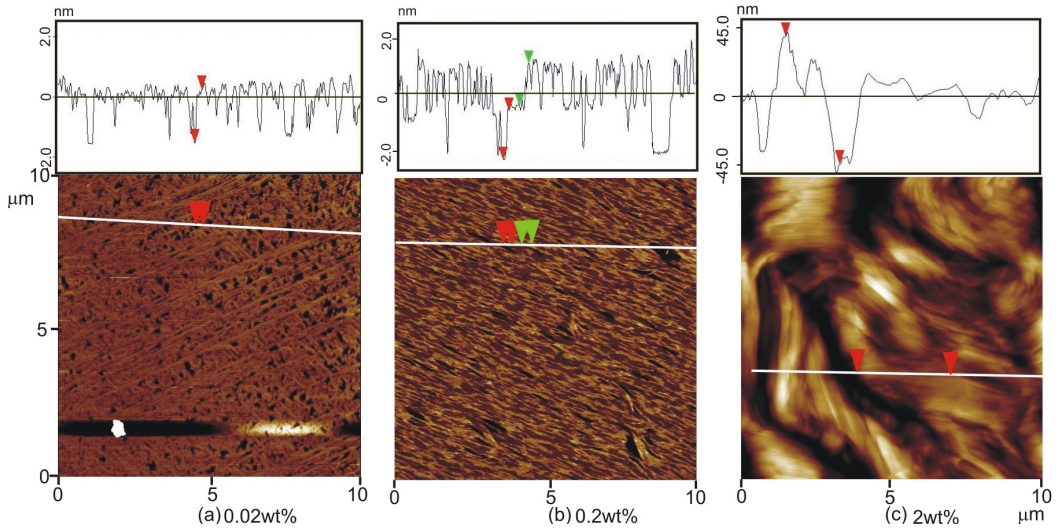

Figure 8-6: AFM images of ammonium GMP deposited on mica substrate at different solution concentrations: (a) 0.02, (b) 0.2 and (c) 2.0 wt%. Note the different height scales in the different panels.

We also captured the surface topography of GMP structures on the flame annealed gold substrate. Figure 8-7 and Figure 8-8 show AFM images of surface morphology of the sodium and ammonium GMP, respectively at different mass concentration of the solution from which the GMP deposition was made. AFM images at low concentrations (0.02 wt%) reveal similar surface morphology for both GMPs with relatively small surface roughness. A completely different story is the morphology at higher concentrations. It seems that again the Na-GMP surface morphology indicates somehow more rough and congested structures, while NH_4-GMP shows smoother surface conformation. All these cognitions very well coincide with very similar SFG signals at low concentration and with large contrast in SFG response at higher concentrations for both types of GMP salts.

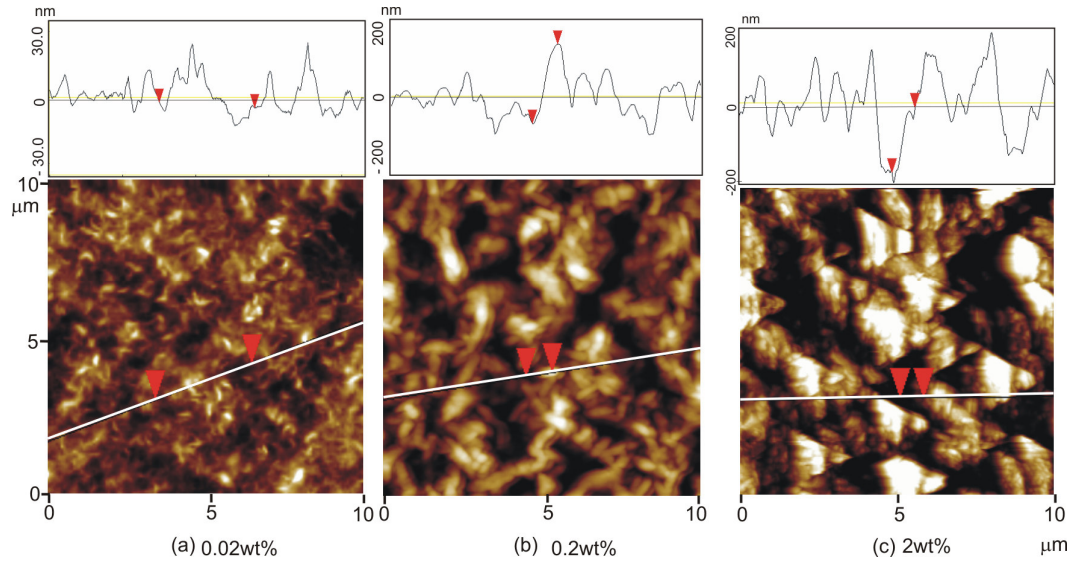

Figure 8-7: AFM images of sodium GMP deposited on gold substrate at different solution concentrations: (a) 0.02, (b) 0.2 and (c) 2.0 wt%. Note the different height scales in the different panels.

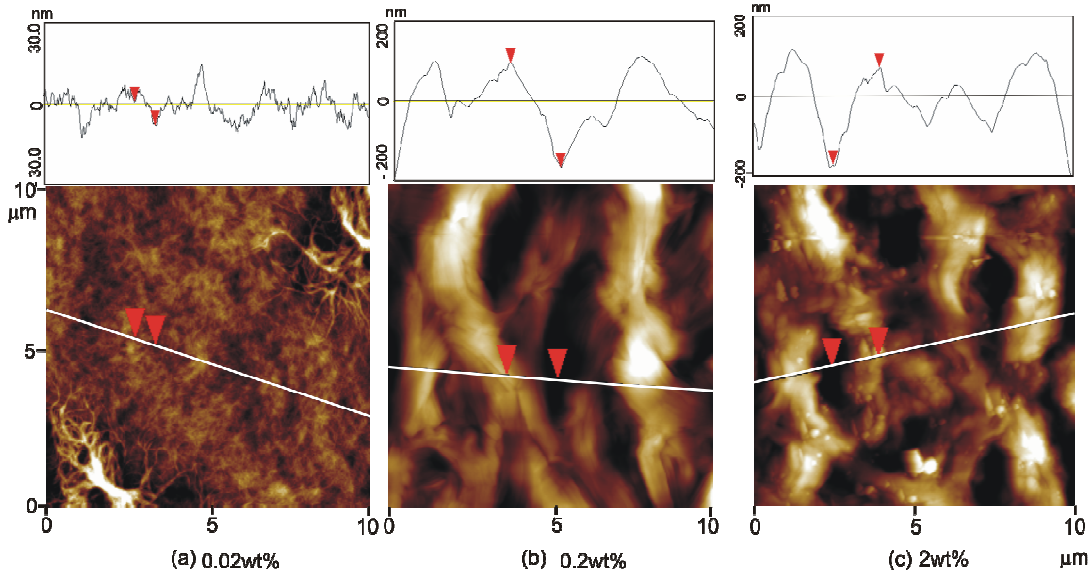

Figure 8-8: AFM images of ammonium GMP deposited on gold substrate at different solution concentrations: (a) 0.02, (b) 0.2 and (c) 2.0 wt%. Note the different height scales in the different panels.

8.3 Discussion

The AFM as well as the SFG analysis reveal that the structures of GMP adsorbates on solid substrates strongly depend on the concentration of the solution used in the deposition. The AFM images on the mica substrate show that at low concentrations long, wire-like aggregates are formed, which at higher concentrations link into flat terraces. At the highest concentrations (2 wt%) these terraces become less and less pronounced until finally very irregular, rough, and congested structures are formed. From AFM images no

details on internal organization of these structures can be revealed. By comparing all AFM images at 2 wt% we can only conclude that surface roughness is less profound for NH_4-GMP samples. On the other hand, the SFG results seem to be quite different showing strong dependence on the solution concentration, and at the same time strong dependence on the type of the ions present in the solution used for GMP deposition. At low solution concentrations the SFG spectra of both salts (sodium and ammonium) are quite similar, but at higher concentrations they exhibit strong differences. This signifies that the internal organization of the bulk films is different.
In general there are several possible sources of the SFG signal from our samples: (a) the interface between air and GMP, (b) the bulk structure of GMP, (c) the interface between GMP and the substrate, and (d) the substrate itself. We believe that at concentrations $c > 0.2$ wt% the bulk contribution of the GMP film apparently becomes a dominant source of the SFG radiation, especially for NH_4-GMP. This was also confirmed by hexane treatment of the sample. After this treatment the SFG signal did not change drastically, which confirms that the SFG signal originates from the bulk. If that were not the case, the SFG signal would be significantly different due to the significant modification of the GMP surface. The observation that the resonant SFG signal for dense Na-GMP adsorbates almost completely vanishes, indicates a very disordered bulk structure for this type of GMP salt. The changes in the SFG spectra of the NH_4-GMP, on the other hand, signify a formation of an ordered bulk structure, which lacks centrosymmetry. The AFM images in Figure 8-6 and Figure 8-8 in fact suggest a helical bulk structure of the NH_4-GMP, which is not unexpected [39]. The formation of a helical bulk structure can enhance a chiral response of the second-order nonlinear susceptibility [78-83], which can explain the existence of a strong resonant SFG peak in thick NH_4-GMP films.

8.4 Conclusions

The combination of both techniques, i.e. AFM and SFG provides an important complementary information on the self-assembly of the Guanosine 5´-monophosphate on the solid substrates. The SFG spectra showed that the resonant response of the C-H vibrations is very sensitive to structural ordering of adsorbed films. This high sensitivity to structural modifications can serve as an efficient tool for investigation of GMPs crystallization on solid substrates.

Chapter 9

Experiment of Free-induction decay Sum-frequency generation

In general there are two options for performing the SFG measurements. The first is the so called frequency domain SFG described also in Chapter 7 and the second is the so called free induction decay SFG (FID-SFG), in which the temporary short VIS pulse is delayed with respect to the temporary short IR pulse. This enables direct observation of the temporal decay of non-linear polarization induced in the sample.

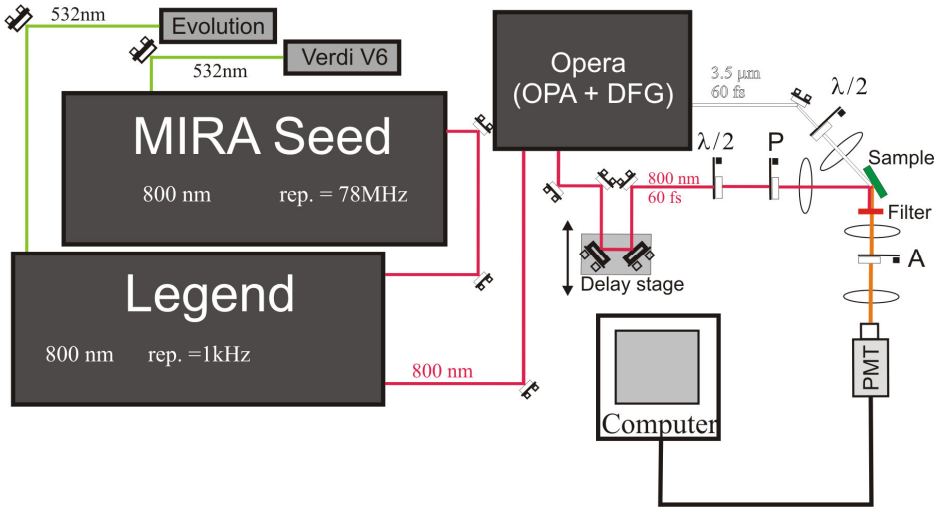

Figure 9-1: Experimental setup for Free induction decay Sum-frequency generation installed at Jožef Stefan Institute. The symbols in the figure represent the following optical components **P**: Polarizer, **λ/2**: half-waveplate and **A**: Analyzer.

9.1 Mira-Legend-Opera laser system

Pulses from the Mira laser oscillator are directed into the Coherent Legend unit which is a titanium sapphire laser amplifier pumped by a Nd:YLF (Coherent Evolution) 1 kHz Q-switched laser operating at a wavelength of 532 nm with an average power of 30 W. Laser radiation from the Legend unit has a repetition rate of 1 kHz with energy per pulse and pulse duration 2.5 mJ and 60 fs, respectively.

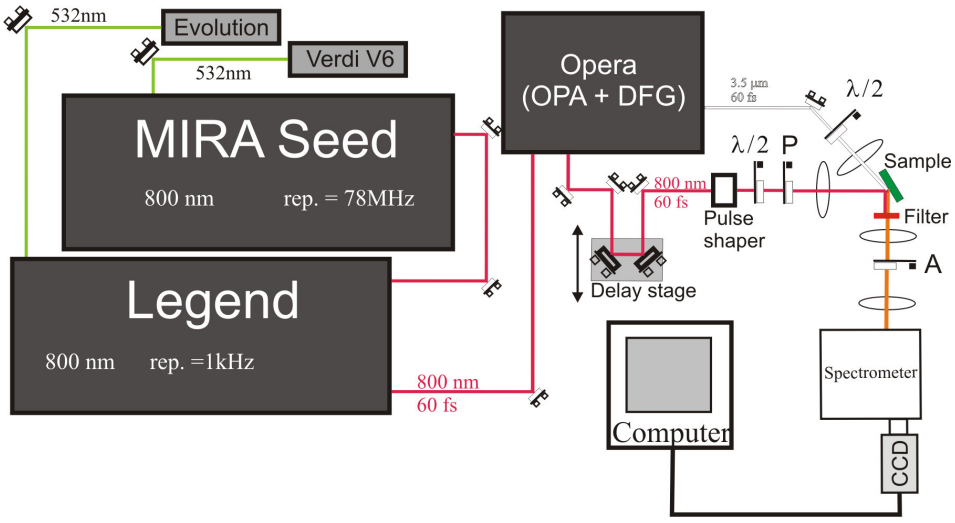

Figure 9-2: Experimental setup for Sum-frequency generation spectroscopy installed at Jožef Stefan Institute.

The 2.5 mJ of pulse energy is split 50:50 and the 1st half is used to generate the IR pulses with the wavelength tunable between 1.1-12 μm (9000 cm^{-1}- 830 cm^{-1}) in the Coherent Opera system, while the 2nd half is used for other experiments. The 2nd half is further split and only part of the energy (6 μJ) is used as a VIS part of the IR - VIS FID-SFG experiment. IR and VIS beams are focused on the sample at incident angles of 37° and 42°, respectively. The spot size for both beams ranges between 150 – 200 μm.
As a detector in the FID-SFG setup we used commercially available photomultiplier tube (PMT, Electron Tubes, model 9863/350B) operating in the gated regime (detailed description is in Chapter 3). This PMT has an infra-red sensitive photocathode layer S20 and 14 BeCu dynodes of linear focused design for fast timing and extended linearity. The active diameter of the PMT is 9 mm with the quantum efficiency around 8% at 650 nm. The PMT was cooled down to -20ºC in order to reduce the dark current down to a few counts per second. The typical spectral response and voltage gain characteristics for this PMT are shown on Figure 9-3.

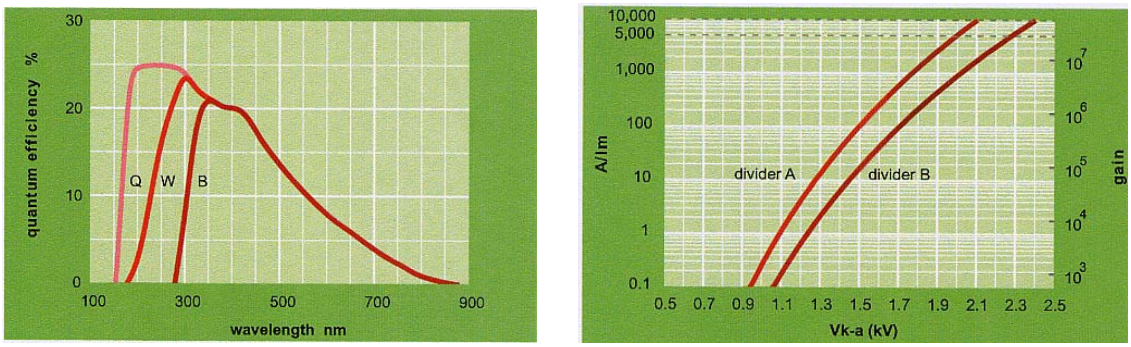

Figure 9-3: The spectral response (left) and voltage gain characteristics for PMT 9863/350B [Electron tubes].

In the frequency domain the spectrally narrowed pulses are used as a VIS part of the IR - VIS SFG experiment. They are obtained by sending 0.5 mJ of the Legend pulse energy

through commercially available etalon (pulse shaper). Pulses from the pulse shaper have a spectral width of approximately 5 cm^{-1} and their time duration is a couple of ps. The energy per pulse is approximately 6 μJ. As a detector in the frequency-domain SFG setup an imaging monochromator (Acton SP-2300 with motorized turret for three gratings) with an intensified Charge Couple Device (CCD) camera (Princeton Instruments) was used as a detector. The monochromator contains two gratings, one with 1200 lines/mm and the other with 600 lines/mm. Both gratings have a blaze wavelength of 500 nm and their size is 68x68 mm^2. The CCD camera was operating in gated regime. The gate was synchronized with the Legend laser system. The temporal delay between both, the Legend laser and gate of the CCD camera was adjusted to 90 ns. The width of the gate was around 60 ns. We cooled the CCD camera down to -25 ℃ to get rid of the thermal noise as much as possible.

Chapter 10

Surface structures of heptadecanoic acid

In Chapter 10 we will show that SFG can be a powerful technique for investigating monolayers of organic molecules. We will introduce Langmuir and Langmuir-Blodgett techniques for preparation of such monolayers and describe investigations of fatty acid molecules in various environments (on the water subphase and on the solid substrate) prepared by different deposition conditions.

10.1 Introduction

The Langmuir-Blodgett (LB) technique was introduced by Irving Langmuir [84] and later applied by Katherine Blodgett [85,86]. The technique has been a subject of scientific exploration for most of the last century and is still an interesting research field nowadays. The interest for LB films has significantly grown in the 1970s after the paper of Hans Kuhn et.al. on energy transfer in multilayered systems was published. This introduced the idea of molecular engineering. So by using the LB technique one can position certain molecular groups at precise distances to others, which enabled the production of new thin film materials controlled at the molecular level.
Similar to 3D materials, also 2D films can exist in various phases: gas, liquid (expanded phase) and solid (condensed phase). The liquid state is thought to be the middle state between the gas and solid state. The constituents in a liquid state neither occupy a specific average position, nor remain oriented in a particular way. The constituents in a liquid state are free to move around and their motion is random. The liquids are also known to be isotropic, which means that their physical properties are direction-independent. Sometimes it is hard to distinguish between liquid and gas state, the major difference between both is that the forces between constituents for liquids are strong enough to hold them together, which is not true for gases. Liquids can flow and change their shape in response to weak external forces. On the other hand gases are much more compressible compared to liquids and the interatomic distance is bigger than in liquids. In the condensed phase the molecules are closely packed and remain oriented in a particular direction.

10.1.1 Surface pressure

In solutions diluted molecules experience attractive forces from the solvent molecules. In the bulk the net attractive force on the molecules is zero, while near surface (or interface)

it is nonzero. This surface force causes a drag of diluted molecules from the surface into the bulk. However, for the air-water interface (most common case) a net attractive force of the air molecules is smaller with respect to the net attractive force of water molecules acting on diluted molecules near the surface. Macroscopically speaking this reflects as an increase in the surface tension of the water (liquid).
The surface active or amphiphilic molecules tend to accumulate near the surface and therefore decrease the surface tension. This reduction of surface tension is known as surface pressure. By knowing a number of molecules on the surface one can control surface pressure π as a function of the area A occupied by a single molecule. The isotherms $\pi(A)$ of monolayers deposited on the water surface are measured by monitoring the surface pressure during compression and expansion of the monolayer. The surface pressure is measured with a paper plate, also known as Wilhelmy plate (see Figure 10-1) which is hanging on the LB scale with its bottom end dipped into the water. The scale is calibrated in order to take into account the net force acting on the Wilhelmy plate (gravitational force, buoyant force and surface tension force)

$$F = F_g + F_{buoyant} + F_{surf.pressure}, \tag{50}$$

$$F_{net} = \left(\rho_p lwt\right) g - \left(\rho_l dwt\right) g + 2\left(w+t\right)\gamma\cos\left(\theta\right), \tag{51}$$

where w is the width, t the thickness, and l the height of the Wilhelmy plate, while ρ_p is the paper density, ρ_l the liquid density, and γ the surface tension. When Wilhelmy plate is dipped into the water, the paper becomes wet, which eliminates the buoyant force. After this the scale can be renormalized in order to eliminate also the gravitational force of the Wilhelmy plate. With the last step the scale is prepared to monitor only the force contribution from the surface pressure in equation (51).

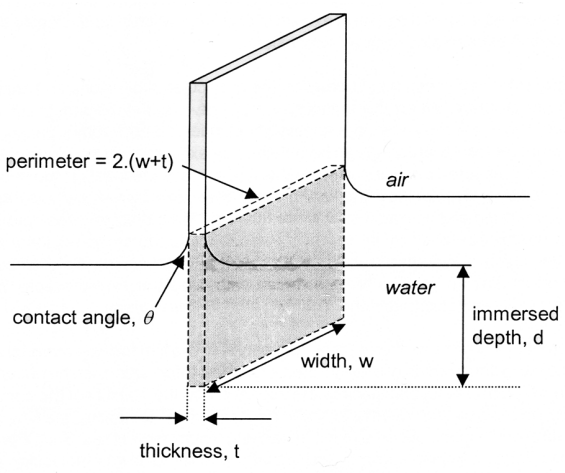

Figure 10-1: The Wilhelmy plate dipped into the water [87].

10.1.2 Monolayers of organic molecules

We will now deal with monolayers of organic molecules captured between gas and solid environment (Langmuir-Blodgett films) or gas and liquid environment (Langmuir films), which are schematically shown in Figure 10-2. The molecules that will be discussed in this chapter are so called monolayer-forming molecules composed of two parts: a part that by itself would mix with water (also known as hydrophilic or water-loving) and the other part that by itself does not want to mix with water (hydrophobic or water-hating). Such molecules are also known as amphiphilic molecules.

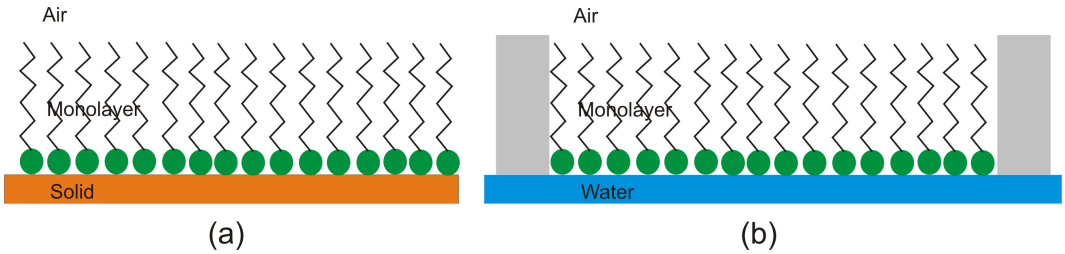

Figure 10-2: (a) Langmuir-Blodgett and (b) Langmuir film of amphiphilic molecules.

The two important groups of amphiphilic molecules are soaps and phospholipids. Such compounds are also called surfactants.

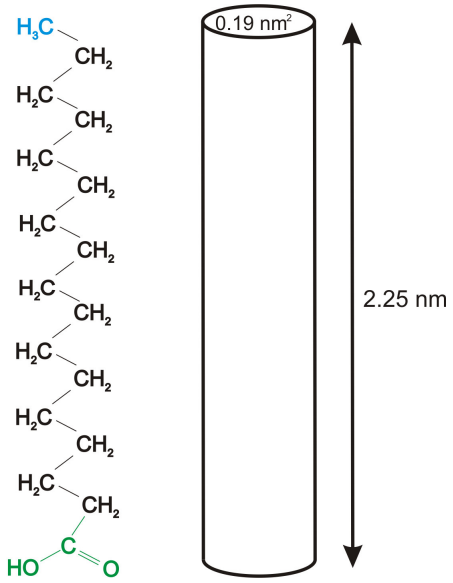

Figure 10-3: Chemical formula for heptadecanoic (margaric) acid. The schematic drawing of its cylindrical shape with lateral dimension of 2.25 nm and cross-section area of 0.19 nm^2 is also shown.

Phospholipids are known to be building block of living cells. So from this point of view the studying of these molecules in different systems can help us understand their role in cellular processes. The simplest amphiphilic substances are long-chain fatty acids, with the general chemical formula $C_nH_{2n+1}COOH$. One of those is heptadecanoic acid (HDA) also known as margaric acid ($C_{16}H_{33}COOH$). This molecule has a cylindrical shape with

the length of approximately 2.25 nm and a cross-section of about 0.19 nm^2 (Figure 10-3) [88].
It consists of 15 methylene (CH_2) groups forming a long hydrocarbon chain (tail) with methyl (CH_3) at one end and carboxyl (COOH) group (head) at the other. Later is polar and so exhibit hydrophilic interaction with water molecules, while the hydrocarbon chain is hydrophobic and exhibit repulsive interaction with water molecules. A balance between the hydrophilic and hydrophobic properties provides the monolayer forming abilities of the heptadecanoic acid. If the hydrocarbon tail was too short, or the polar head too strong, then the material would simply dissolve in the subphase (in our case water).

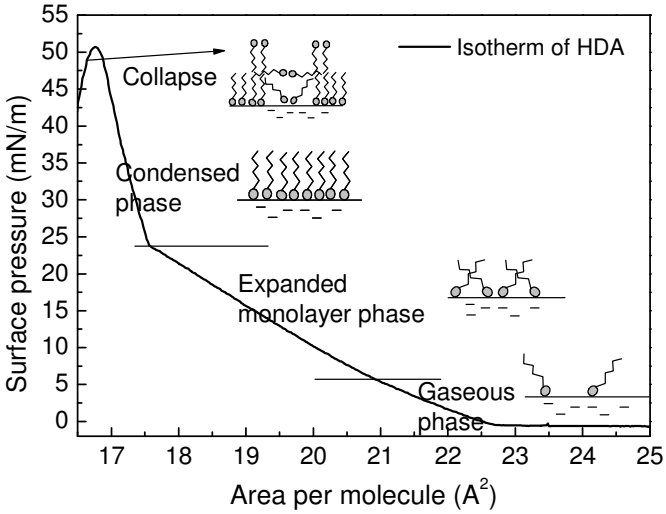

Figure 10-4: Surface pressure of heptadecanoic acid on the water as a function of area per molecule.

When amphiphilic molecules are spread (distributed) on the water surface they organize in various configurations and can under certain external condition undergo several phase transitions. The most usual phases were described earlier in this subsection. The corresponding phase transitions can be monitored by changing the surface tension of the monolayer by changing the position of the barriers in the Langmuir-Blodgett trough (see Figure 10-2 (b)).
Translation of the barriers results in modification of the area occupied by a single molecule in the monolayer. This is the 2D-equivalent of the volume modification when measuring the p-V diagram for solid-liquid-gas phases of conventional materials. The corresponding 2D phase diagram showing all phases of heptadecanoic acid is presented in Figure 10-4. The area per molecule can be calculated from the total area of the film A from the following expression:

$$a = \frac{A}{cN_A V}, \tag{52}$$

where N_A is Avogadro number, c the specific molar concentration of the spreading solution, V its volume and A the total monolayer area.

In the gaseous phase distance between two neighboring molecules is large, so the interactions between them are very small. By reducing the total area of the monolayer the molecules are approaching each other and therefore their hydrocarbon tails can begin to interact with each other. In the case of heptadecanoic acid this gas-liquid phase transition occurs somewhere around 5 mN/m. The hydrocarbon tails of molecules in the expanded monolayer phase have random orientations with their polar groups in contact with the water subphase. The phase transition from liquid to solid phase occurs at around 24 mN/m. In the condensed phase the molecules are closely packed and are oriented with hydrocarbon chain pointing away from the water surface. All these phases are schematically shown in Figure 10-4. The surface area can be further compressed to the point, at which it is impossible to increase the surface pressure any further. At this point the area of the film decreases, if the pressure is kept constant or the pressure falls, if the film is held at constant area. This event is known as collapse of the monolayer. At this point the forces acting on the molecules in the monolayer are so high that the molecules are forced out of the monolayer. If we made an estimation for such force, we can see that the surface pressure around 100 mN/m acting on a 2.5 nm thick layer of molecules corresponds to a 3D pressure of 400 bar. The point of collapse depends on many factors such as the history of the monolayer or the rate at which the monolayer is being compressed. When the collapse occurs, molecules move out of the monolayer as schematically shown in Figure 10-4.

10.2 Experimental

10.2.1 Langmuir and Langmuir-Blodgett techniques

For Langmuir-Blodgett and Langmuir techniques we used a commercial trough from NIMA Technology (model 112D, United Kingdom) with a subphase area of 85 cm^2 (Figure 10-5).

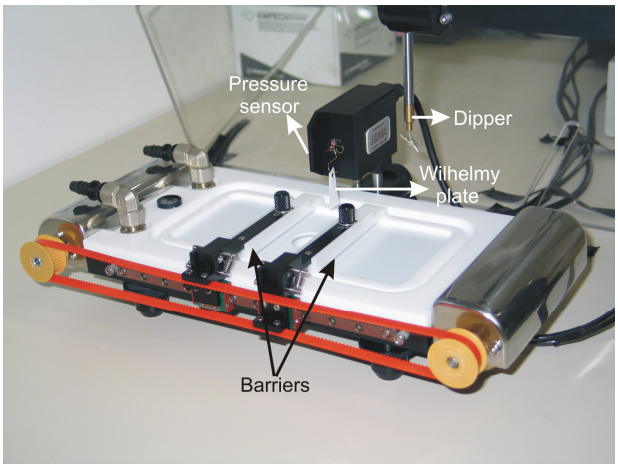

Figure 10-5: Langmuir-Blodgett trough.

The barriers of the LB trough were computer controlled via a stepped micromotor. The very important parts of the LB trough are also the pressure sensor with Wilhelmy plate (for measuring surface tension) and the dipper (for preparation of LB films), which were as well computer controlled by commercially available software from NIMA Technology.

For the preparation of Langmuir and Langmuir-Blodgett films we used heptadecanoic acid (> 98% purity) purchased from Sigma Aldrich Inc. The material was first dissolved in chloroform (Merck, Germany 99 – 99.4% purity) at concentration of 0.5 mg/ml and than spread on the pure water surface in the previously cleaned LB trough. We used the standard cleaning procedure for LB trough, i.e. first the trough was cleaned with isopropanol for several times, afterwards we distributed a small volume of water and aspirated it from the trough in order to remove the dust accumulated during cleaning with isopropanol. After this the calibration of the pressure sensor by a special balance and 100 mg weight was performed. This was necessary in order to control the surface pressure of the clean subphase and the monolayer of HDA molecules on the water subphase. After the cleaning and calibration procedures we recorded the isotherm (surface pressure vs. area of the through) of the pure water subphase. If the water surface is clean, the pressure does not show any drastic changes during the compression or relaxation process (see Figure 10-6).

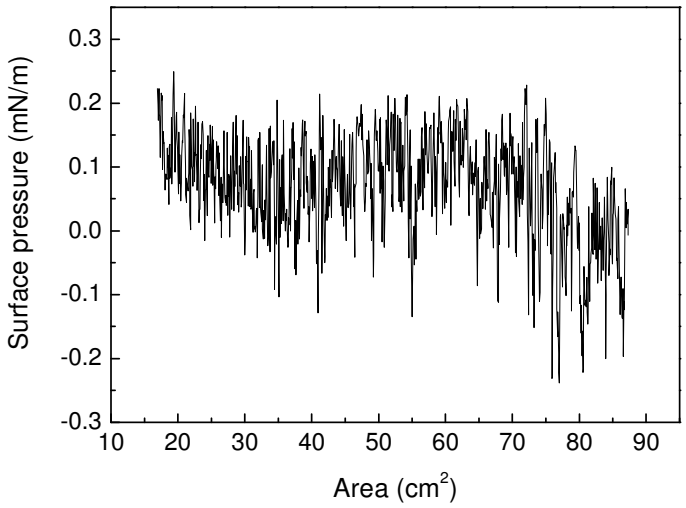

Figure 10-6: Surface pressure of pure water as a function of surface area.

With the last step everything was prepared for dispersion of approximately 30 µl of HDA solution in chloroform on the water surface. The HDA molecules were spread on the water surface with a microsyringe. After spreading the film was left for 20-30 min before compression. This was necessary due to the chloroform evaporation and equilibration of a HDA film on the water surface. In the proceeding stage the film was compressed to the required surface pressure (5 mN/m, 15 mN/m and 25 mN/m) by moving the computerized LB barriers with a compression velocity of 5 mm/min. After obtaining the target pressure the film was left to stabilize for approximately 40 min in order to stabilize and relax before further investigations with sum-frequency generation or in the case of LB deposition before further transfer on solid substrates. In the later case the HDA molecules were transferred onto two types of solid substrates: (a) chemically cleaned

fused silica plates (8 mm x 25 mm x 1 mm size) and (b) freshly cleaved mica substrates. For cleaning the fused silica substrates were immersed in piranha solution (1:3 ratio of H_2O_2:H_2SO_4) for 10 min and left in water until they were used in the LB preparation procedure. During the LB preparation the surface pressure was kept constant either at 5 mN/m, 15 mN/m or 25 mN/m. The elevation rates were 0.5 mm/min at 5 mN/m and 15 mN/m, and 0.1 mm/min at 25 mN/m.
We performed both Frequency-domain and FID-SFG measurements on the Langmuir and Langmuir-Blodgett films at different surface pressures. The detailed description of both setups is given in the previous chapter. After SFG measurements the films were transferred onto solid substrates and again the SFG analysis was performed. After this the LB films were probed also by AFM. All experiments including sample preparation, SFG spectroscopy and AFM were performed at room temperature (22-23°C).

10.3 Results

10.3.1 SFG

The SFG results for Langmuir films of HDA molecules at various surface pressures are shown in Figure 10-7 and in Figure 10-8. The results are given for ssp and sps polarization combinations, respectively. Heptadecanoic acid exhibits three vibrational peaks in the region of C-H vibrations, as reported in the literature [89-91]. The first peak at 2875 cm^{-1} arises from the symmetric stretch of the methyl (CH_3) group, the second at around 2935 cm^{-1} is associated with CH_3 symmetric bend overtone enhanced by Fermi resonance, and the third peak at around 2958 cm^{-1} is related to CH_3 asymmetric stretching vibration. These vibrational modes correspond to vibrations of methyl group on the hydrocarbon tail of the heptadecanoic acid. In the FID-SFG measurements we basically observed two types of signals. In the case of ssp polarization combination we observed a quantum-beat pattern of the FID-SFG signal. This corresponds to the interference (beating) of the two strongest vibrational modes of methylene group, which is also in agreement with the SFG spectra for the same polarization combination. Actually the third peak reported in the literature was hardly observable in our spectra indicating that the resonance is weak or even has negative amplitude [89]. For sps polarization combination only one peak is noticed in the SFG spectra which is also confirmed by the FID-SFG measurements, in which a simple exponential decay without any interference pattern is observed. For the other two polarization combinations (ppp and pss) the signals were very low, mostly hardly resolved from the noise (background), and therefore they are not included in further studies.
In case of the two vibrational contributions the free induction decay SFG signal can be peaks described by the following form

$$I_{SFG} \propto A_1 \exp\left(-\Gamma\left(t-t_0\right)\right) + A_2 \sin\left(2\pi\Delta\nu\left(t-t_0\right)-\varphi\right)\exp\left(-\Gamma\left(t-t_0\right)\right) \qquad (53)$$

where the φ is the phase, $\Delta\nu$ is the beating frequency and Γ is the damping constant. The beating frequency obtained from fitting all FID-SFG data for ssp polarization

combination to relation (53) is $\Delta\upsilon$ = 1.95 THz. This is in good agreement with the peak difference obtained from the SFG spectra recorded in ssp polarization combination ($\Delta\upsilon$ = 70 cm^{-1} = 2.11 THz).

The detailed inspection of the pressure-area isotherms of all Langmuir films (Figure 10-4) indicate the phase transitions from condensed to expanded and from expanded to gaseous phase, through which the molecular tails are becoming more and more disoriented. This results in intensity decrease of the SFG signal with decreasing surface pressure for both polarization combinations (Figure 10-7 and Figure 10-8).

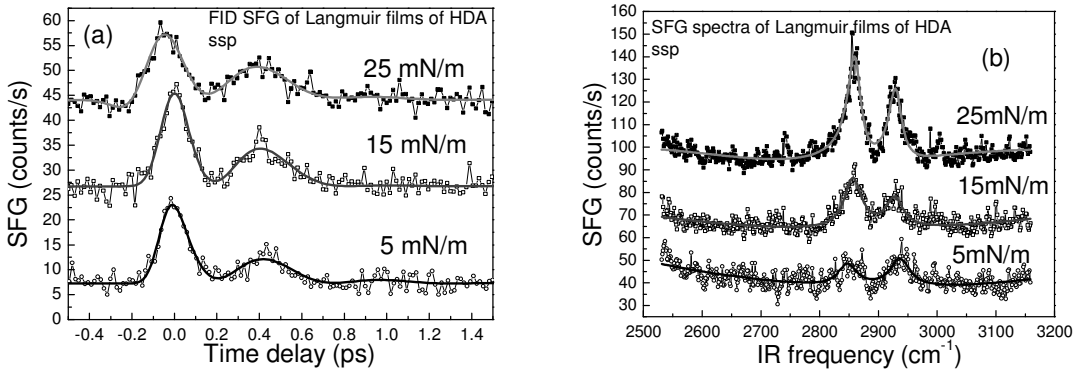

Figure 10-7: (a) Time domain SFG signals and (b) the corresponding SFG spectra of Langmuir film of HDA molecules at different surface pressures (ssp polarization combination). The data are offset for clarity.

The FID-SFG signal for sps polarization combination is very close to a single exponential decay pattern (dumped oscillator with single frequency) at all measured surface pressures, which is again in agreement with the SFG spectra, in which only a single resonance is observed.

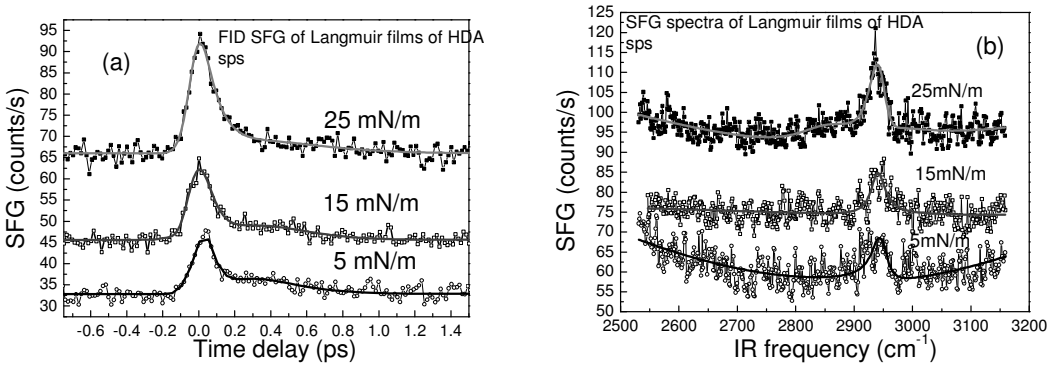

Figure 10-8: (a) Time domain SFG signals and (b) the corresponding SFG spectra of Langmuir film of HDA molecules at different surface pressures (sps polarization combination). The SFG data are offset for clarity.

In contrast to Langmuir films, the SFG intensities for Langmuir-Blodgett films (deposited on the fused silica or on the mica substrate) do not decrease monotonically, but are more or less independent of the surface pressure used during deposition. On the other hand other characteristics of the observed responses for both polarization combinations are very similar as for Langmuir films (from Figure 10-9 to Figure 10-11). Almost the same

pattern is present for both types of films (Langmuir and Langmuir-Blodgett) in the same polarization combinations i.e. two vibrations for ssp and a single vibration for sps polarization combination. In some cases the appearance of the CH_3 symmetric stretch (2875 cm^{-1}) was also observed in Langmuir-Blodgett films for sps polarization combination and for both types of substrates. This can indicate relatively minor conformational changes during the transfer from the water subphase to the solid substrate, for instance the development of double layer

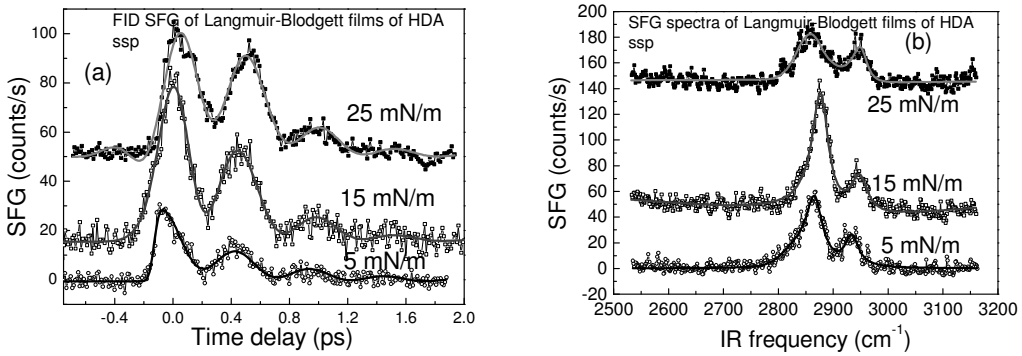

Figure 10-9: (a) Time domain SFG signals and (b) the corresponding SFG spectra of Langmuir-Blodgett film of HDA molecules on fused silica substrate deposited at different surface pressures (ssp polarization combination). The data are offset for clarity.

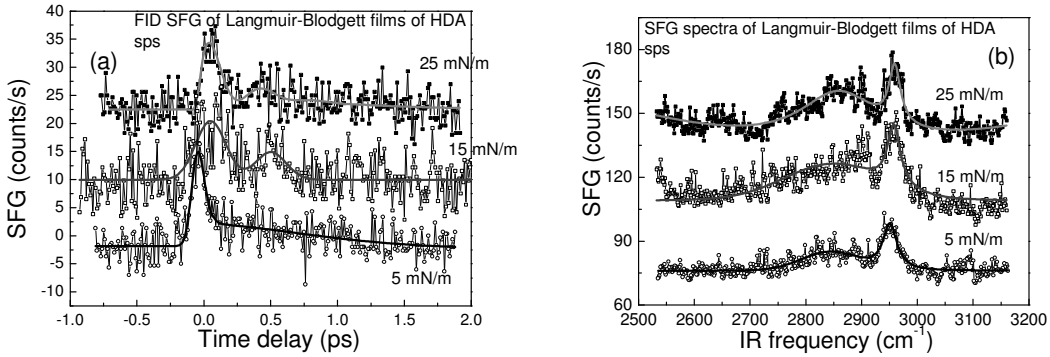

Figure 10-10: (a) Time domain SFG signals and (b) the corresponding SFG spectra of Langmuir-Blodgett film of HDA molecules on fused silica substrate deposited at different surface pressures (sps polarization combination). The data are offset for clarity.

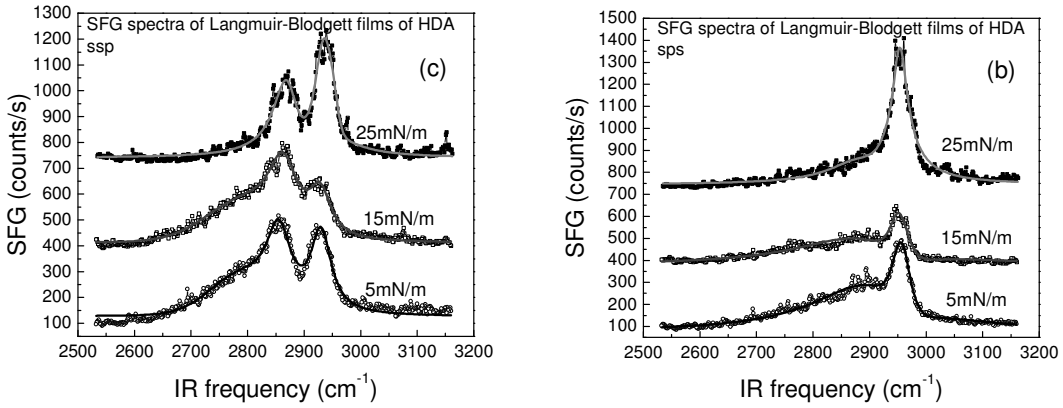

Figure 10-11: SFG spectra of Langmuir-Blodgett films of HDA molecules on the mica substrate deposited at 3 different surface pressures for (a) ssp and (b) sps polarization combinations. The spectra are offset for clarity.

10.3.2 AFM

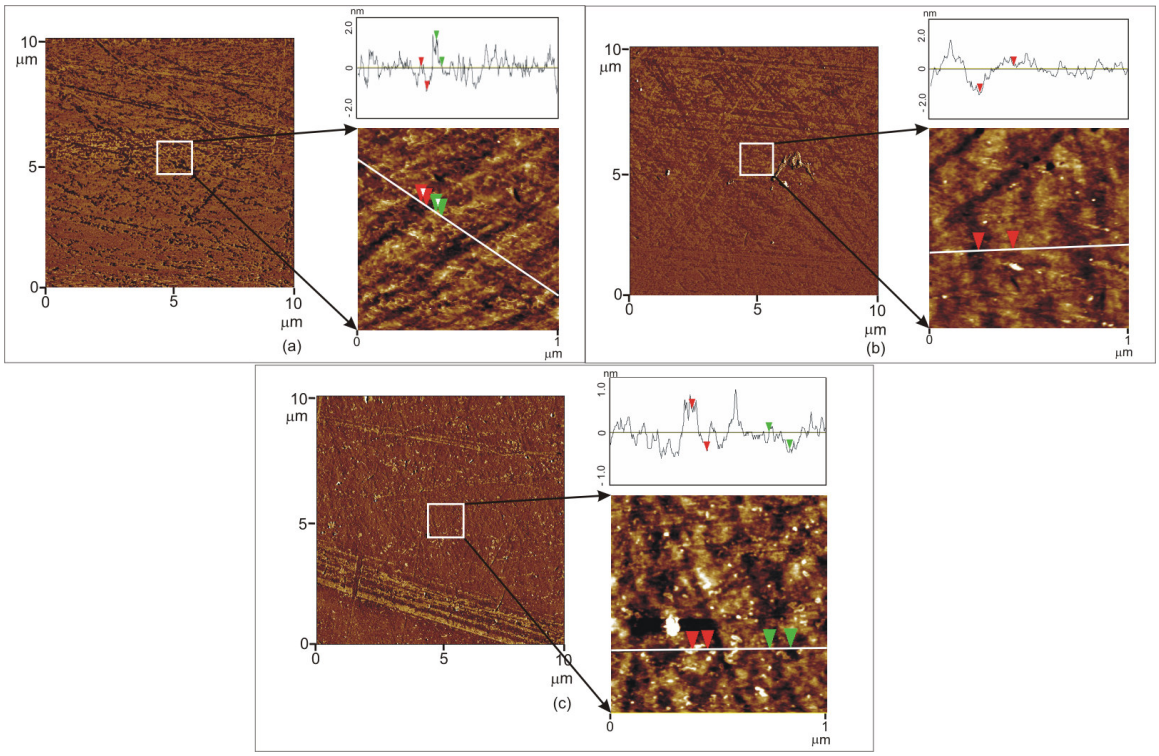

Figure 10-12: AFM images of Langmuir-Blodgett films of HDA molecules on the fused silica at different surface pressures: (a) 25 mN/m, (b) 15 mN/m and (c) 5 mN/m.

Figure 10-12 and Figure 10-13 show AFM images of the surface topography of HDA molecules on fused silica and mica substrates, respectively. The images indicate that surface density of the molecules does not depend very drastically on the surface pressure

used during the LB film transfer. One would expect that the density is largest for the surface pressure of 25 mN/m, since the HDA molecules already develop a condensed phase around this pressure. However this was usually not the case. We examined large areas of the LB films and for the majority of the LB films we observed variable surface structure within the area of observation. This indicates inhomogeneous film formation during the deposition. As a consequence of the inhomogeneity Figure 10-14 (a) clearly shows significant variation of the SFG intensity obtained at 3 different spots on the LB film, even though the spectra were recorded at the same conditions and within a reasonable time interval (not more than 20 min). The AFM images in Figure 10-14 (b) additionally confirm the previous statement. In the case of Langmuir films such variations in surface structures were not observed (SFG spectra in Figure 10-15).

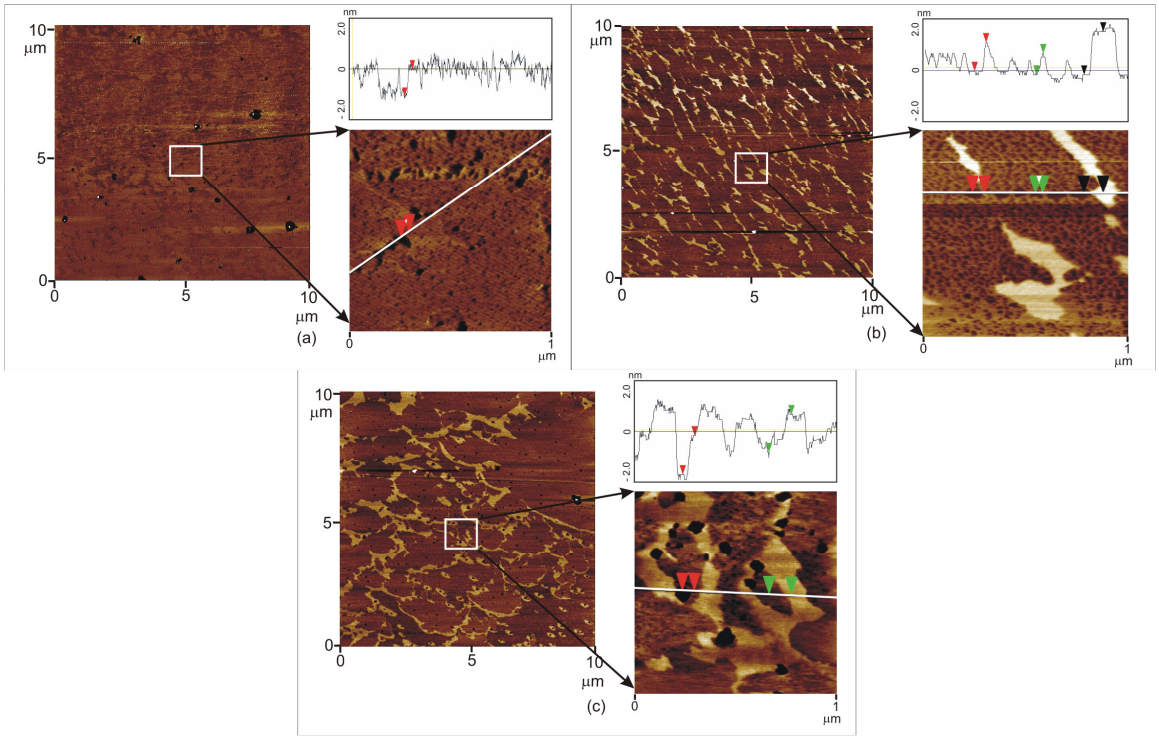

Figure 10-13: AFM images of Langmuir-Blodgett films of HDA molecules on the mica substrate prepared at different surface pressures: (a) 25 mN/m, (b) 15 mN/m and (c) 5 mN/m.

We measured the average thickness of the molecular monolayer observed with AFM. On average the layer thickness ranges between 0.6 – 1 nm. An average height is similar for all LB films, which is clearly shown also on all cross-sections. In some cases we also observed the formation of the second layer on top of the first layer (see for instance Figure 10-13 for 5 mN/m and 15 mN/m). The average height of the second layer also ranges between 0.6 - 1 nm.

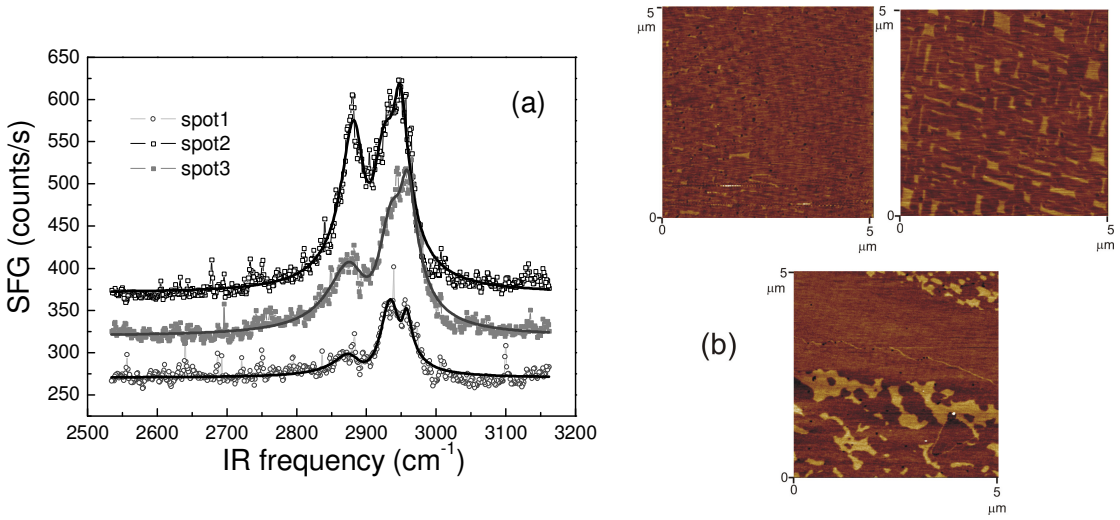

Figure 10-14: (a) SFG spectra recorded at different regions of the LB film prepared at surface pressure 15 mN/m. (b) AFM images of the same LB film obtained again at three different places on the mica surface. The corresponding tilt angles for these three spots are the following: 18°, 15° and 26°.

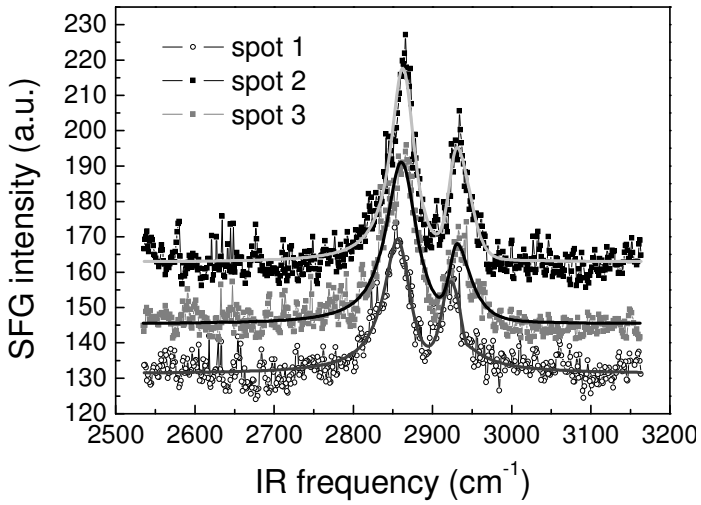

Figure 10-15: Spectra recorded at different regions of the Langmuir film prepared at surface pressure 25 mN/m. The corresponding tilt angles for these three spots are the following: 8°, 10° and 10°.

10.4 Discussion

In Langmuir films it can be noticed that the SFG intensity of vibrational peaks is increasing with increasing surface pressure. But on the other hand this is not true for LB films on the solid substrates (the variation in surface structures was drastically different on different parts of the LB film). The same observation can be obtained from AFM results where the monolayer coverage on the substrate hardly depends on the surface pressure.

	Langmuir (ssp)			Langmuir-Blodgett fused silica substrate (ssp)			Langmuir-Blodgett mica substrate (ssp)		
	5 mN/m	15 mN/m	25 mN/m	5 mN/m	15 mN/m	25 mN/m	5 mN/m	15 mN/m	25 mN/m
A_1	4	7	29	13	15	17	17	22	22
$\omega_1(cm^{-1})$	2851	2860	2855	2863	2870	2855	2855	2862	2861
$\Gamma_1(cm^{-1})$	10	15	14	25	23	27	28	32	26
A_2	1.9	9.8	6.7	3.4	17	6.6	4.3	20	13
$\omega_2(cm^{-1})$	2920	2925	2923	2925	2929	2936	2927	2928	2932
$\Gamma_2(cm^{-1})$	7	22	15	15	23	18	15	23	23
A_3	-7	-4	-15	-2.7	-27	-14	-91	-20	-20
$\omega_3(cm^{-1})$	2942	2938	2940	2955	2952	2951	2958	2955	2961
$\Gamma_3(cm^{-1})$	14	17	14	22	20	23	14	33	15

Table 10-1: Parameters giving the best fit to the SFG spectra of Langmuir and Langmuir-Blodgett films of HDA molecules from Figure 10-7 to Figure 10-11.

	Langmuir (ssp)			Langmuir-Blodgett fused silica substrate (ssp)			Langmuir-Blodgett mica substrate (ssp)		
	5 mN/m	15 mN/m	25 mN/m	5 mN/m	15 mN/m	25 mN/m	5 mN/m	15 mN/m	25 mN/m
$\Delta\nu$ (THz)	1.81	1.65	1.83	1.95	1.84	1.96	/	/	/
$\Gamma(ps^{-1})$	3.4	6.0	4.3	1.75	2.58	2.28	/	/	/

Table 10-2: Parameters giving the best fit to the FID-SFG signals of Langmuir and Langmuir-Blodgett films of HDA molecules from Figure 10-7 to Figure 10-10.

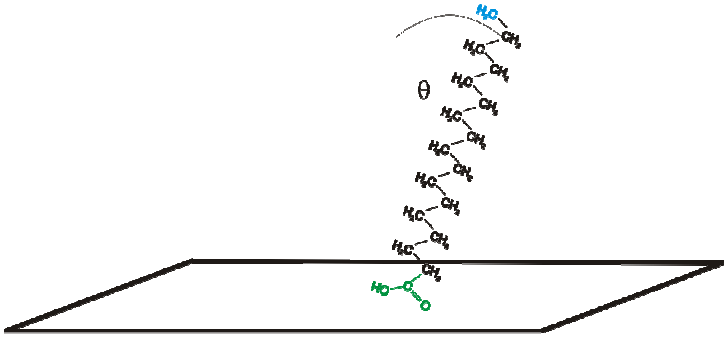

Figure 10-16: The orientation of HDA molecule on the surface. The tilt angle with respect to the surface normal is labeled by θ.

Regardless of this non-ideal formation of monolayers we will try to obtain some quantitative information on the orientation and distribution of HDA molecules in Langmuir and Langmuir-Blodgett films. The SFG spectra were fitted by describing the second order susceptibility as a set of Lorentzians, as was already described in Chapter 8. The parameters obtained from the SFG fitting are given in Table 10-1 and Table 10-2.
In order to determine the tilt angle of HDA molecule (see Figure 10-16) with respect to the surface normal we used the model developed by Wolfrum and Laubereau [92] for similar types of monolayers.

This model assumes azimuthally isotropic angular distribution which leads to the following dependence

$$\frac{A_{ssp,2875}}{A_{ssp,2958}} = -\left(\frac{\beta_{zzz,2875}}{2\beta_{zxx,2958}}\right)\left(\frac{(\gamma+1)\langle\cos\theta\rangle-(\gamma-1)\langle\cos^3\theta\rangle}{\langle\cos\theta\rangle-\langle\cos^3\theta\rangle}\right), \tag{54}$$

where A represent amplitudes of vibrational modes, β are molecular hyperpolarizabilities, $\gamma=\beta_{xxz}/\beta_{zzz}$ is the anisotropy which can be found in the literature for methanol [93] i.e. $\gamma=$ 1.66, and brackets $\langle\rangle$ denote averaging over polar angles θ. This is possible since the hyperpolarizabilities of hydrocarbons show that the group polarizabilities are transferable [94]. If the orientational distribution has a strong peak at a single tilt angle, the brackets $\langle\rangle$ in the expression (54) can be omitted. With this assumption one can determine the tilt angle of HDA molecules in a single film. For Langmuir films at 5 mN/m, 15 mN/m and 25 mN/m we obtained the chain tilt angles $\theta=$ 17°, 10°, and 10°±2° respectively. On the other hand the chain tilt angles for Langmuir-Blodgett films were higher giving 30°, 20°±5° and 10° for 5 mN/m, 15 mN/m and 25 mN/m, respectively.
The obtained dependence of tilt angles on surface pressure roughly corresponds to the expected orientation that HDA molecules possess at defined surface pressure (2D phase diagram in Figure 10-4). In the gaseous phase the distance between two neighboring molecules is the largest and thus the interactions between them are very small consequently the tilt angle is relatively large. By reducing the total area of the monolayer the molecules are approaching each other and therefore the hydrocarbon tails of HDA molecules begin to close pack with each other, so the tilt angle decreases. The phase transition from liquid-solid phase occurs at around 24 mN/m and above this pressure the monolayer of HDA molecules is in the condensed phase. The molecules are closely packed and are oriented with the hydrocarbon chain approximately pointing parallel with the surface normal thus giving the smallest value for the tilt angle for both types of films.
The last part of the investigaton of HDA films was focused on determination of the tilt angle from AFM images, in which the formation of a monolayer can be clearly seen. For the monolayer developed at all three surface pressure used for deposition the average measured thickness of the monolayer was in the range of 0.6 – 1 nm. By taking into account the lateral dimension of the hydrocarbon tail this corresponds to the tilt of the molecules between 60°-75°. The origin of the large discrepancy between the SFG and AFM analysis is still not resolved at the moment. Several scenarios are possible: the first is that the tip of the AFM somehow distorts the height of a monolayer due to a very soft interface and the second is that the SFG model used in our analysis is simply too simple and too general. It is most likely that the real values of the tilt angles lie somewhere between both limits and that the angular range is relatively broad.

10.5 Conclusions

We demonstrated that the combined SFG and AFM analysis of surface structures is a powerful tool to probe the quality of Langmuir and Langmuir-Blodgett films. Even

though one expects to obtain completely homogeneous monolayers of HDA molecules, the SFG spectra show just the opposite, especially in the case of LB films. The adsorbed films are very inhomogeneous, and so claiming that the molecules in a monolayer are well oriented with a well defined tilt angle is very presumptuous and could only be valid for very small areas, for instance 1 μm x 1 μm. Such small areas are very hard to probe by SFG experiments presented in this thesis.

Chapter 11

Summary and conclusions

In this chapter we summarize main achievements and conclusions of the dissertation.

Our results demonstrate that the SHG technique is an efficient tool to study the structural and switching properties of very thin films of the FLCP polymers. They revealed the V-shaped switching of the FLCP molecules. The SHG response originates mainly from the topmost surface layer of the FLCP, while the main part of the film is in a strongly pinned domain configuration. The FLCP in contact with hexadecane shows the domain like structure which resulted in a slower relaxation dynamics. The SHG results also point out that the polar order seems to respond with much slower dynamics compared to quadrupolar order which was confirmed by birefringence measurements.
The SHG results also indicate the layered structure of FLCP interface. The topmost layer is from the concept of proper operation of the ECS cell the most important but at the same time it is coupled to the underneath domain-like structure and thus influences its response. The understanding of the complete structure and its response to the external voltage is fundamental in order to tailor the properties of the ECS alignment layer for applications in the LCD industry.
In the thesis an extensive research on very thin films of organic molecules was presented. One such molecule is GMP nucleotide which can be a promising candidate for future applications in nanoelectronics, especially the formation of long G-wires with uniform height seems to be the most interesting. These wires are on average 1.9 nm high and can be up to several micrometers long. On the mica substrate these wires are aligned along the six directions of the nearest neighbours of the quasi-hexagonal basal mica plane. This preferential growth could be used to manufacture some specific nano-circuits used for applications.
The AFM results showed that the formation of the G-wires depends on the concentration of the solution and is observed in the range 0.005 wt% and 0.1 wt%. For smaller concentrations there is simply not enough material to initiate the wire growth, while at larger concentrations the terrace-like structures appear on the mica substrate. The process to form wire-like surface structures is practically independent of the type of cations present in solution for intermediate concentrations which is contrary to the self-assembly of GMP molecules for all three types of GMP derivatives in water solutions. We attribute this discrepancy to the specific surface structure of mica substrate where the K^+ ions stimulate the aggregation of GMP molecules.
The combination of both techniques, i.e. AFM and SFG provide an important complementary information on the surface structures, ordering, homogeneity, structural modifications, etc. More specifically we demonstrated that the resonant response of SFG in the range of C-H vibrations is very sensitive to structural ordering of adsorbed films.

This high sensitivity to structural modifications can serve as a perfect tool for investigation of GMPs, fatty acids or even some other molecules with similar properties.

Chapter 12

Extended abstract in Slovenian language

Povzetek disertacije v slovenskem jeziku

12.1 Uvod

Dandanes so tekoči kristali in biomateriali v povezavi z optiko in nanotehnologijo zelo obetavna in zanimiva znanstveno-raziskovalna področja. Primeri takih biomaterialov so zagotovo lipidi, proteini in materiali, povezani z DNK molekulo. Zanimivi s stališča znanosti sta predvsem njihovo obnašanje in mehanizem na površinah ter mejnih plasteh. Tako se na površinah izvrši mnogo bioloških procesov kot npr. samourejanje in adsorpcija proteinov, prepoznavanje celičnih receptorjev, itd. Kot primerne metode za proučevanje teh procesov lahko služijo nelinearne optične tehnike. Ob predpostavki, da poznamo procese, lahko nelinearne optične uporabimo pri detekciji specifičnih biomolekul v različnih biosenzoričnih arhitekturah.

V disertaciji sem predstavil optični eksperimentalni tehniki podvajanja (SHG) in seštevanja (SFG) frekvenc, ki sta bila postavljeni na Odseku za kompleksne snovi Instituta Jožef Stefan v Ljubljani, v Sloveniji. Glavni del disertacije je temeljil na postavitvi obeh eksperimentalnih tehnik, ki sta bili del večjega ultra hitrega titan-safirnega laserskega sistema podjetja Coherent iz Združenih držav Amerike. Prvi preizkus SHG eksperimenta je temeljil na meritvah urejevalnih slojev za tekočekristalne celice. Podobno so bile testne meritve s SFG metodo opravljene na tankih površinskih slojih biomolekul v stiku z različnimi trdnimi substrati. Z namenom določitve površinske topografije smo v kombinaciji z SFG metodo uporabili tudi mikroskop na atomsko silo (t.i. AFM).

12.2 Teoretično ozadje

Polarizacijo snovi lahko zapišemo v obliki linearnega in nelinearnega prispevka

$$\mathbf{P} = \mathbf{P}_l + \mathbf{P}_{nl}, \tag{55}$$

kjer linearni prispevek povezujemo z linearnimi optičnimi pojavi v snovi (sipanje, odboj, lom, itd). Nelinearni člen v enačbi (55) pa lahko razvijemo v vrsto kot

$$\mathbf{P}_{nl} = \mathbf{P}^{(2)} + \mathbf{P}^{(3)} + \mathbf{P}^{(4)} + \ldots \tag{56}$$

Glavna tema disertacije bodo nelinearni optični pojavi drugega reda, zato zapišimo le-ta člen kot funkcijo električnega polja **E**

$$\mathbf{P}^{(2)}(\omega) = \chi^{(2)}(\omega = \omega_1 \pm \omega_2) : \mathbf{E}(\omega_1)\mathbf{E}(\omega_2). \tag{57}$$

Ker iz tega člena izhaja več nelinearnih optičnih pojavov drugega reda, omenimo le najpomembnejša dva, to sta t.i. podvajanje frekvenc (angl. kratica SHG) in generacija vsote frekvenc (angl. kratica SFG). V prvem primeru velja, da ima elektromagnetno sevanje frekvenco 2ω, ki nastane v snovi kot posledica osvetlitve z močnim laserskim snopom s frekvenco ω. V drugem primeru pa v snovi nastane elektromagnetno sevanje s frekvenco enako seštevku frekvenc prvotnih dveh laserskih žarkov, in sicer $\omega = \omega_1 + \omega_2$. Za vse sode nelinearne optične pojave (drugega, četrtega reda,...) velja, da so dovoljeni oz. nastanejo v necentrosimetričnih materialih (materiali brez simetrije inverzije). To se da pokazati s pomočjo prostorske inverzije na izrazu (57)

$$\begin{aligned} -P_i^{(2)}(\omega) &= \chi_{ijk}^{(2)}(\omega = \omega_1 \pm \omega_2) : \left(-E_j(\omega_1)\right)\left(-E_k(\omega_2)\right) \\ &= (-1)^2 \chi_{ijk}^{(2)}(\omega = \omega_1 \pm \omega_2) : E_j(\omega_1) E_k(\omega_2) \\ &= P_i^{(2)}(\omega), \end{aligned} \tag{58}$$

kar pomeni, da so členi nelinearne polarizacije drugega reda pri taki operaciji lahko le 0. V skupino materialov s takšnimi simetrijskimi lastnostmi pa spadajo tudi površine in tanke mejne plasti, kjer je simetrija inverzije vedno porušena.

12.3 Eksperimentalna tehnika SHG

Eksperimentalna tehnika SHG je bila postavljena v sklopu komercialno dostopnega laserskega sistema Mira-RegA. Shema eksperimenta je predstavljena na sliki 12-1.

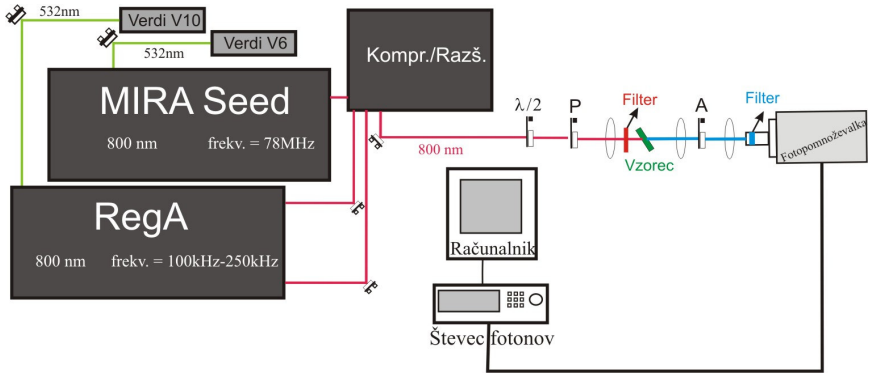

Slika 12-1: Shema SHG eksperimenta.

Mira je pulzni (frekvenca ponavljanja 78 MHz) titan-safirni laserski oscilator črpan z zveznim diodno črpanim laserskim snopom z valovno dolžino 532 nm, Laserski pulz iz oscilatorja najprej pošljemo v Kompr./Razš. enoto, nato pa spremenjen pulz od tam v RegA ojačevalnik, iz katerega dobimo ojačano pulzno lasersko svetlobo s frekvenco ponavljanja 100-250 kHz in energijo na pulz 3,6 – 6 μJ. Končni laserski izvor iz RegA ojačevalnika ima valovno dolžino nastavljivo med 790 – 810 nm in spektralno širino 26 nm. Za SHG meritve smo od celotne moči približno 1 W uporabili le 150-200 mW. Za detektor na vzorcu generiranega SHG signala pri valovni dolžini okoli 400 nm smo uporabili fotopomnoževalko (Electron Tubes iz Velike Britanije) model 9893/350B skupaj z števcem fotonov (Stanford research SR 440). Števec je obratoval v t.i. režimu vrat s časovno širino 5 ns, kar pomeni da so vrata detektorja odprta le 5 ns in sinhronizirana z RegA ojačevalnikom. Namen tako kratkih vrat detekcije je kar se da učinkovito zajemati izključno signal, ki ga dobimo od vzorca in se s tem izogniti signalu iz okolice.

12.4 SHG meritve na električno aktivnih površinah

Električno aktivne površine (ECS) so nov tip urejevalnih površin v tekočekristalnih zaslonih (LCD). Njihov koncept delovanja temelji na reorientaciji molekul urejevalne plasti pod vplivom električnega polja. Ta reorientacija mejnih molekul se potem preko elastičnih sil prenese na molekule tekočega kristala v neomejenem delu tekočekristalne celice. V običajnih LCD-jih elektrooptični efekt temelji na sklopitvi fizikalnih lastnosti tekočega kristala (kot npr. dielektrična anizotropija tekočega kristala, polarizacija) z električnim poljem. Tako se tekočekritalnih molekul v neomejenem delu vzorca reorientirajo povsod razen direktno ob površini, kjer pa je sidranje molekul tekočega kristala na mejno plast premočno. Tako v običajnih LCD-jih urejevalni sloj deluje kot zavora v procesu preklopa. Pri novem tipu urejevalnih slojev pa je drugače. Tu imamo tanek sloj feroelektričnega tekočega kristalnega polimera (FLCP) debeline 100 nm, ki se ob prisotnosti električnega polja reorientira, kar pa se potem prenese na molekule v neomejenem delu tekočega kristala.

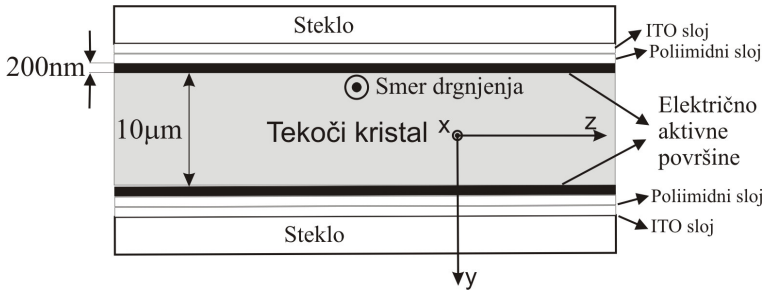

Slika 12-2: Geometrija tekočekristalne celice z električno aktivnimi površinami (FLCP sloji).

Z našimi SHG raziskavami smo poskušali določiti statične in dinamične lastnosti urejevalnega FLCP sloja debeline 200 nm (Slika 12-2). Opravili smo primerjalno študijo med prazno in tekočekristalno celico napolnjeno z izotropno tekočino heksadekan, obe pa

sta vsebovali urejevalni sloj molekul FLCP. Vse meritve so bile opravljene v transmisijski geometriji. Poleg tega smo proučevali tudi tekočekristalni fazni prehod iz SmC* v SmA* fazo.

Najprej smo izvedli meritve odziva SHG signala v FLCP plasti na zunanje električno polje v prazni celici in celici napolnjeni s heksadekanom pri sobni temperaturi. Na sliki 12-3 opazimo, da je odziv na zunanje električno polje pri prazni celici v pp polarizacijski kombinaciji (prvi znak je polarizacija laserskega izvora, drugi pa SHG signala) bipolaren s skoraj linearnim potekom. Na drugi strani pa odziv v sp polarizacijski kombinaciji precej odstopa od linearnega. V ostalih dveh polarizacijskih kombinacijah (ps in ss) skoraj ni bilo opaziti odziva na zunanje električno polje. Nato smo celico napolnili z izotropno tekočino heksadekan in ugotovili povečanje relativnega odziva v pp polarizacijski kombinaciji, pri čemer je ostal odziv v sp polarizacijski kombinaciji precej podoben prejšnjemu v prazni celici.
V naslednji fazi smo izmerili dinamični odziv tega sloja pri vklapljanju, izklapljanju in preklopu električnega polja iz 100 V na -100 V ter obratno.

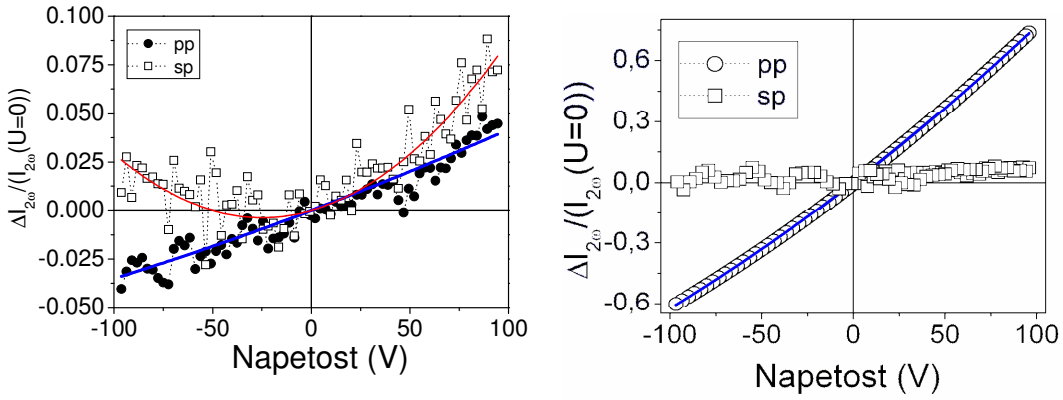

(a) (b)

Slika 12-3: Relativni SHG odziv (a) prazne in (b) tekoče-kristalne celice napolnjene s heksadekanom na zunanje električno polje.

Signal smo zajemali s časovno ločljivostjo 50 ms. Iz meritev preklopa v prazni celici lahko zaključimo le, da je odziv manjši od 50 ms, točne vrednosti pa ni mogoče določiti. Pri celici, napolnjeni s heksadekanom, pa je mogoče ugotoviti, da so preklopni časi precej daljši, $\tau = 0.5 \pm 0.12$ s (Slika 12-4 (a)). Zanimal nas je tudi relaksacijski proces FLCP sloja na izklop električnega polja od 100 V na 0 V in vklop le-tega od 0 V na 100 V. Tudi tu smo dobili relativno dolge relaksacijske čase $\tau_{odklop} = 1.31 \pm 0.11$ s and $\tau_{priklop} = 0.46 \pm 0.15$ s (Slika 12-4 (b)).

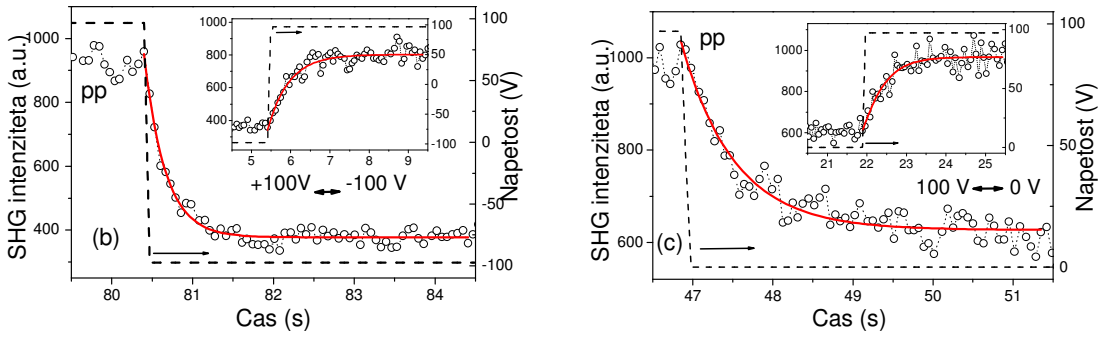

(a) (b)

Slika 12-4: SHG odziv prazne tekoče-kristalne celice s FLCP plastjo na zunanje električno polje v (a) pp in (b) sp polarizacijskih kombinacijah v transmisijski geometriji.

FLCP plast lahko pri spremembi zunanje temperature preide v več različnih ureditvenih faz.

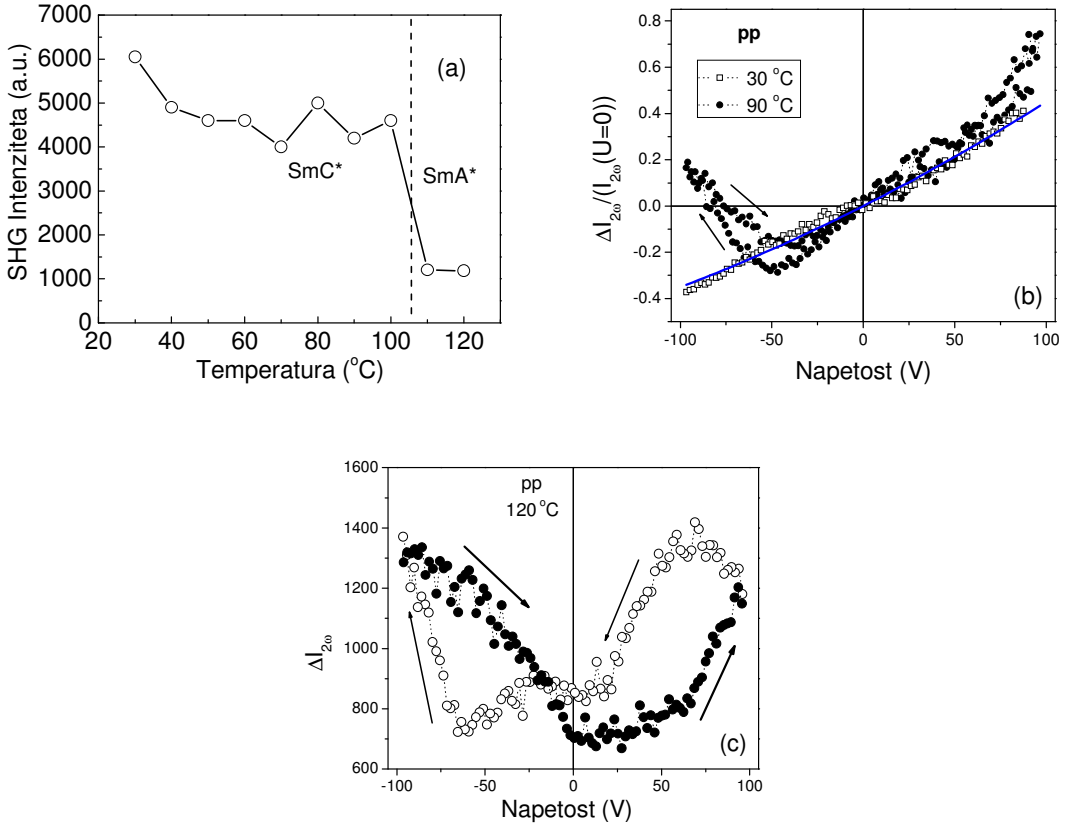

Slika 12-5: (a) SHG intenziteta ob odsotnosti električnega polja kot funkcija temperature tekočekristalne celice s FTKP urejevalnim slojem. (b) Relativni SHG odziv pri temperaturah 30° in 90°. (c) Histereza SHG odziva pri temperaturi 120°.

FLCP je pri sobni temperaturi v t.i. SmC* tekočekristalni fazi in z naraščanjem temperature preide pri 105°C v SmA* fazo, kar se lepo vidi tudi iz grafa odvisnosti SHG

signala od temperature (Slika 12-5 (a)), kjer ob faznem prehodu pride do nenadnega upada v SHG intenziteti. Tudi odziv na električno polje pri različnih temperaturah nakazuje na fazni iz SmC* – SmA* tekočekristalno fazo. Signal se namreč iz bipolarnega spremeni v unipolarni, poleg tega pa je v relativnem SHG signalu prisotna čedalje večja histereza (odziv pri večanju napetosti je drugačen kot odziv pri zmanjševanju).
Naši rezultati so pokazali, da je SHG tehnika učinkovita metoda za raziskovanje strukturnih in dinamičnih lastnosti FLCP urejevalnih slojev za tekočekristalne zaslone. V splošnem smo iz SHG odziva ugotovili t.i. karakteristično V-odzivno obliko FLCP molekul na zunanje električno polje. Prepričani smo tudi, da SHG odziv prihaja predvsem iz vrhnjih delov FLCP sloja in da ima glavni del filma t.i. domensko strukturo. Naše meritve polarnega odziva nakazujejo na zelo počasne odzivne čase v primerjavi z kvadrupolnimi odzivi, dobljenimi z meritvami dvolomnosti.
Vsi rezultati nakazujejo na večplastno zgradba urejevalnega sloja, in sicer (a) vrhnji sloj, ki se precej hitro odziva na zunanje polje (~10 ms) (b) vmesna debelejša plast z domensko strukturo in odzivnim časom blizu 1 s ter (c) statična plast ob substratu stekla, ki prispeva največ k SHG signalu in se ne odziva na zunanje električno polje. Ta plastovitost s stališča pravilnega in zadostnega delovanja takega urejevalnega sloja niti ne predstavlja velike ovire, saj je najvišja plast tista, ki je pomembna in se odziva z relativno kratkim odzivnim časom. Je pa res, da je ravno natančno poznavanje celotne strukture bistveno pri nadaljnjih korakih k razvoju in uveljavitvi FLCP urejevalnih plasti v industriji tekočekristalnih zaslonov.

12.5 Mikroskop na atomsko silo

Mikroskop na atomsko silo (bolj poznan v obliki angl. kratice AFM) spada v malo širšo skupino metod, kjer se ostro konico uporablja za proučevanje površinskih struktur na nivoju molekul in ob prisotnosti specifičnih pogojev tudi na atomskem nivoju. Mikroskop na atomsko silo lahko uporabljamo v več različnih načinih delovanja: (a) t.i. tipalni način, kjer preko tipanja površine s konico (amplitude velikosti od 20-200 nm) pridobimo informacijo o topografiji preiskovane površine. (b) Kontaktni način, ki deluje na principu stalnega kontakta konice s tankim tekočinskim slojem na vzorcu. Topografijo vzorca tako dobimo na podlagi vertikalnih premikov konice, ko prepotuje celotno območje zajemanja. (c) Zadnji je nekontaktni način, kjer konica ves čas niha z frekvenco, ki je malce višja od resonančne in amplitudo manjšo od 10 nm. Informacijo o topografijo dobimo preko vertikalnega odmika čitalnika v posamezni točki preiskovane površine.

12.6 Površinske strukture molekul gvanozin 5´-monofosfata

Dandanes je proizvodnja površinskih struktur preko procesa samourejanja eden izmed glavnih izzivov aplikativnih znanosti s področja molekularne elektronike. Med primerne kandidate štejemo tudi molekula gvanozina oz. njeni derivati. V tem delu disertacije se bomo osredotočili na molekulo gvanozin 5´-monofosfata (GMP), ki je RNK nukleotid sestavljen iz nukleinske baze gvanina, sladkorja riboze in fosfatne skupine. Molekula GMP je edinstvena med vsemi nukleotidi po svoji specifični lastnosti povezovanja v večje supermolekularne skupke v vodnih raztopinah. To ji omogočajo

samokomplementarni deli za tvorbo vodikovih vezi, zaradi česar tvori t.i. kvartete, ki se v nadaljnjem procesu samourejanja preko kationov povežejo v vijačne strukture t.i. G-žičke s prečno dimenzijo okoli 2,5 nm. Njihova dolžina pa je odvisna od velikega števila zunanjih parametrov, kot so npr. tip kationov, pH, temperatura in koncentracija raztopine. V doktorski disertaciji sem skušal predstaviti predvsem urejanje GMP molekul na površinah. Podobno kot v vodnem okolju smo skušali ugotoviti vrednosti kritičnih parametrov za dosego željenih površinskih struktur. Glavni poudarek je bil na masni koncentraciji raztopine, iz katere smo nanesli GMP molekule na različne tipe substratov (SiO_x, zlato, na sveže odlomljen substrat sljude $K_2O{\cdot}Al_2O_3{\cdot}SiO_2$). Osredotočili smo se tudi na vpliv različnih tipov kationov (NH_4, K in Na) prisotnih v GMP soli na tvorbo skupkov ob površini substrata.

Najprej smo izbrani material raztopili v čisti destilirani vodi pri masni koncentraciji 20% in nato pa to raztopino redčili do izbrane koncentracije. Za nanos materiala iz raztopine smo uporabili več različnih pristopov. Najprej smo uporabili t.i. metodo kapljičnega nanosa na substrat sljude pri koncentracijah, ki so v raztopinskem okolju znane kot kritične koncentracije za tvorbo skupkov (masna koncentracija c > 10%). Rezultati AFM analize so pokazali, da so bili nastali skupki na površini precej nepravilnih dimenzij, poleg tega pa je njihova višina precej odstopala od znanih dimenzij v raztopini, in sicer je znašala okoli 100 nm. Zaradi neuspelih poizkusov, da bi na površini opazili žičke oz. homogene strukture enovitih dimenzij, smo se lotili nanosa na površino s pomočjo potapljanja substrata. Prav tako smo koncentracijo raztopine, iz katere smo nanašali molekule, zmanjšali na 0,004 – 0,2 %. Nanos na substrat s potapljanjem je trajal 3 minute, nato pa je sledilo 6–9 h sušenje vzorca pri sobnih pogojih. Tako smo v območju koncentracij c ≤ 0,01% opazili majhne otočkom podobne skupke, in velike, zaplatam podobne strukture, z majhno višino (h < 1 nm). Prvi bi lahko bili skupki soli, drugi pa enoslojne plasti GMP molekul.

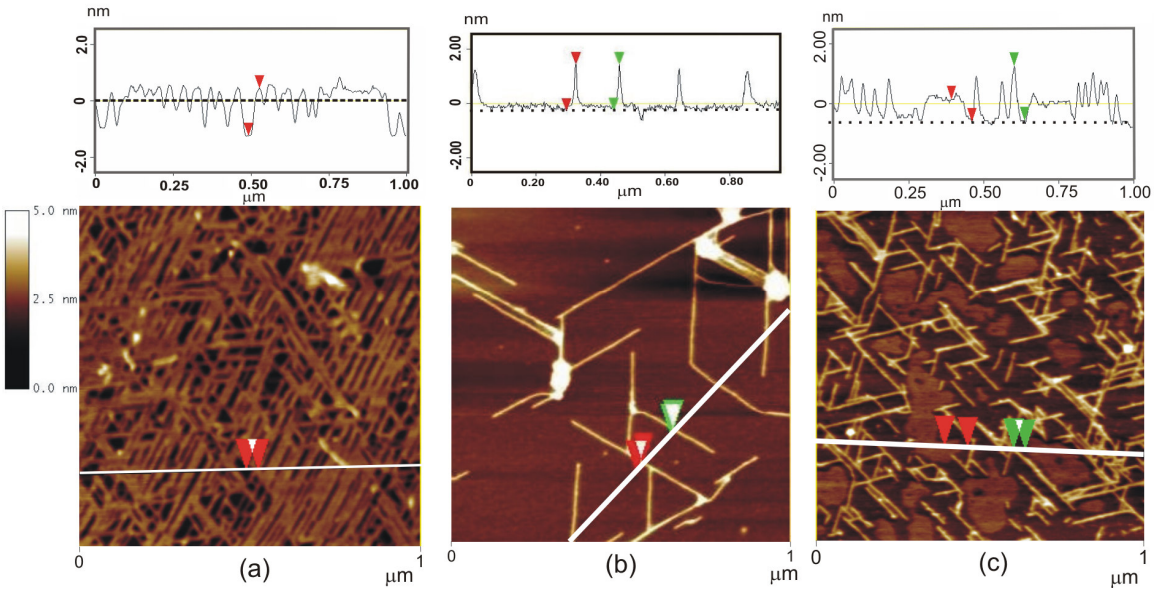

Slika 12-6: AFM slike velikosti 1 µm x 1 µm različnih tipov GMP molekul: (a) KGMP nanešene pri masni koncentraciji 0,02%; (b) Strukture iz NaGMP, nanešene pri 0,01% in (c) Strukture iz NH_4GMP nanešene pri masni koncentraciji 0,01%.

Pri masnih koncentracijah med 0,01% ≤ c ≤ 0,02% smo opazili žičkam podobne tvorbe. Opazili smo tudi, da se te žičke povezujejo v mreže, kar velja za vse tri tipe GMP soli (tako NH_4, K kot tudi Na). AFM slike za vse tri tipe na sljudi prikazuje slika 12-6.
Povprečna višina posamezne žičke na sliki 12-6 je 1,5 – 2,2 nm, kar jasno prikazuje tudi statistična analiza na sliki 12-7 (a). Zakaj pride do odstopanja v velikosti, če primerjamo nanešene strukture z dimenzijo G-kvartetov v raztopini, še ni povsem jasno. Je pa za takšno razliko lahko odgovornih več mehanizmov: (a) interakcija med žičko in substratom sljude lahko privede do zmanjšanja premera žičke; (b možno je, da žička na substratu sljude ni sestavljena iz G-kvartetov, temveč je sestavljena iz monomernih ali celo dimernih enot GMP, še posebej pri strukturah z višino manjšo od 1,7 nm; (c) pritisk AFM konice lahko privede do zmanjšanja višine posamezne žičke.
Že na podlagi AFM rezultatov na sliki 12-6 je možno opaziti, da so nastale žičke na površini sljude preferenčno orientirane v določene smeri, ki so ena glede na drugo zavrtene za kot 60°. To dokazuje tudi statistična analiza orientacij teh žičk, opravljena na različnih vzorcih (Slika 12-7 (b)).

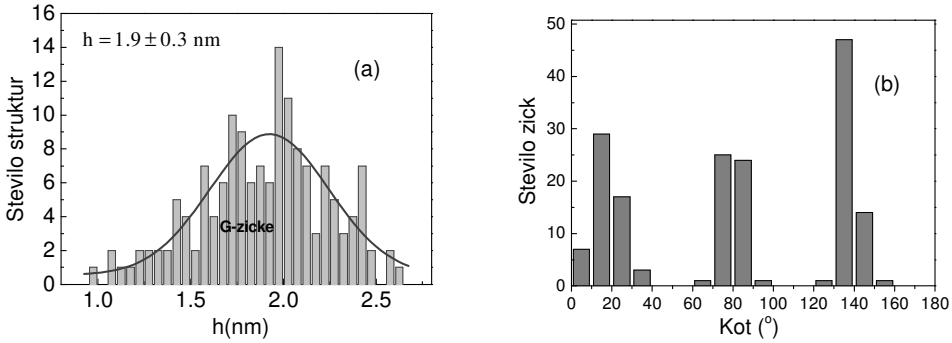

Slika 12-7: (a) Višinska statistika struktur opaženih na substratu sljude za različne vzorce. (b) Porazdelitev orientacij žičk na substratu sljude.

Zanimivo vprašanje, zakaj pride do te specifične orientacije G-žičk. Odgovor se skriva v sami površinski strukturi sljude, in sicer se v zgornjem sloju substrata sljude nahajajo kalijevi ioni, ki tvorijo t.i. heksagonalno mrežo. Sljuda je namreč sestavljena iz več plasti t.i. filosilikatov (Slika 12-8).

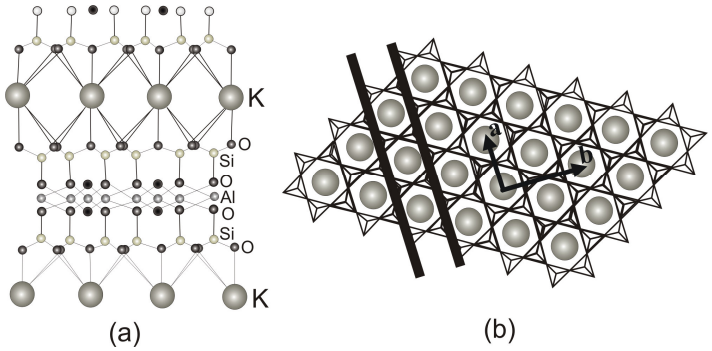

Slika 12-8: (a) Prerez preko filosilikatnih plasti in (b) prerez preko heksagonalne mreže kalijevih ionov med dvema filosilikatnima plastema.

Med dvema takima plastema filosilikatov ležijo kalijevi ioni, ki ponavadi pri t.i. »cepljenju« sljude ostanejo na površju in tako tvorijo heksagonalno površinsko strukturo, kot jo prikazuje slika 12-8 (b).
Zanimalo nas je tudi, v kateri smeri glede na glavni osi (**a** ali **b**) heksagonalne mreže kalijevih ionov ležijo G-žičke na sljudi (Slika 12-8 (b)). S tem namenom smo posneli AFM sliko na skali 10 nm x 10 nm in tako ugotovili, da se žičke orientirajo v smeri osi a = 0,52 nm oz. v smeri najbližjih sosedov kalijevih ionov. Poleg tega imamo še dodatni dokaz za ureditev G-žičk po najbližjih sosedih kalijevih kationov. In sicer se dvakratnik razdalje med dvema sosednjima kalijevima ionoma na površini sljude (2 x **a** = 1,04 nm) zelo dobro ujema s trikratnikom razdalje med dvema kvartetoma (3 x 0.34 nm = 1,02 nm), kar je ravno perioda G-žičke. Meritve v raztopinah so namreč pokazale, da je razmik med dvema sosednjima G-kvartetoma v G-žički približno 0,34 nm.

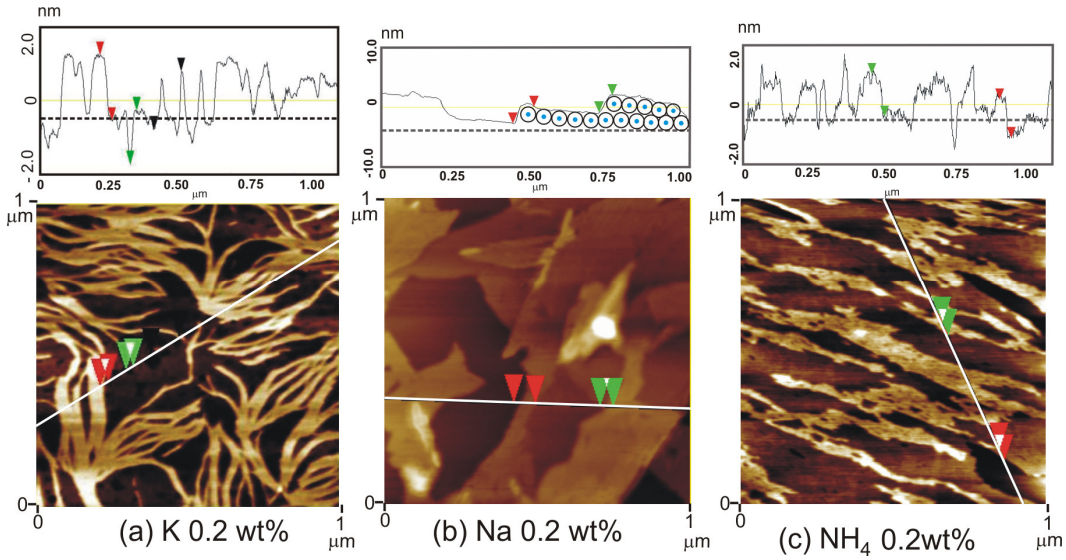

Slika 12-9: AFM slike različnih tipov GMP molekul na substratu sljude pri masni koncentraciji 0,2%.

Pri masnih koncentracijah, ki so bile večje od 0,2 % smo na substratu sljude opazili terasam podobne površinske tvorbe (Slika 12-9). Višina le-teh se precej bolje ujema s prečno dimenzijo G-žičk v vodnih raztopinah, ki je 2,2 – 2,8 nm. Na prerezu na sliki 12-9 (b) smo tako upodobili model urejanja G-žičke v teh terasam podobnih strukturah.
AFM rezultati na tankih površinah GMP molekul na sljudi in drugih substratih so pokazali, da so te molekule ena izmed potencialnih kandidatk pri izdelavi elektronskih naprav na nanoskali. Ima namreč sposobnost tvorbe dolgih G-žičk z določeno prečno dimenzijo (~1.9 nm). Prišli smo do zaključka, da je podobno kot pri raztopinski dinamiki, tudi ob površinah njena sposobnost tvorbe določenih struktur precej odvisna od masne koncentracije nanosov. Pri zelo nizkih koncentracijah ($c \leq 0{,}005\%$) je preprosto premalo molekul v raztopini, da bi se tvorba žičk sploh pričela, pri previsokih koncentracijah pa je materiala preveč, zato pride do tvorbe velikih konglomeratov molekul gvanozina. Najbolj primerne masne koncentracije za tvorbo žičkam podobnih struktur so med obema skrajnostma, to je 0,01 % - 0,2 %. Kljub temu pa se mehanizem urejanja ob površinah v nečem razlikuje od tistega v raztopini, in sicer je ob površinah tvorba G-žičk skoraj

popolnoma neodvisna od tipa GMP soli, ki smo jih uporabili pri nanosu na površino. Razlog za to je ponovno v specifični strukturi površine sljude, ki v večji meri kot tip GMP soli stimulira nastanek žičkam podobnih struktur.

12.7 Eksperimentalna tehnika SFG

V splošnem obstajata dva tipa eksperimentalne postavitve SFG tehnike, in sicer t.i. spektroskopska SFG tehnika (Slika 12-10) in časovna FID-SFG tehnika (enaka shema brez etalona in namesto CCD detektorja uporabimo fotopomnoževalko). Pri prvi se spektralno ozek (oz. časovno dolg, to je nekaj ps) vidni laserski pulz v času in kraju ujame s spektralno širokim (časovno kratkim, to je 60 fs). Pri tem načinu SFG tehnike lahko proučujemo vibracije določenih molekulskih vezi oz. molekulskih skupin.

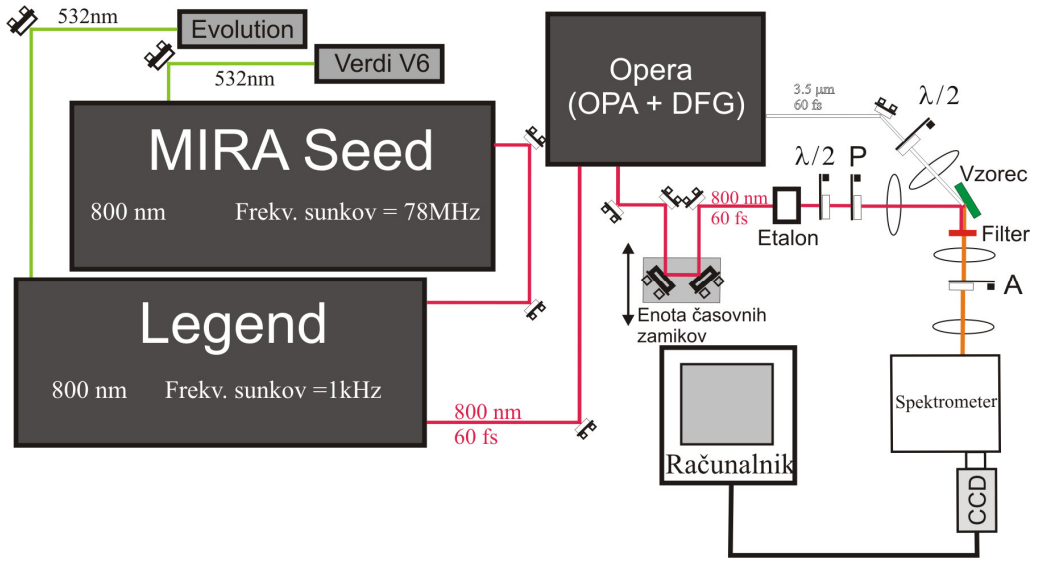

Slika 12-10: (a) Shema spektroskopske SFG tehnike.

Za razliko od SHG tehnike smo za SFG uporabili komercialno dostopni (Coherent, ZDA) pulzni titan-safirni laser t.i. Legend, ki deluje pri frekvenci ponavljanja 1 kHz in 2,5 mJ energije na pulz. Del te laserske svetlobe se porabi za tvorbo infrardeče laserske svetlobe z valovno dolžino med 1,1-10 µm v Opera enoti (Coherent), približno 0,5 mJ pa smo uporabili za vidni del SFG eksperimenta. Pri SFG spektroskopiji smo kot detektor SFG signala uporabili spektrometer (Acton SP-2300 z motoriziranim modulom treh uklonskih mrežic) in CCD kamero (Princeton Instruments). V primeru časovno ločljive SFG tehnike pa je bila tako kot pri SHG eksperimentalni metodi uporabljena fotopomnoževalka (Electron tubes), model 9863/350B s števcem fotonov (Stanford Research). Fotopomnoževalka se od modela, uporabljenega pri SHG meritvah (9893/350B), razlikuje v večji občutljivosti na svetlobo z valovno dolžino okoli 650 nm, ki pa je ravno valovna dolžina SFG signala. Oba detekcijska sistema za SFG meritve sta, podobno kot pri SHG eksperimentu, delovala v t.i. režimu »vrat«, ki so bila časovno usklajena s prihodom laserskih sunkov do detektorja.

12.8 SFG meritve na tankih površinah molekul Gvanozin 5´-monofosfata

GMP molekula tvori na sljudi celo paleto različnih površinskih topografij. Tvorba posameznega tipa struktur je odvisna predvsem od masne koncentracije raztopine, iz katere molekule nanašamo. V nadaljevanju bodo predstavljeni izsledki raziskave površinskih struktur GMP molekul na substratu sljude in zlata, ki so bili dobljeni s pomočjo AFM in SFG eksperimentalnih metod.
Priprava vzorcev površinskih struktur GMP molekul na površini sljude je potekala na način, opisan v podpoglavju 12.6. Nanašanje GMP molekul na substrat sljude je potekalo z uporabo t.i. tehnike s potapljanjem, na substrat zlata pa smo zaradi njegove hidrofobnosti uporabili tehniko kapljičnega nanosa z volumnom kapljice 15 μl. Vzorce smo nato sušili pri sobnih pogojih 6-9 h. Pripravi je sledila natančna preiskava vzorcev pod mikroskopom na atomsko silo, ki je deloval v tipalnem načinu. Nato smo na vzorcih GMP molekul opravili tudi SFG meritve pri različnih polarizacijskih kombinacijah (ppp, ssp, pss in sps, kjer prvi znak predstavlja polarizacijo nastale SFG svetlobe, drugi vpadne vidne in tretji vpadne infrardeče laserske svetlobe) v območju C-H vibracij, in sicer med 2800 – 3100 cm^{-1}. Pri tem smo bili pozorni na to, da so bile SFG meritve opravljene približno na enakih delih, kot so bile predhodno opravljene meritve pod AFM. To je pomembno zaradi primerjave topografije, ki je lahko na različnih delih zaradi koncentracijskega gradienta, ki nastane med sušenjem vzorca, precej drugačna.
Rezultati spektroskopije s SFG metodo kažejo na prisotnost dveh C-H vibracijskih vrhov, in sicer enega pri 2900 cm^{-1} (simetrično raztezanje CH_2 vezi) in drugega pri 2950 cm^{-1} (asimetrično raztezanje CH_2 vezi). Ta CH_2 skupina se namreč nahaja na repu sladkorja riboze. To velja tako za SFG rezultate na substratu sljude kot tudi na zlatu. Razlika je le v večjem neresonančnem ozadju iz površine zlata v primerjavi s tistim iz površini sljude. Primeri SFG spektrov, pomerjeni pri treh različnih masnih koncentracijah in pri dveh polarizacijskih kombinacijah (ppp in ssp) za Na-GMP in NH_4-GMP soli na substratu sljude, so prikazani na sliki 12-11. Topografija nastalih površinskih struktur je prikazana na AFM slikah na sliki 12-12 in sliki 12-13. Tako na podlagi AFM rezultatov, kot tudi SFG spektrov, je moč ugotoviti, da je površinska struktura GMP molekul na sljudi v precejšnji meri odvisna od masne koncentracije raztopine uporabljene pri nanosih. Pri najnižjih koncentracijah (c ~ 0,02 %) lahko opazimo žičkasto površinsko strukturo, pri srednjih koncentracijah (c ~ 0,2 %) terasam podobno strukturo in pri najvišjih koncentracijah (c ~ 2 %) popolnoma neurejeno ter gosto površinsko strukturo.
Kljub temu, da AFM slike ne kažejo kakšnih posebnih razlik med posameznim tipom GMP molekul, pa SFG rezultati kažejo ravno nasprotno. Pri nizki in srednji masni koncentraciji se SFG signal za posamezni tip GMP soli ne razlikuje veliko, opazimo lahko prisotnost dveh vibracijskih vrhov, ki sta posledica prej navedenih CH_2 vibracij.

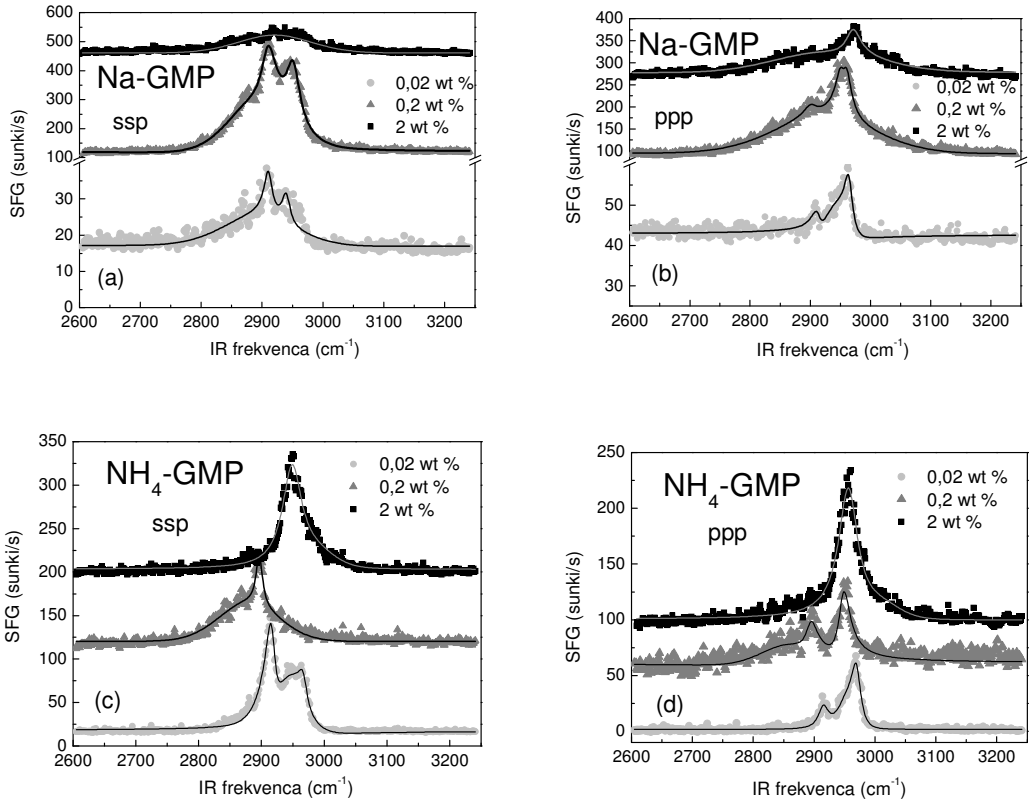

Slika 12-11: SFG spektri Na in NH_4-GMP molekul nanešenih na površino sljude pri treh različnih koncentracijah za ssp (a in c) in ppp (b in d) polarizacijski kombinaciji. Zaradi lažje primerjave SFG intenzitet smo posamezni spekter vertikalno premaknili.

Pri visokih koncentracijah je SFG odziv Na-GMP drugačen kot pri NH_4-GMP. Tako pri NH_4-GMP opazimo en resonančni vrh okoli 2950 cm^{-1}, pri Na-GMP pa resonančni odziv izgine oz. ostane le šibak neresonančni odziv od samega substrata sljude.

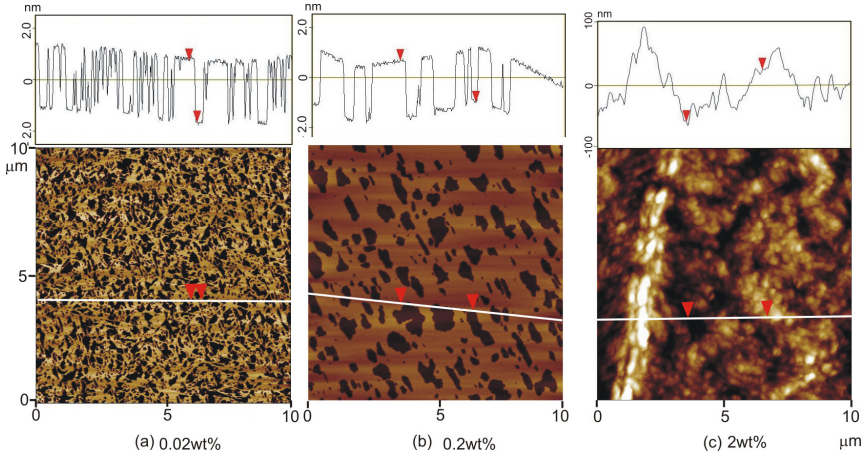

Slika 12-12: AFM rezultati površine Na-GMP molekul na substratu sljude pri različnih masnih koncentracijah: (a) 0,02; (b) 0,2 in (c) 2.0 wt%.

Tako obnašanje nakazuje na to, da signal pri visokih koncentracijah ne prihaja več s površine, ampak iz neomejenega dela vzorca. Da bi dokazali, da je izvor SFG signala v notranjosti vzorca, smo na površino NH_4-GMP kanili izotropno tekočino heksan. Po tem postopku je kljub spremenjenemu površinskemu sloju, ostal signal skoraj nespremenjen, kar potrjuje, da je mesto izvora signala v neomejenem delu vzorca.
Poleg tega smo pri NH_4-GMP vzorcih pri visokih koncentracijah opazili tudi, da je resonančni vrh pri 2950 cm^{-1} viden tudi v prepovedanih polarizacijskih kombinacijah. To je dodaten dokaz, da signal prihaja iz neomejenega dela vzorca, ki ima urejeno strukturo s porušeno centrosimetrijo. Iz AFM na sliki 12-13 (c) je moč sklepati celo na prisotnost vijačne strukture, ki lahko povzroči kiralni odziv nelinearne optične susceptibilnosti drugega reda.

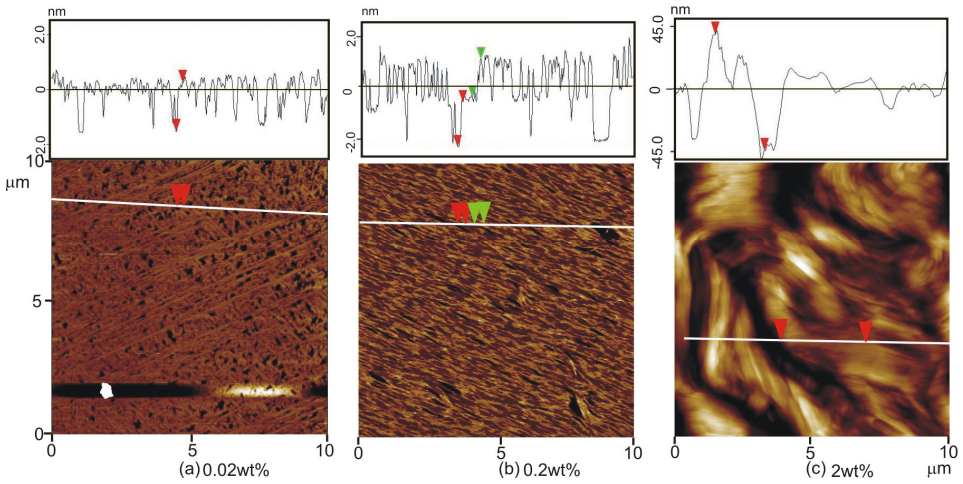

Slika 12-13: AFM rezultati površine NH_4-GMP molekul na substratu sljude pri različnih masnih koncentracijah: (a) 0,02; (b) 0,2 in (c) 2.0 wt%.

S pomočjo raziskovalnih tehnik AFM in SFG smo pridobili informacijo o samourejanju GMP molekul na trdnih površinah. Ugotovili smo, da je resonančni odziv v območju C-H vibracij močno občutljiv na vsako strukturno spremembo adsorbiranega sloja GMP molekul, zaradi česar je SFG metoda še posebej primerna za proučevanje GMP in njej podobnih molekul.

12.9 Površinske strukture monoslojev Heptadekanojske kisline

Za pripravo tankih plasti organskih molekul t.i. monosloje organskih molekul na vodni površini in površini trdnega substrata smo uporabili Langmuir in Langmuir-Blodgett tehniki. Ti dve metodi manipulacije s tankimi filmi površinskih molekul sta izpopolnila Irwing Langmuirja in Katherine Blodgett. Glavna razlika med metodama je, da se z Langmuir tehniko pripravlja tanke sloje organskih molekul na tekočinah, z Langmuir-Blodgett tehniko pa se tak monosloj iz površine tekočine prenese na trden substrat.
Podobno kot pri 3D materialih tudi 2D površinske strukture tvorijo različne faze, ki jih analogno imenujemo: plinasta, tekoča in trdna (Slika 12-14 (a)). Te faze se med seboj razlikujejo po stopnji urejenosti molekul v 2D sloju. Tako je najbolj neurejena faza

plinasta, pri kateri so molekule dovolj narazen ena glede na drugo, da se lahko prosto gibljejo po površini.

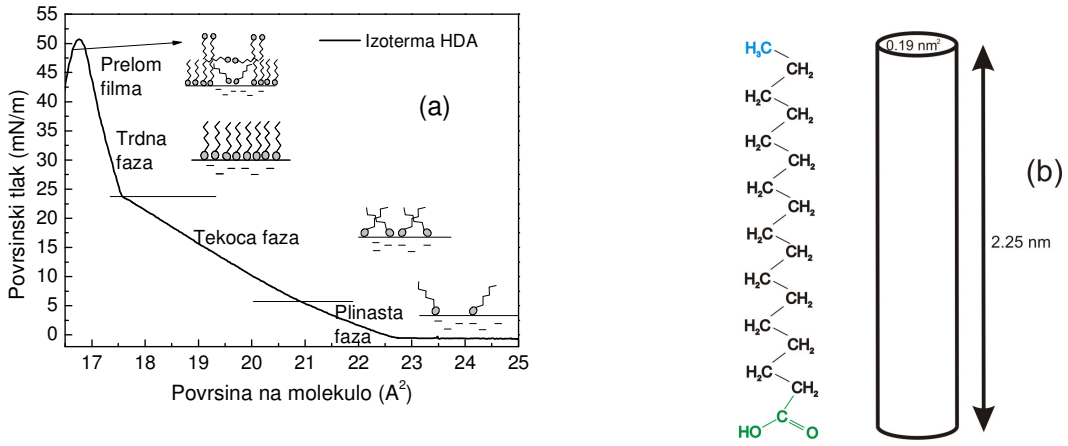

Slika 12-14: (a) Izoterma molekule heptadekanojske kisline z nazorno ponazoritvijo vseh treh faznih stanj. (b) Kemijska formula HDA molekule in shema njene cilindrične oblike z dolžino 2,25 nm in površino 0,19 nm^2.

Slednje do neke mere velja tudi za tekočinsko fazo s to razliko, da prihaja do močnejših medmolekularnih interakcij kot v plinasti fazi. V trdni fazi so molekule tesno ena ob drugi in preferenčno orientirane v določeno smer.

Molekule z lastnostjo tvorbe monoslojev na tekočini (vodi) imenujemo površinsko aktivne oz. amfifilne. Poznamo več skupin takih molekul, kot npr. fosfolipidi in maščobne kisline. Slednje so sestavljene iz dveh delov, in sicer hidrofilne karboksilne skupine (skupina COOH) in hidrofobnega repka (ogljikovodikova veriga iz CH_2 in CH_3 skupin). Maščobne kisline predstavimo s splošno kemijsko formulo $C_nH_{2n+1}COOH$.

Opravili smo podrobno študijo obnašanja molekul heptadekanojske kisline (HDA) pri različnih parametrih, kot sta tip površine in površinska napetost monosloja. HDA molekula spada med maščobne kisline in ima kemijsko formulo $C_{16}H_{33}COOH$. Do faznega prehod med plinasto in tekočo fazo HDA molekul pride pri površinskem tlaku okoli 5 mN/m, med tekočo in trdno pa pri okoli 24 mN/m. Nadaljnje naraščanje površinskega tlaka povzroči prelom filma pri 50 mN/m. Do preloma filma pride zaradi prevelikih medsebojnih sil, ki povzročijo izrivanje molekul iz monosloja (shema na sliki 12-14 (a)).

Langmuir in Langmuir-Blodgett filme smo pripravili s pomočjo komercialno dostopnega korita podjetja Nima technology iz Velike Britanije. Model korita je bil 112D z delovno površino 85 cm^2. Poleg korita sta za pripravo filmov potrebna tudi pomakalni sistem in senzor površinskega tlaka. Pomembni del korita sta dve motorizirani zapornici za uravnavanje površinskega tlaka. Celotni sistem kontroliramo z računalnikom. Pred pripravo filmov je korito potrebno najprej očistiti, umeriti merilni sistem površinskega tlaka in nato opraviti testno meritev, pri kateri se površinski tlak vodne površine ne sme bistveno spremeniti (± 0,5 mN/m) med stiskanjem in razpenjanjem. Na ta način preverimo čistost vode in njene površine.

Molekule heptadekanojske kisline smo naročili pri podjetju Sigma Aldrich (98 % čistost), jih raztopili v kloroformu in pripravili raztopino z masno koncentracijo 0,5 mg/ml. 30 µl

raztopine smo nato nanesli na vodno površino in pustili 30 minut mirovati pri sobni temperaturi 22-23°C. Po polurnem mirovanju smo film stisnili do predvidenega tlaka (5, 15 in 25 mN/m) in počakali še približno 40 minut, da se je tvoril homogen Langmuir film. Na tako formiranem filmu smo nato izvajali SFG meritve oz. le-tega prenesli na trden substrat, to je na sveže odlomljenem substrat sljude ali substrat kvarčnega stekla. Slednjega je bilo potrebno najprej očistiti tako, da smo ga za 10 minut potopili v t.i. piranja raztopino (raztopina v razmerju 1:3 H_2O_2:H_2SO_4).
SFG meritve smo izvajali pri različnih polarizacijskih kombinacijah dobljenega SFG ter vpadnih dveh, vidnega in infrardečega žarka (ssp, ppp, sps in pss). Iz literature lahko razberemo, da ima HDA molekula v območju C-H vibracijc (to je med 2800 cm^{-1} – 3100 cm^{-1}) tri resonančne vrhove, in sicer simetrično raztezanje CH_3 skupine (2875 cm^{-1}), simetrično upogibanje CH_3 skupine povečano zaradi Fermijeve resonance (2935 cm^{-1}) in asimetrično raztezanje CH_3 skupine (2958 cm^{-1}). Na SFG spektrih na sliki 12-15 in sliki 12-16 spodaj v glavnem opazimo le prva dva vrhova, tretji pa je zelo šibak oz. ima lahko negativno amplitudo. Na prisotnost dveh nas opozarjajo tudi meritve FID-SFG signala. Pri slednjih namreč merimo razpad nelinearne polarizacije, ki se v monosloju inducira zaradi visokih moči vpadnega vidnega in infrardečega žarka. Te meritve izvajamo tako, da vidni žarek časovno zakasnjujemo glede na infrardečega.

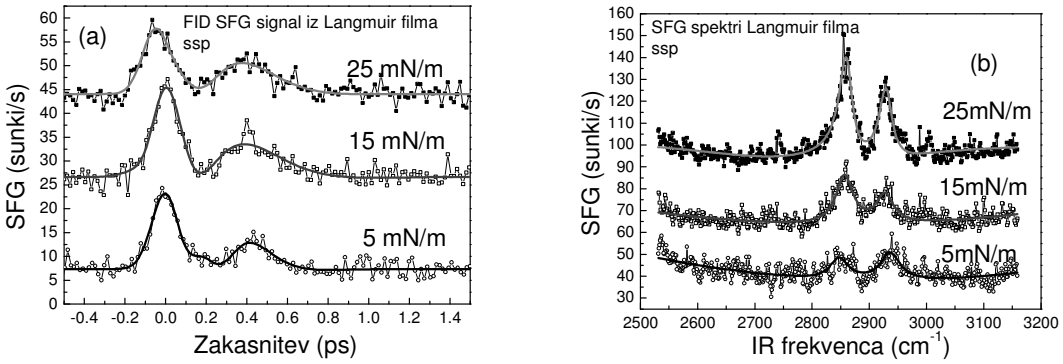

Slika 12-15: (a) FID-SFG signali in (b) SFG spektri Langmuir filma na vodni površini pomerjeni v ssp polarizacijski kombinaciji.

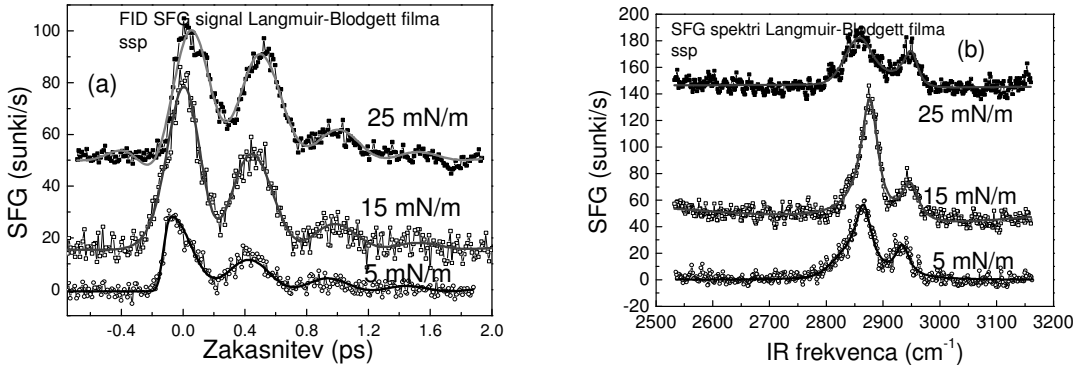

Slika 12-16: (a) FID-SFG signali in (b) SFG spektri Langmuir-Blodgett filma pripravljeni na kvarčnem steklu in pomerjeni v ssp polarizacijski kombinaciji.

V FID-SFG signalu tako vidimo dušeno utripanje resonančnih dveh vrhov opaženih v SFG spektrih. Frekvenca utripanja $\Delta\nu$ = 1,95 THz se lepo ujema z razliko frekvenc obeh resonančnih vrhov, to je približno $\Delta\nu = 70\ cm^{-1} = 2{,}11$ THz.
Iz SFG rezultatov lahko ugotovimo še nekaj, in sicer, da je v primeru Langmuirjevih filmov intenziteta SFG signala odvisna od tlaka in s tem povezana z urejenostjo filma. Največjo intenziteto dobimo pri najbolj urejenem filmu, to je pri površinskem tlaku 25 mN/m, pri katerem je monosloj HDA molekul v trdni fazi. Pri Langmuir-Blodgett filmih pa ni neke očitne korelacije med SFG intenziteto in površinskim tlakom, pri katerem je bil film prenesen iz vodne površine na substrat. Odgovor na vprašanje, zakaj je tako le pri LB filmih, smo dobili z nadaljno analizo vzorcev pod AFM mikroskopom in posnetimi spektri istega filma na več različnih območjih. Struktura se je znotraj različnih delov vzorca precej spreminjala, kar pomeni, da prihaja med prenosom filma iz vodne površine na trden substrat do določenih sprememb, ki povzročijo nehomogenosti na LB filmih (Slika 12-17).

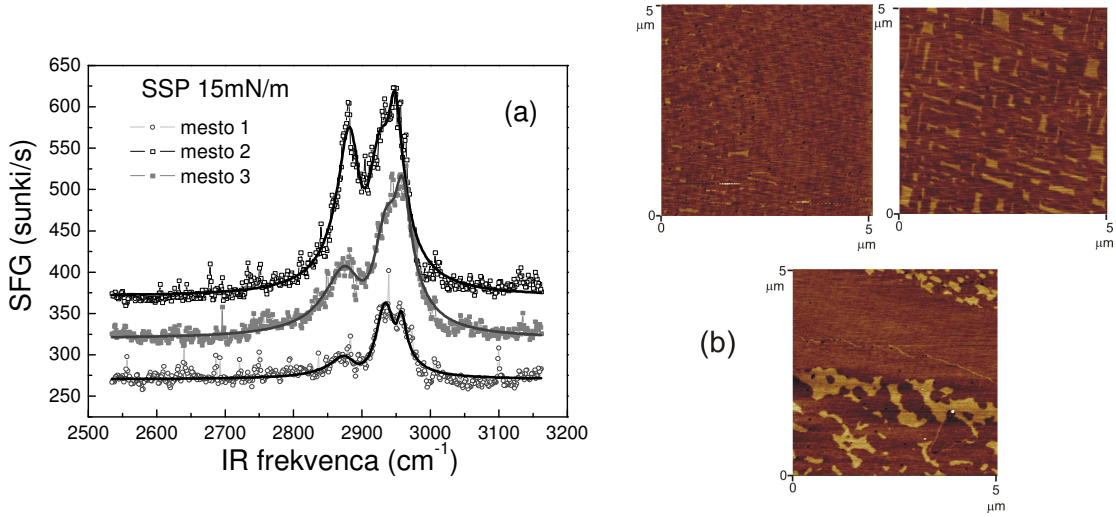

Slika 12-17: (a) SFG spektri Langmuir-Blodgett filma na sljudi pripravljenega pri 15 mN/m dobljeni iz različnih delov filma. (b) AFM slike različnih območij velikosti 5 µm x 5 µm istega LB filma.

Kljub temu, da so LB filmi precej nehomogeni, smo skušali iz SFG in AFM meritev pridobiti informacijo o orientaciji molekul s pomočjo modela, ki sta ga zasnovala Wolfram in Lauberau.

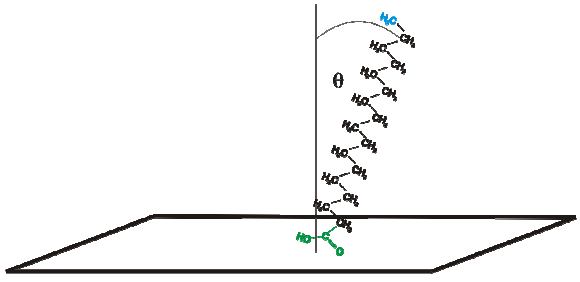

Slika 12-18: Kot nagnjenosti molekule glede na normalo površine, na kateri se molekula nahaja.

Iz razmerja intenzitet dveh vibracijskih vrhov se da za molekule maščobnih kislin določiti kot nagnjenosti molekul glede na normalo površine, na kateri molekule ležijo (Slika 12-18)

$$\frac{A_{ssp,2875}}{A_{ssp,2958}} = -\frac{\beta_{zzz,2875}}{2\beta_{zxx,2958}} \frac{(\gamma+1)\langle\cos\theta\rangle - (\gamma-1)\langle\cos^3\theta\rangle}{\langle\cos\theta\rangle - \langle\cos^3\theta\rangle}, \tag{59}$$

kjer A-ji predstavljajo amplitude resonančnih vrhov, β so hiperpolarizabilnosti molekule, γ je anizotropija molekule, ki jo lahko dobimo iz literature (γ = 1,66). Spektrom smo tako najprej prilagodili naslednjo odvisnost

$$I_{SFG} \propto \left|\chi^{(2)}\right|^2 \cdot I_{IR}(\omega_{IR}) I_{VIS}(\omega_{VIS}) \tag{60}$$

pri čemer velja

$$\chi^{(2)} = \chi_{NR} + \sum_n \frac{A_n}{\omega_{IR} - \omega_n + i\Gamma_n}, \text{kjer je } \chi_{NR} = A_{NR} \cdot e^{i\varphi}. \tag{61}$$

V tej zvezi je χ sestavljen iz neresonančnega prispevka χ_{NR}, ki je posledica substrata in resonančnega dela (vsota Lorentzovih funkcij), ki predstavlja odziv iz vzorca. S prilagajanjem te odvisnosti pridobimo informacijo o amplitudah resonančnih vrhov. Slednje nato ob predpostavki, da so molekule preferenčno orientirane v določeno smer, uporabimo v relaciji (59) ter na ta način dobimo informacijo o kotu naklona θ. Za Langmuirjeve filme dobimo naslednje vrednosti za kote naklona, in sicer 17°, 10° in 10°±2° pri površinskih tlakih 5, 15 in 25 mN/m. Vrednosti naklonskih kotov pri LB filmih pa so bile 30°, 20°±5° in 10° pri površinskih tlakih nanašanja 5 mN/m, 15 mN/m in 25 mN/m. Odvisnosti naklonskih kotov od površinskega tlaka se dobro ujemajo s stopnjo ureditve posamezne faze, v kateri se monosloj nahaja. Največjemu odklonskemu kotu namreč pripada najbolj neurejena plinska faza, najmanjšemu pa urejena trdna faza monosloja. Naklonski kot molekul pa smo določili tudi iz AFM slik, na katerih je vidna terasam podobna struktura (slika 12-17 (b)). Iz AFM smo dobili informacijo o višini teh slojev, in sicer je bila le-ta med 0,6 - 1 nm za vse Langmuir-Blodgett filme. Ker poznamo vzdolžno dimenzijo molekule (2,25 nm), dobimo za naklonski kot θ = 60°-75°. Te vrednosti se v precejšnji meri razlikujejo od tistih dobljenih iz SFG meritev. Na voljo imamo več razlogov za to odstopanje, in sicer lahko AFM konica deformira monosloj in s tem zmanjša njegovo višino, poleg tega pa je lahko model uporabljen pri analizi SFG meritev presplošen in s tem premalo natančen. Verjetno je prava vrednost za naklonski kot nekje med vrednostmi dobljenimi iz SFG in tistimi dobljenimi iz AFM meritev.
Kljub vsem pomanjkljivostim pa lahko trdimo, da je SFG optična tehnika v kombinaciji z AFM precej učinkovita metoda za določitev kvalitete tako Langmuir-Blodgett kot tudi Langmuir filmov.

Bibliography

[1] Robert W. Boyd: Nonlinear optics, Academic Press Limited, London (1992);

[2] Frank Träger: Handbook of Lasers and Optics, Springer, New York (2007);

[3] Hari Singh Nalwa, Seizo Miyata: Nonlinear Optics of Organic Molecules and Polymers, CRC Press (1997);

[4] D.A. Kleinman, *Phys. Rev.* **126**, 1977 (1966);

[5] A.V. Pethukov, *Phys. Rev. B*, **52** (23), 16901-16911, (1995);

[6] N. Bloembergen , R. K. Chang, S. S. Jha, and C. H. Lee, *Phys. Rev.* **174**, 813 (1968);

[7] M. Mauerer, I.L. Shumay, W. Berthold, U. Hoefer, *Phys. Rev. B* **73** (24), 245305 (2006);

[8] K. Nouneh, I. V. Kityk, R.Viennois, S. Benet, S. Charar, S. Malynych, S. Paschen, *Matt. Lett.* **61**(4-5), 1142-1145 (2007);

[9] A.M. Kalashnikova , V.V. Pavlov, R.V. Pisarev, L.N. Bezmaternykh, M. Bayer, and T. Rasing, *JETP Lett*., **80** (5), 293-297 (2004);

[10] M. Oh-e, H. Yokoyama, S. Yorozuya, K. Akagi, M.A. Belkin, and Y.R. Shen, *Phys. Rev. Lett.* **93**, 267402 (2004);

[11] C.M. Johnson, A. B. Sugiharto, S. Roke, *Chem. Phys. Lett.* **449**, 191-195, (2007);

[12] M. Smits , M. Sovago, G.W.H Wurpel, D. Kim, M. Muller, M. Bonn, *J. Phys. Chem. C* **111**(25), 8878-8883 (2007);

[13] X.Y. Chen, A.P. Boughton, J.J.G. Tesmer, Z. Chen, *J. Am. Chem. Soc.* **129** (42), 12658 (2007);

[14] X.Y. Chen, H.Z. Tang, M.A. Even, J. Wang, G.N. Tew, Z. Chen, *J. Am. Chem. Soc.* **128** (8), 2711-2714 (2006);

[15] M. Sovago, R. K. Campen, G. W. H. Wurpel, M. Müller, H.J. Bakker, M. Bonn, *Phys. Rev. Lett.* **100**, 173901 (2008);

[16] M. Barmentlo: Nonlinear optical studies on (liquid-)crystal surfaces, *PhD thesis*;

[17] K. Mivšek, Diplomsko delo, Bachelor degree, Faculty of mathematics and Physics, University of Ljubljana (2004);

[18] T. Heinz: *Second-order nonlinear optical effects at surfaces and interfaces*, chapter 5 of V.M. Agranovich, A.A. Maradudin: *Modern Problems in condensed matter sciences* vol. 29, Elsevier Science Publishers (1991);

[19] L. Komitov, *Journal of the SID*, **11**, 436, (2003);

[20] L. Komitov, B. Helgee, J. Felix, *Appl. Phys. Lett*. **86**, (2005);

[21] M. Škarabot, B. Helgee, I. Muševic, L. Komitov, *J. Appl. Phys.* **98**, 046109 (2005);

[22] Čopič, M., Maclennan, J.E., Clark, N.A., *Phys. Rev .E* **65**, 021708 (2002);

[23] P. Rudquist, P.F. Lagerwall, M. Buivyads, F. Gouda, S.T. Lagerwall, N.A. Clark, J.E. Maclenmann, R. Shao, D.A. Coleman, S. Bardon, T. Belini, D.R. Link, G. Natale, M.A. Glaser, D.M. Walba, M.D. Wand, X.H. Chen, *J. Mater. Chem.* **9**, 1257 (1999);

[24] M.B. Feller, W. Chen, Y.R. Shen, *Phys. Rev. A* **43**, 6778 (1991);

[25] Helgee, B., Hjertberg, T., *Liquid Crystals*, **18**(6), 871, (1995);

[26] K. Kunstelj, I. Drevenšek-Olenik, B. Helgee, L. Komitov, *Mol. cryst. liq. cryst.*, 450, 127-138, (2006);

[27] I. Drevenšek-Olenik, K. Kunstelj, J. Koncilija, L. Komitov, *J. Appl. Phys.*, 100 (073514), (2006);

[28] Yu. G. Fokin, T. V. Murzina, O. A. Aktsipetrov, S. Soria, G. Marowsky, *Phys. Rev. E* **69**, 031701 (2004);

[29] Yu. G. Fokin, S.V. Krupenin, T.V. Murzina, O.A. Aktsipetrov, S. Marowsky, G. Soria, *Surface Science* **566-568**, 783 (2004);

[30] I. Drevenšek-Olenik, M. Čopič, R. Torre, E. Mehdizadeh, *Ferroel*., 148 (349), (1999);

[31] K. Shirota, M. Yaginuma, T. Sakai, K. Ishikawa, H. Takezoe, A. Fukuda, *Appl. Phys. Lett*., 69(2), (1996);

[32] O. A. Aktsipetrov, I. M. Baranova, L. V. Grigor'eva, K. N. Evtyukhov, E. D. Mishina, T. V. Murzina, and I. V. Chernyi, *Kvantovaya Elektron. Moscow* **18**, 943 (1991) [*Sov. J. Quantum Electron.* **21**, 854 1991];

[33] O. A. Aktsipetrov et al., *Phys. Rev. B* **60**, 8924 (1999);

[34] Yu. G. Fokin, T. V. Murzina, O. A. Aktsipetrov, S. Soria, G. Marowsky, *Appl. Phys. B: Lasers Opt.* **74**, 777 (2002);

[35] W.L.V. Price, *Br. J. Appl. Phys.* 18, 1679 (1967);

[36] P. Rudquist *et al., J. Mat. Chem.* **9**, 1257 (1999);

[37] M.G. Samant, J. Stoehr, H.R. Brown, T.P. Russel, J.M. Sands, and S.K. Kumar, *Macromolecules*, **29**, 8334 (1996);

[38] Training Handbook of Scanning Probe Microscope, *Veeco Instruments Inc*. (2003);

[39] J. T. Davis, *Angew. Chem. Int. Ed.* **43,** 668-698, (2004);

[40] J. T. Davis, G.P. Spada, *Chem. Soc. Rev.* **36,** 296-313, (2007);

[41] C.A. Seidel, M.A. Schulz, J. Sauer, *Phys. Chem.* **100,** 5541-5553, (1996);

[42]A. Calzolari, R. Di Felice, E. Molinari, A. Garbesi, *J. Phys. Chem. B*, 108, 2509-2515 (2004);

[43] H. Cohen, C. Nogues, R. Naaman, D. Porath, *Proc. Natl. Acad. Sci. USA* **102,** 11589-11593, (2005)**;**

[44] R. Gutierrez, S. Mohapatra, H. Cohen, D. Porath, G. Cuniberti, *Phys. Rev. B* **74**, 235105, (2006);

[45] M. Gellert, M.N. Lipsett, D.R. Davies, *Proc. Natl. Acad. Sci. USA*, **48**, 2013-2018, (1962);

[46] G.S. Oxford, R.G. Gillespie, *Annu. Rev. Entomol.* **43,** 619-643, (1998);

[47] R.H. Douglas, J.C. Partridge, N.J. Marshall, *Prog. Retinal Eye Res.* **17,** 597-636, (1998);

[48] S. Bonazzi, M. Copobianco, M.M. De Morais, A. Garbesi, G. Gottarelli, P. Mariani, M.G. Ponzi Bossi, G.P. Spada, L. Tondelli, *J. Am. Chem. Soc.* **113,** 5809, (1991);

[49] H. Franz, F. Cuichi, G. Di Nicola, M.M. De Morais, P. Mariani, *Phys. Rev. E* **50**, 395, (1994);

[50] L. Spindler, I. Drevenšek-Olenik, M. Čopič, J. Cerar, J. Škerjanc, P. Mariani, *Eur. Phys. J. E* **13,** 27-33, (2004);

[51] L. Spindler, F. Federiconi, P. Mariani, I. Drevenšek-Olenik, M. Čopič, M. Tomšič, A. Jamnik, *Mol. Cryst. Liq. Cryst.* **435,** 1-12, (2005);

[52] A. Wong, R. Ida, L. Spindler, G. Wu, *J. Am. Chem. Soc.* **127,** 6990-6998, (2005);

[53] T.J. Pinnavaia, C.L. Marshall, C.M. Mettler, C.L. Fisk, H.T. Miles, and E.D. Becker, *J. Am. Chem. Soc.* **100**, 3625, (1978);

[54] C. Detellier, and P. Laszlo, *J. Am. Chem. Soc*. **102**, 1135-1141, (1980);

[55] A. Wong, and G. Wu, *J. Am Chem. Soc.*, **125**, 13895, (2003);

[56] R. Otero, M. Schock, L.M. Molina, E. Laegsgaard, I. Stensgaard, B. Hammer, and F. Basenbacher, *Angew. Chem. Int. Ed.,* **44**, 2270-2275 (2005);

[57] T. Giorgi, S. Lena, P. Mariani, M.A. Cremonini, S. Masiero, S. Pieraccini, J.P. Rabe, P. Samori, G. P. Spada, and G. Gottarelli, *J. Am. Chem. Soc.*, **125**, 14741-14749, (2003).

[58] B. Pergolese, A. Bonifacio, and A. Bigotto, *Phys. Chem. Chem. Phys.*, **7**, 3610-3613, (2005);

[59] R. Rinaldi, E. Branca, R. Cingolani, S. Masiero, G. P. Spada, and G. Gottarelli, *Appl. Phys. Lett.*, 78 (2001) (22), pp. 3541-3543.

[60] R. Rinaldi, G. Maruccio, A. Biasco, V. Arima, R. Cingolani, T. Giorgi, S. Masiero, G.P. Spada, and G. Gottarelli, *Nanotechnology*, 13, (2002), pp. 398-403.

[61] S. D'Amico, G. Maruccio, P. Visconti, E.D'Amone, R. Cingolani, R. Rinaldi, S. Masiero, G.P. Spada, and G. Gottarelli, *Microelectronics Journal*, **34**, (2003), pp. 961-963.

[62] T.C. Marsh, J. Vesenka, and E. Henderson, *Nucleic Acids Res.,* **23**, (1995);

[63] J. Vesenka, E. Henderson, and T. Marsh, *AIP Conf. Proceed.,* **640**, 109-122, (2002);

[64] W. Eimer, and T. Dorfmuller, *J.Phys.Chem.*, **96**, 6790-6800, (1992);

[65] P. Samori, S. Pieraccini, S. Masiero, G.P. Spada, G. Gottarelli, and J.P. Rabe, *Coll. and Surf .B:Biointerf.,* **23**, 283-288, (2002);

[66] K. Kunstelj, F. Federiconi, L. Spindler, I. Drevenšek-Olenik, *Coll. Surf. B: Biointerf.* **59**, 120–127, (2007);

[67] A.B Kotlyar, N. Borovak, T. Molotsky, H. Cohen, E. Shapir, and D. Porath, *Adv. Mater.,* **17**, 1901-1905, (2005);

[68] J. Vesenka, private communication, 2006;

[69] J. Vesenka, D. Bagg, A. Wolff, A. Reichert, R. Moeller, and W. Fritzsche, *Coll. and Surf. B: Biointerf.* **58** (2), 256, (2007);

[70] S. Nishimura, P. J. Biggs, T. Scales, W. Healy, K. Tsunematsu, and T. Tateyama, *Langmuir* **10**, 4554, (1994);

[71] A.A. Lipanov, J. Quintana, and R.E. Dickerson, *J. of Biomol. Struc. and Dyn.* **8**, 483 (1990);

[72] K. Kunstelj, L. Spindler, F. Federiconi, M. Bonn, I. Drevenšek-Olenik, M. Čopič, *Chem. Phys. Lett.***467**, 159-163 (2008);

[73] M.J. Lane, G.J. Thomas Jr., *Biochemistry* **18** (18), 3839, (1979);

[74] M. Mathlouthi, A.M. Seuvre, J.L. Seuvre, J.L. Koenig, *Carbohydr. Res.* **122**, 31, (1983);

[75] M. Smits, M. Sovago, G.W.H. Wurpel, D. Kim, M. Muller, M. Bonn, *J. Phys. Chem. C*, **25**, 111, (2007);

[76] Y. Sartenaer, G. Tourillon, L. Dressen, D. Lis, A.A. Mani, P.A. Thiry, A. Peremans, *Biosensors and Bioelectronics* **22,** 2179, (2007);

[77] J. Wang, M.L. Clarke, Z. Chen, *Anal. Chem.* **76,** 2159, (2004);

[78] C.M. Johnson, , A.B. Sugiharto, S. Roke, *Chem. Phys. Lett*. **449**, 191, (2007) ;

[79] G.J. Simpson, *Chem. Phys. Chem*. **5** 1301(2004) ;

[80] M. Oh-e, H. Yokoyama, K. Yorozuya, K. Akagi, M.A. Belkin, Y.R. Shen. *Phys. Rev. Lett.* **93** 267402, (2004);

[81] B. Busson, A. Tadjeddine, *J. Phys. Chem. C* **112** (31) 11813, (2008);

[82] N. Ji, K. Zhang, H. Yang, Y.R. Shen, *J. Am. Chem. Soc.* **128** (11) 3482, (2006);

[83] J.M. Perry, A.J. Moad, N.J. Begue, R.D. Wampler, G.J. Simpson, *J. Phys. Chem. C* **109** (42) 20009, (2005);

[84] I. Langmuir, *Trans. Faraday Soc.*, **15,** 62-74, (1920);

[85] K.B. Blodgett, *J. Am. Chem. Soc.*, **56**, 495, (1934);

[86] K.B. Blodgett, *J. Am. Chem. Soc.*, **57**, 1007-22, (1935);

[87] P.Martin, M. Szablewski: Langmuir-Blodget troughs, Operating manual of Nima technology (2004);

[88] Michael C. Petty: Langmuir-Blodgett films; An Introduction, Cambridge University Press, Cambridge (1996);

[89] A.N. Bordenyuk, H. Jayathilake, A. V. Benderskii, *J. Phys. Chem. B*, **109,** 15941-15949, (2005);

[90] P. Guyot-Sionnest, J.H. Hunt, Y.R. Shen, *Phys. Rev. Lett.*, **59** (14), 1597-1600, (1987);

[91] R. Superfine, J.Y. Huang, Y.R. Shen, *Phys. Rev. Lett.*, **66** (8), 1066-1069, (1991);

[92] K. Wolfrum, A. Lauberau, *Chem. Phys. Lett.,* **228,** 83-88, (1994);

[93] M.J. Colles, J.E. Griffith, *J. Chem. Phys.* **56**, 3384, (1972);

[94] K. M. Gough, *J. Phys. Chem.* **91,** 2424, (1989);

List of publications:

1. K. Kunstelj, I. Drevenšek-Olenik, B. Helgee, L. Komitov, *Mol. cryst. liq. cryst.*, 450, 127-138, (2006);
2. I. Drevenšek-Olenik, K. Kunstelj, J. Koncilija, L. Komitov, *J. Appl. Phys.*, 100 (073514), (2006);
3. K. Kunstelj, F. Federiconi, L. Spindler, I. Drevenšek-Olenik, *Coll. Surf. B: Biointerf.* **59**, 120–127, (2007);
4. K. Kunstelj, L. Spindler, F. Federiconi, M. Bonn, I. Drevenšek-Olenik, M. Čopič, *Chem. Phys. Lett.***467**, 159-163 (2008);

Izjava

Izjavljam, da sem v disertaciji predstavil rezultate lastnega znanstvenoraziskovalnega dela.

Ljubljana, 19.5.2009 Klemen Kunstelj